Testing the Extremes of Initial Mass Function Variability using Compact Stellar Systems

by

Chloe M. Cheng

A thesis
presented to the University of Waterloo
in fulfillment of the
thesis requirement for the degree of
Master of Science
in
Physics

Waterloo, Ontario, Canada, 2022

Author's Declaration

This thesis consists of material all of which I authored or co-authored: see Statement of Contributions included in the thesis. This is a true copy of the thesis, including any required final revisions, as accepted by my examiners.

I understand that my thesis may be made electronically available to the public.

Statement of Contributions

This research was conducted under the supervision of Michael L. Balogh and Alexa Villaume. Useful insights were also given by the PypeIt development team, especially from J. Xavier Prochaska and Joseph Hennawi. The analysis in this work is based on data collected by Jean Brodie, Charlie Conroy, Ignacio Martín-Navarro, Aaron J. Romanowsky, Pieter van Dokkum, and Alexa Villaume. This study is an extension of Villaume et al. (2017a). The ALF code and models used to fit the data are detailed in Conroy & van Dokkum (2012a) and Conroy et al. (2018). Additionally, Figure 1.1 has been reproduced from Conroy & van Dokkum (2012a), Figure 1.2 has been reproduced from Sparke & Gallagher 2007, and Figure 4.7 has been reproduced from Conroy & van Dokkum 2012b. All other work in this thesis is my own, including data reduction, fitting of data, minor code modifications, data analysis, generation of figures, and manuscript preparation, with feedback from my supervisors.

Abstract

The initial mass function (IMF) is a cornerstone in star formation and galaxy evolution studies. It has traditionally been assumed to be universal, but this has been challenged by increasingly detailed observations of diverse, extragalactic stellar populations. However, this observed variability in the IMF is debated as a sufficient theoretical framework to explain it has not yet been substantiated. A major limitation is that these observations have only probed narrow regions of mass-metallicity-density parameter space (i.e. metal-rich, early-type galaxies). We present an unprecedented sample of integrated light spectroscopy of diverse objects, including "compact" stellar systems (CSSs, i.e. globular clusters and ultra-compact dwarf galaxies) and brightest cluster galaxies. Our sample covers a wide range of metallicities (-1.7 $<$ [Fe/H] $<$ 0.01) and velocity dispersions (7.4 km/s $< \sigma <$ 275 km/s). We carefully reduce high S/N Keck LRIS spectra and measure the IMF by employing a new suite of full-spectrum stellar population synthesis models. These simultaneously fit for ages, metallicities, and detailed chemical abundances, allowing us to robustly measure the effects of the IMF. We show that CSSs do not follow trends with physical parameters that have been found for early-type galaxies (ETGs). In particular, previously established metallicity-dependent trends with the IMF may change in complex ways. We examine potential factors that could be causing the population of CSSs to contrast with the ETGs in this parameter space.

Acknowledgements

I acknowledge and am grateful to have the opportunity to work on the land on which the University of Waterloo operates. The Waterloo, Kitchener, and Cambridge campuses of the University of Waterloo are situated on the Haldimand Tract, land granted to the Haudenosaunee of the Six Nations of the Grand River, and are within the territory of the Neutral, Anishinaabe, and Haudenosaunee peoples. I also wish to recognize and acknowledge the very significant cultural role and reverence that the summit of Maunakea has always had within the indigenous Hawaiian community. I am most fortunate to have the opportunity to make use of data that were obtained via observations from this mountain. Finally, I am grateful to have had the opportunity to conduct the majority of this research on the land which we now call Toronto. For thousands of years it has been the traditional land of the Huron-Wendat, the Seneca, and the Mississaugas of the Credit River, and it is home to many Indigenous peoples from across Turtle Island.

I would like to thank my advisors, Michael L. Balogh and Alexa Villaume, for their supervision, guidance, and expertise. I would also like to thank my advisory and defence committees (Michael Hudson and James Taylor) for their helpful suggestions and feedback. Many thanks to J. Xavier Prochaska, Joseph Hennawi, and the rest of the PypeIt development team for useful insights into troubleshooting and improving my data reduction. Thank you also to Vincent Hénault-Brunet for useful conversations.

The data presented herein were obtained at the W. M. Keck Observatory, which is operated as a scientific partnership among the California Institute of Technology, the University of California and the National Aeronautics and Space Administration. The Observatory was made possible by the generous financial support of the W. M. Keck Foundation. This research has made use of the NASA/IPAC Extragalactic Database (NED), which is operated by the Jet Propulsion Laboratory, California Institute of Technology, under contract with the National Aeronautics and Space. This research has also made use of the SIMBAD database, operated at CDS, Strasbourg, France Administration.

Table of Contents

List of Figures

List of Tables

Chapter 1

Introduction

A major area of study in astrophysics is galaxy formation and evolution, of which a deep understanding is needed to learn about cosmology and the evolution of the Universe. A key first step in achieving this is to understand stellar populations and star formation (SF) in these galaxies. For example, we can learn about when galaxies formed by measuring stellar ages and about chemical enrichment and stellar feedback by measuring metallicities and abundances (Conroy & van Dokkum 2012a; Conroy et al. 2018). A fundamental concept underpinning these measurements is the distribution of birth stellar masses in a galaxy, called the initial mass function (IMF, e.g. Bastian et al. 2010; Conroy 2013; Hopkins 2018). The IMF provides insight into the physics needed to describe SF as it is one of the principal results from SF theories. It is also needed to translate observables (e.g. galaxy luminosities) into physically meaningful quantities (e.g. stellar masses, SF rates, Hopkins 2018; Smith 2020).

The importance of the IMF was first recognized by Salpeter (1955), who found that its shape could be characterized by a single power law (PL) with slope ~ 2.35 for stellar masses $\gtrsim 0.5$ $M_\odot$. This parameterization was updated to include lower masses and is now often characterized as a double PL (2PL, Miller & Scalo 1979; Scalo 1986; Kroupa 2001; Chabrier 2003). Subsequent measurements made via the direct method of resolved star counts in nearby SF regions have produced similar results, regardless of location or age (Sagar et al. 2001; Bastian et al. 2010; Da Rio et al. 2012; Peña Ramírez et al. 2012; Andersen et al. 2017; Suárez et al. 2019; Damian et al. 2021). Thus, the prevailing picture of the IMF indicates a universal form and little-to-no variation with environment (Bastian et al. 2010; Offner et al. 2014; Krumholz 2014). However, this limited number of galaxies that are close enough for their stars to be resolved are not representative of the full diversity in the Universe, for which we need to examine more distant systems. Moreover, it is expected that

the IMF should vary with physical properties. In particular, since the MW at present-day is relatively quiescent, it is unlikely that it represents the entire range of conditions under which stars have formed throughout the Universe and across all cosmic time. For example, it would be surprising if galaxies that display intense SF at high redshifts, discovered via sub-millimetre continuum emission and thought to be the progenitors of today's massive early-type galaxies (ETGs), have the same IMF as the MW (Smith 2020). Furthermore, a variety of modern astrophysical problems can be explained by a variable IMF, such as different SF histories that turn over, remain flat, or continue to rise to very high redshifts (Bastian et al. 2010).

Unfortunately, it is currently impossible to resolve distant stars to validate these results. Thus, despite the fact that there is little theoretical reason for the IMF to remain the same across all SF regions (e.g. Schwarzschild & Spitzer 1953; Larson 1986; Kroupa 2001; Hennebelle & Chabrier 2008; Krumholz et al. 2011; Hopkins 2012, 2013; Chabrier et al. 2014), and that there remain key uncertainties in the measured universal IMF (i.e. star counting requires assumptions about ages, metallicities, binary star fractions, and mass segregation, Hopkins 2018), it is often still assumed to be universal. This makes it one of the most significant sources of systematic uncertainty in stellar population studies (Hopkins 2018).

While direct measurements cannot be made, indirect attempts to characterize the extragalactic IMF are ongoing. These different types of measurements are difficult to compare directly because they have been made via fundamentally different methods, but they can allow for insight into the IMF's behaviour in diverse environments. In particular, one can measure the integrated light of distant galaxies. Spectral features that are sensitive to low-mass M dwarf and massive M giant stars, respectively, can then be used to quantify the relative numbers of each type of star. Specifically, low-mass ($\lesssim 0.5$ $M_\odot$) and massive stars at the same effective temperature display differences discernible at a level of $\sim 1-3\%$ in high S/N spectra (Smith 2020). For example the Wing-Ford band is a spectral feature seen in M dwarfs but not M giants (Wing & Ford 1969). This allows for IMF determinations over a wide range of stellar masses. The high-mass end of the IMF can be constrained using features that are sensitive to the number of massive stars, for example the ratio of Hα to UV emission (Hopkins 2018). In this way, the high-mass IMF can be constrained as top-heavy (containing an excess of M giant stars) or top-light (lacking M giant stars). On the other hand, the low-mass end is especially important to constrain since, despite their low luminosity, the majority of stars in the Universe are less massive M dwarfs. Thus, small changes in their inferred quantity can impact the mass-to-light ratio (M/L) significantly (van Dokkum & Conroy 2012; Conroy & van Dokkum 2012a; Conroy

& van Dokkum 2012b; Conroy 2013; Hopkins 2018).[1] In this way, the low-mass IMF can be constrained as bottom-heavy (containing an excess of M dwarf stars) or bottom-light (lacking M dwarf stars).

Because of M dwarf stars' disproportionately small contribution to the integrated light of a galaxy, despite their importance to the total stellar mass, it can be difficult to quantify them. However, M giant stars have lower surface gravity, which affects the strengths of certain spectral lines, allowing for the differentiation between these different types of stars (Conroy & van Dokkum 2012a; Smith 2020). This is demonstrated in Figure 1.1, which has been reproduced from Conroy & van Dokkum (2012a) (their Figure 7). This displays the strengths of several strong spectral absorption features in M dwarf stars (red) and M giant stars (black). For example, the NaI0.82 feature in the first panel is stronger in M dwarf stars than in M giant stars.

The basic idea for the physical origin of these different surface gravity trends can be understood by considering the fact that every strong feature in M dwarf stars is from a neutral metal (e.g. NaI, KI, CaI, AlI), while every strong feature in M giant stars is from a singly-ionized metal (e.g. CaII). This is due to ionization equilibrium. In particular, as electron pressure increases at a fixed temperature due to increased surface gravity, then for the same species of atoms, the ratio of singly-ionized to neutral atoms decreases (Conroy & van Dokkum 2012a). This is evident in Figure 1.1: for stars with effective temperature $T_{\rm eff} = 3500$ K, M dwarf stars have a greater relative abundance of NaI but a lesser relative abundance of CaII compared to M giant stars at the same $T_{\rm eff}$. For molecules, due to molecular dissociation equilibrium (Russell 1934; Tsuji 1973), the side of a chemical reaction that results in fewer moles of gas is favoured because of the increase in the partial pressures of atoms and molecules. For example, the formation of H_2O is favoured because this results in fewer moles of gas compared to the formation of H and O individually (Conroy & van Dokkum 2012a). Conroy & van Dokkum (2012a) also found that, at fixed $T_{\rm eff}$, molecules are in greater abundance with respect to hydrogen for M dwarfs than for M giants.

M dwarf and M giant stars are furthermore important because they contribute crucially

[1] For a stellar population undergoing passive evolution, note that evolution in the M/L is sensitive to the IMF's logarithmic slope at the main sequence turnoff. In particular, the IMF dictates the rate at which the giant branch is populated by turnoff stars, since stars on the giant branch comprise the majority of a stellar population's luminosity. As such, the logarithmic evolution of luminosity over logarithmic time ($d\ln L/d\ln t$) scales linearly with the IMF's logarithmic slope. Steeper IMF slopes indicate a more well-populated giant branch as a function of time, and therefore reduced natural luminosity dimming. If the logarithmic slope of the IMF is sufficiently steep, the luminosity is dominated by unevolving low-mass stars, and the integrated luminosity is approximately constant as a function of time (Tinsley 1980; van Dokkum 2008; Conroy et al. 2010; Conroy 2013; Hopkins 2018).

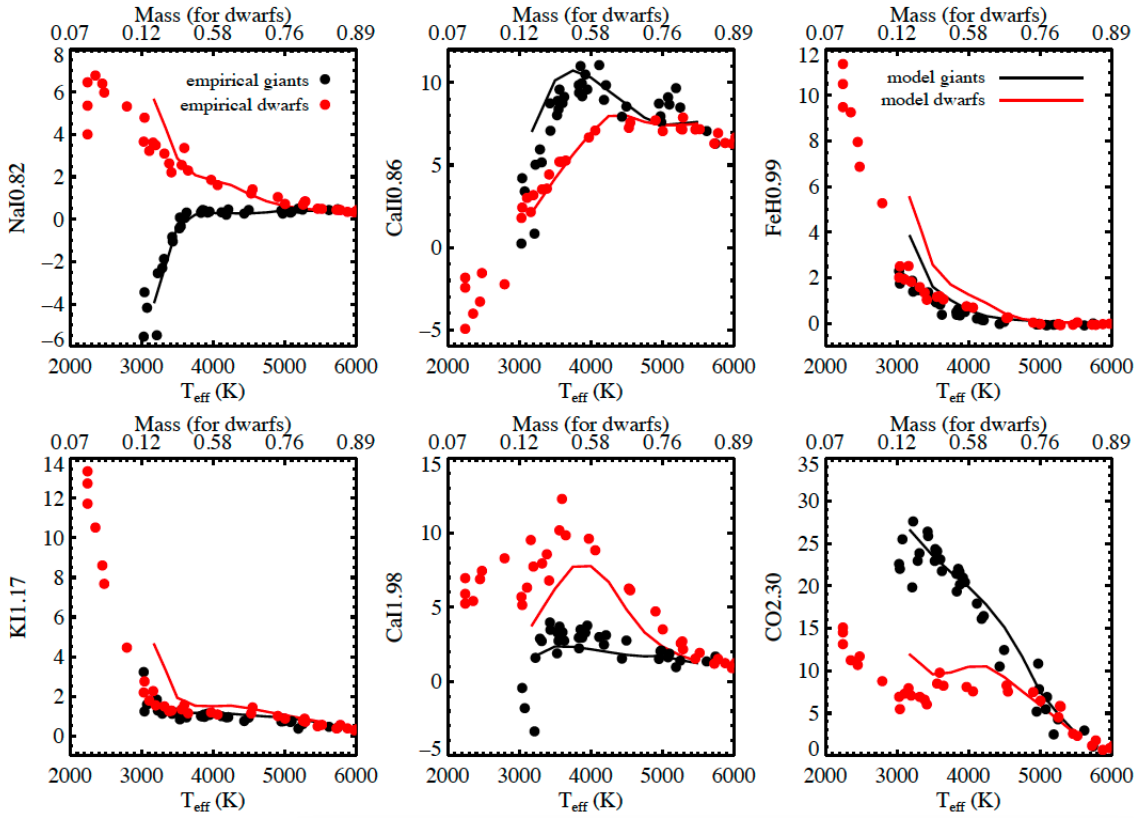

Figure 1.1 The equivalent widths of strong spectral absorption features as function of effective temperature ($T_{\rm eff}$), which is translated to stellar mass for M dwarfs at the top of each panel. Red points and lines represent M dwarf stars and black points and lines represent M giant stars. For example, the NaI0.82 feature in the first panel is stronger in M dwarfs than in M giants. Figure reproduced from Conroy & van Dokkum (2012a) (Figure 7).

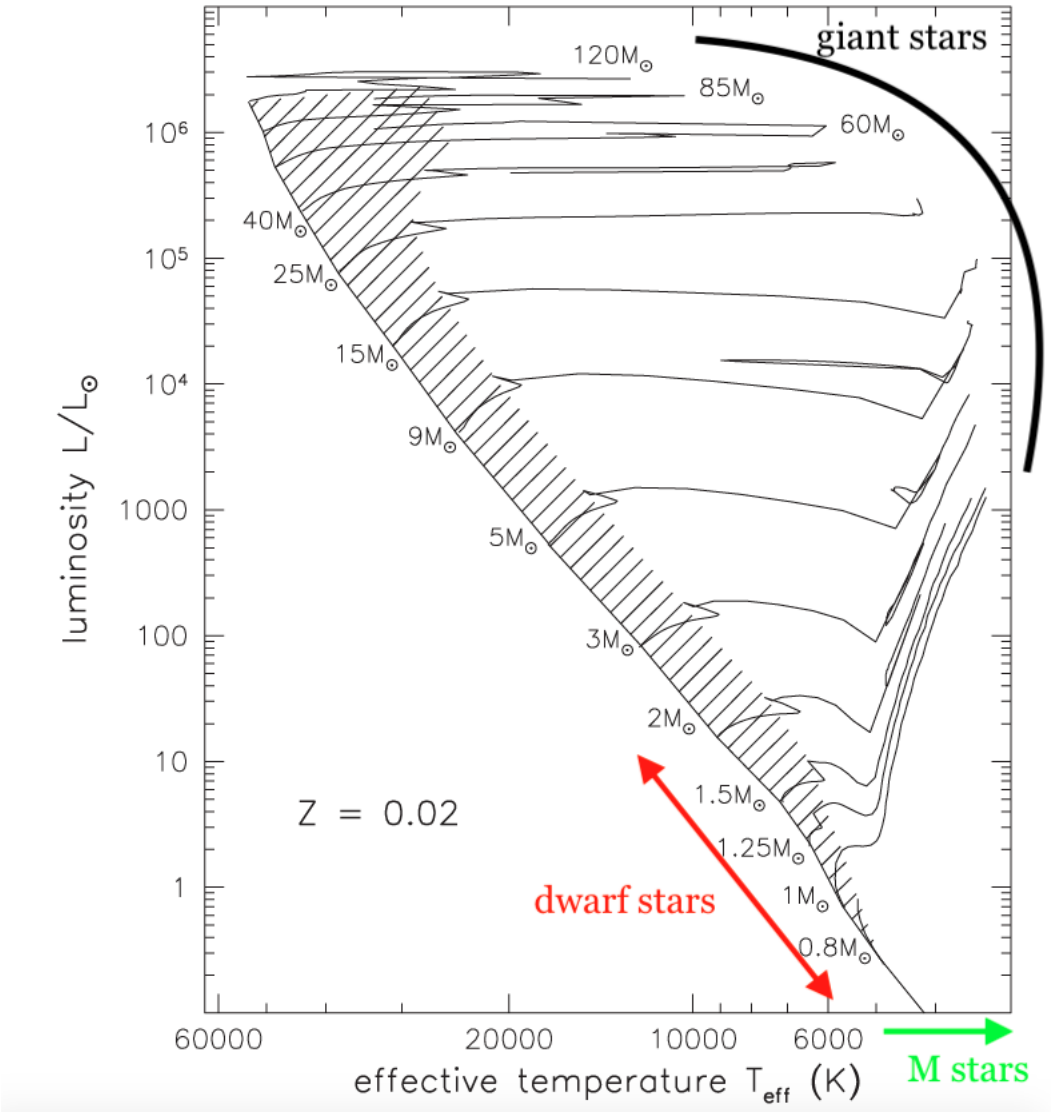

Figure 1.2 A Hertzsprung-Russell (HR) diagram showing luminosity and effective temperature for stars of different masses with solar chemical abundances. Evolutionary tracks (Geneva, Schaller et al. 1992; Charbonnel et al. 1996, 1999) are shown from the main sequence onward, with the hatched region indicating where the core of the star is burning hydrogen. Regions relevant to M dwarf stars and M giant stars, respectively, are indicated. In particular, M dwarfs are main sequence stars with $T_{\rm eff} < 4000$ Å and M giant stars are stars on the red and asymptotic giant branches with $T_{\rm eff} < 4000$ Å. Figure reproduced from Sparke & Gallagher (2007) (Figure 1.4).

to the subsequent SF and evolution of their host galaxies. In particular, while M dwarfs and giants have important differences in their masses, they also have important differences in their evolutionary stages. To conceptualize the differences in luminosity, temperature, and evolution between these stars, we show a Hertzsprung-Russell (HR) diagram in Figure 1.2, reproduced from Sparke & Gallagher (2007) (their Figure 1.4). Note that stars with masses < 0.8 $M_{\odot}$ are M dwarf stars and have not left the main sequence since the Big Bang. It is these less massive stars which we are interested in constraining. M giant stars, on the other hand, are those that are further evolved, in particular those on the red and asymptotic giant branches (Tinsley 1980; Carroll & Ostlie 2017; Sparke & Gallagher 2007). These contribute to the high-mass end of the IMF. The masses of M giant stars depend on the age of the stellar population to which they belong, and therefore the ratio of dwarf-to-giant stars, which is what we can constrain using integrated light, is related to an age-dependent ratio of their stellar masses (Conroy & van Dokkum 2012a).

While M dwarf and M giant stars display key differences, this method of using integrated light to differentiate them is difficult. This is because the integrated light from stellar populations is dominated by M giant stars, with M dwarf stars contributing a disproportionately small amount. Moreover, any light that can be detected from M dwarfs looks very similar to that from M giants. Although this method was identified in the 1960s, due to poor data and model quality and detector technology (e.g. Spinrad & Taylor 1971; Cohen 1978; Faber & French 1980; Kennicutt 1983; Carter et al. 1986; Hardy & Couture 1988; Delisle & Hardy 1992; Couture & Hardy 1993), early implementations did not lead to definitive conclusions. A clear picture of the entire mass range of the IMF therefore could not be formed. Since then, however, the quality of models and data of stellar interiors and atmospheres have increased significantly. As such, integrated light could now be used to robustly constrain the IMF in distant galaxies, though this remains challenging and subject to systematic uncertainties (Hopkins 2018; Smith 2020).

The traditional approach to interpreting integrated light is by measuring the equivalent widths of a limited number (3-20) of absorption features, called spectral indices. This was used partially because early spectral observations of early-type galaxies (ETGs) had relatively low spectral resolution and partially an attempt to focus on features that showed the most sensitivity to IMF variation (Conroy 2013). This method is still widely used due to its efficiency - if only a narrow spectral region is available, one can still quantify numbers of stars, as long as there are a few M dwarf- and M giant-sensitive features available (Worthey 1994; Lonoce et al. 2021). One of the first studies to use this in the modern resurgence of variable IMF studies was Cenarro et al. (2003). They found variations in the calcium triplet (CaT) index in massive ETGs which could not be explained by age, metallicity, and chemical abundances alone. They suggested that more flexibility in their models was

required, perhaps in the form of a variable IMF.

More detailed results were subsequently found by fitting entire integrated spectra using stellar population synthesis (SPS) models. Here, a synthetic spectrum is produced by combining the spectra of a galaxy's expected types of stars and is compared to observed spectra to find a best-fit model (Conroy 2013; Smith 2020). This allows for arbitrary variation in stellar parameters, including the IMF, age, and chemical abundances (Conroy & van Dokkum 2012b). In principle, their goal is to extract fundamental physical properties of stellar systems (e.g. SF histories, metallicities, abundances, dust mass, etc.) encoded in spectral energy distributions (Conroy 2013). An early study to apply these was Conroy & van Dokkum (2012b), who used the full spectrum SPS model, ALF (Conroy & van Dokkum 2012a), to fit the integrated spectra of massive ETGs. They found that the IMF becomes more bottom-heavy with [Mg/Fe] and velocity dispersion. This was one of the first robust pieces of evidence for an IMF that varies with physical parameters. Many similar results have followed (e.g. Spiniello et al. 2012; La Barbera et al. 2013; Ferreras et al. 2013; McDermid et al. 2014; Posacki et al. 2015).

If the IMF is variable, the cause of these variations must also be determined. This is crucial to our understanding of the IMF and its broader observational implications (e.g. this will reduce uncertainties on stellar masses and SF rates derived using the IMF). In a widely accepted picture of SF, it is thought that the majority of stars are born in regions of the interstellar medium (ISM) called molecular clouds (e.g. Lada & Lada 2003; Padoan & Nordlund 2002, though see, e.g. Krumholz & McKee 2020; Ward et al. 2020 for an alternative explanation). The ISM is largely made up of dust and cold hydrogen gas, which undergoes turbulent motion due to stellar feedback. This can inject turbulent kinetic energy and restore turbulence, and it can also introduce galactic-scale accretion and shear motion (Mathew & Federrath 2021). Thus, overdensities can develop within molecular clouds (Elmegreen & Scalo 2004). With time, these overdensities increase in density and pressure, eventually collapsing under their own self-gravity. At this point, they become dense structures called cores, which will eventually turn into stars (Mac Low & Klessen 2004; McKee & Ostriker 2007). This process is known as turbulent fragmentation, where supersonic shocks can create dense cores by compressing gas as they move through the ISM (Padoan & Nordlund 2002; Nam et al. 2021). Since stars form from the collapse of dense, gravitationally unstable cores in molecular clouds, it is plausible that the shape of the IMF is also a result of turbulent fragmentation (Padoan & Nordlund 2002; Chon et al. 2021). The IMF may also be affected in complex ways by gravity, magnetic fields, and outflows (Dib et al. 2010; Guszejnov et al. 2017; Mathew & Federrath 2021).

The emerging picture depicts metallicity as a key driver (e.g. Geha et al. 2013; Martín-Navarro et al. 2015; van Dokkum et al. 2017), which is theoretically motivated because of its

role in regulating cloud cooling and fragmentation efficiency (Hopkins 2013; Chabrier et al. 2014). If metallicity is driving IMF variations, there are strong implications for several aspects of galaxy formation. For example, this would imply that the IMFs of massive ETGs have been bottom-heavy since $z \sim 1$, as it has been shown that their chemical compositions have not changed since then (Martín-Navarro et al. 2015). Metallicity is also important from a SF and evolution standpoint. Throughout their evolution, stars synthesize heavier elements and can inject these back into the ISM in different ways. For low- and intermediate-mass stars, gas from the outer layers can be ejected as stellar superwinds during the asymptotic giant branch phase. For more massive stars, the outer layers of the star can fall into the core and become ejected as Type Ib, Ic, or II supernovae, or as Type Ia supernovae, where the star completely blows itself apart. These explosions act to eject gas rich in α-elements and other heavy elements, enriching the ISM (Tinsley 1980; Carroll & Ostlie 2017; Sparke & Gallagher 2007). In this way, the evolution of different stars contributes importantly to the overall metallicity of a galaxy. On the other hand, a galaxy's metallicity also affects the evolution of stars of a given mass, via the initial metallicity of the ISM from which stars are formed. This means that the ratio of dwarf-to-giant stars will also depend on metallicity.

The ubiquity of this idea has become widespread, with some recent studies assuming a metallicity-dependent IMF (e.g. Clauwens et al. 2016; Prgomet et al. 2021; Sharda & Krumholz 2022). However, it is not clear if different metallicity-dependent relationships are consistent (e.g. Geha et al. 2013; Martín-Navarro et al. 2015) and not all objects seem to follow these trends (Conroy & van Dokkum 2012b; Newman et al. 2017; Villaume et al. 2017a). Moreover, metallicity is mutually correlated with other parameters (e.g. velocity dispersion, α-element abundances), all of which have different physical implications. For example, if the IMF depends on metallicity, there will still be a dependence on α-element abundances. A top-heavy IMF will produce more massive stars, which will contribute to the ISM's enrichment via the ejection of α-elements by supernovae, as described above. This will result in the next generation of stars having a different IMF, and in this way one might expect to see a correlation between the top-heaviness of the IMF and α-element abundances. Correlations between variations in IMF slopes and these other parameters have been found as well (e.g. Conroy & van Dokkum 2012b; Geha et al. 2013; Martín-Navarro et al. 2015; Li et al. 2017; Gennaro et al. 2018; Martín-Navarro et al. 2021). In the case of velocity dispersion, correlations with IMF variations could be explained by physical properties of SF clouds during the formation of a massive galaxy, since σ traces a galaxy's gravitational potential (Larson 2005; La Barbera et al. 2013). On the other hand, [Mg/Fe], which is often used to represent α-element abundances, is often used as a proxy for SF timescales (Martín-Navarro et al. 2015, though see Martín-Navarro (2015) for an

alternative point of view), so a correlation here suggests that the shape of the IMF may be intimately tied to SF intensity (Conroy & van Dokkum 2012b).

Additionally, the metallicity of a galaxy is affected not only by the evolution of stars and their ejecta described above, but also on the mixing of this ejecta with interstellar gas. Gas inflows can affect the total metallicity by diluting the products of stellar nucleosynthesis and evolution with unenriched material from outside of the galaxy. Similarly, gas outflows can carry metals between different regions of a galaxy, or transport them out of the galaxy entirely (Tinsley 1980). Moreover, inflows and outflows are closely related to σ. In particular, gas-rich accretion via cold streams (Kereš et al. 2005; Dekel et al. 2009) or gas rich mergers (Khochfar et al. 2011) can increase mass and σ (Cappellari et al. 2013). In this way, these parameters are intimately related, as galaxies with different values of σ can have different metallicities and SF histories (Tinsley 1980; Cappellari et al. 2013). As an example of how these correlations are difficult to disentangle, Barber et al. (2018) implemented a variable IMF model in the EAGLE galaxy formation simulations. In particular, they allowed either the low- or high-mass segments of a 2PL IMF to depend on local ISM pressure, and calibrated this relationship to reproduce the correlation with σ from Cappellari et al. (2013). When they applied this to low-mass IMF slopes, the simulations predicted a positive correlation between the global $\alpha_{\rm IMF}$ and age for ETGs and a weak negative correlation with global metallicity (Barber et al. 2019a). This also lead to a negative radial gradient of $\alpha_{\rm IMF}$ within the galaxies (Barber et al. 2019b). These gradients also lead to strong correlations with local metallicity (Smith 2020). Thus, the primary driver of correlations is difficult to establish. Velocity dispersion in particular is a prominent alternative contender (Cappellari et al. 2013; Ferreras et al. 2013; La Barbera et al. 2013; Spiniello et al. 2014; Villaume et al. 2017a; La Barbera et al. 2019).

Alternative methods have additionally been used to measure the extragalactic IMF, for example via stellar dynamics (e.g. Cappellari et al. 2012; Cappellari et al. 2013) or strong lensing (e.g. Treu et al. 2010). These methods allow for inferences of the total mass (luminous and non-luminous) in galaxies. The dark matter (DM) and stellar contributions can be separated by assuming the spatial distribution of stellar mass follows luminosity and the DM halo profile follows a parameterized form, leading to a constraint on the IMF in the form of an estimate of the dynamically-measured stellar M/L ($(\mathrm{M/L})_{\rm dyn}$, Smith 2020). These studies have revealed increasing ($(\mathrm{M/L})_{\rm dyn}$) with σ, broadly consistent with the results of Conroy & van Dokkum (2012b) and reinforcing the idea that σ is a key driver.

Despite this evidence, IMF variability remains debated. In particular, these dynamical IMF measurements must serve as an upper limit for spectroscopic ones. This is because they take into account dark and luminous mass, while spectroscopic measurements only

measure luminous mass. However, different studies often find differing levels of consistency. For example, Smith (2014) showed that, while both the spectroscopic Conroy & van Dokkum (2012b) and dynamical Cappellari et al. (2013) results favoured a bottom-heavy IMF on average, there was no correlation between individual galaxies in each sample.

While this particular discrepancy may have been resolved by Lyubenova et al. (2016) (they examined a homogeneous sample of ETGs to avoid aperture effects that can result from comparing different studies, finding agreement between dynamics and spectroscopy for individual galaxies), there are still other unexpected discrepancies. For example, some studies (e.g. Newman et al. 2017; Zieleniewski et al. 2017; Alton et al. 2017, 2018) have found individual ETGs that do not follow the trend of increasing bottom-heaviness with σ (Ferreras et al. 2013; La Barbera et al. 2013; Spiniello et al. 2014), but may instead be consistent with MW IMFs. It is not yet clear whether these outliers are the result of data or model systematics, or if they are indicative of a real effect. If this is a real effect, then it is furthermore unclear how to reconcile these results and the universal IMF in the MW with variable extragalactic results (Guszejnov et al. 2019). It is also not clear how to reconcile IMF variability and its implications with previous chemical evolution and SF history measurements (Martín-Navarro 2015).

Part of this difficulty in understanding the IMF is that most studies have focused on metal-rich, massive ETGs, but this defines a narrow parameter space in metallicity, density, and σ. Since most galaxies in the Universe are metal-poor dwarfs, it is necessary to expand this parameter space (Villaume et al. 2017a, V17 hereafter). For example, recent star counting studies in local, metal-poor, SF regions have found IMF variations (e.g. Geha et al. 2013; Gennaro et al. 2018; Hallakoun & Maoz 2021). Geha et al. (2013) and Gennaro et al. (2018) studied several nearby ultra-faint dwarf galaxies (UFDs) which are satellites of the MW, and found IMFs that were more bottom-light than that of the Galactic disc (where bottom-light indicates a lack of low-mass stars compared to the MW). Moreover, Geha et al. (2013) found a trend with metallicity in metal-poor UFDs that echoes the extragalactic result from Martín-Navarro et al. (2015). This may contribute evidence contradicting the idea of "universality".

To fill in this parameter space and more conclusively determine the primary driver of variability, we must study objects with similar metallicities but a wider range of σ compared to Geha et al. (2013). "Compact" stellar systems (CSSs, Norris et al. 2014), especially globular clusters (GCs) and ultra-compact dwarf galaxies (UCDs), are of particular interest. GCs are compact star clusters which are important for understanding galaxy formation because they exist in the MW and externally, connecting distant galaxies and local stellar populations (Carretta et al. 2010). They have been used to test full spectrum SPS models, since they have similar metallicities and element enhancements as ETGs, but

fundamentally different formation histories and stellar populations (Conroy & van Dokkum 2012b; V17). In particular, they have historically been thought to have MW IMFs. They have also been thought to represent simple stellar populations (SSPs), with a common age and metallicity throughout (although note recent evidence indicates GCs are actually multiple stellar populations as they host large star-to-star abundance spreads in their light elements, Prantzos & Charbonnel 2006; Carretta et al. 2010; Bastian & Lardo 2018). Thus, they should not have the same trends in spectroscopic M/L ($(M/L)_*$) unless SPS models are not performing correctly (V17). Furthermore, GCs are not expected to contain any dark matter (DM), simplifying the comparison between dynamics and spectroscopy (Grillmair et al. 1995; Odenkirchen et al. 2003; Conroy et al. 2011).

On the other hand, UCDs are dense stellar systems lying between GCs and traditional dwarf galaxies in the luminosity-size plane ($-13.5 \lesssim M_B \lesssim -11.5$, 2×10^6 $M_\odot \lesssim M_* \lesssim 10^8$ $M_\odot$; Hilker et al. 1999; Drinkwater et al. 2000; Evstigneeva et al. 2007; Paudel et al. 2010; Mieske et al. 2013). Their formation pathway is a major open question. Some may be the compact nuclei of dwarf galaxies that have been tidally stripped (Bekki et al. 2001, 2003; Drinkwater et al. 2003; Goerdt et al. 2008; Forbes et al. 2014; Voggel et al. 2019; Mayes et al. 2020) and some may be massive or merged star clusters (Kroupa 1998; Fellhauer & Kroupa 2002; Evstigneeva et al. 2007; Brüns et al. 2011; Brüns & Kroupa 2012; Mieske et al. 2012). Some combination of these mechanisms may also be possible - in particular, it has been suggested that UCDs with masses $M > 10^7$ $M_\odot$ are the stripped nuclei of dwarf galaxies (Forbes et al. 2014; Janz et al. 2015; Sánchez-Janssen et al. 2019; Mayes et al. 2020), while UCDs with $M < 2 \times 10^6$ $M_\odot$ are either stripped nuclei that overlap in mass with the GC population (Mayes et al. 2020) or merged GCs. Differentiating these two populations is challenging.

GCs and UCDs are furthermore interesting in the context of this study because both have unexpected discrepancies in their $(M/L)_{dyn}$ behaviour. Strader et al. (2011) found a trend of decreasing $(M/L)_{dyn}$ with metallicity in M31 GCs, inconsistent with SSP models. They suggested a variable IMF as a potential explanation. Moreover, most UCDs with $M_* > 10^7$ $M_\odot$ possess elevated $(M/L)_{dyn}$ compared to those expected for SSPs or predicted spectroscopically (e.g. Haşegan et al. 2005; Mieske et al. 2008a; Dabringhausen et al. 2008; Frank et al. 2011; Strader et al. 2013). Excess dark mass in the centres of these objects can explain this elevation, but its form is unclear. Suggestions include dark matter, a central supermassive black hole (SMBH), excess mass resulting from a variable IMF, or some combination (Mieske et al. 2013). SMBHs have been detected in some UCDs and thus these are also confirmed stripped nuclei (Seth et al. 2014; Ahn et al. 2017, 2018; Afanasiev et al. 2018). However, IMF variations have also been found in other UCDs (e.g. Mieske & Kroupa 2008; Murray 2009; Dabringhausen et al. 2012; V17), so other explanations cannot

be ruled out. Moreover, if the IMFs of UCDs are variable, then their proposed formation pathways offer predictions for how this variation may appear. If UCDs belong to the star cluster population (i.e. merged or massive GCs, Kroupa 1998; Fellhauer & Kroupa 2002; Evstigneeva et al. 2007; Brüns et al. 2011; Brüns & Kroupa 2012; Mieske et al. 2012), then it is plausible that they have IMFs similar to those of GCs, which are thought to be MW-like (e.g. Conroy & van Dokkum 2012b; V17). If the UCDs belong to the galaxy population (i.e. the stripped remnants of once more massive galaxies), then it is plausible that they have more bottom-heavy IMFs (e.g. V17). In particular, ETGs have been found to have IMF gradients, with a more bottom-heavy IMF in the core and a MW IMF in the outskirts (e.g. van Dokkum et al. 2017). The tidal-stripping of the stars in the outskirts would leave behind only the bottom-heavy core.

Some of these questions were first addressed in V17. Their results indicated that CSSs behave differently than the main sample of ETGs in the literature. Additionally, they concluded that metallicity is not the sole driver of variability and point to σ instead, differing critically from the prevailing assumption in the literature (e.g. Martín-Navarro et al. 2015). These results have raised crucial questions about IMF variability and SF theory, but definitive conclusions could not be drawn due to the small sample size. To explore these issues further, we increase the sample size of V17 significantly. We use the ALF models to measure IMF variability in 11 GCs, 4 UCDs, and 2 BCGs. By homogeneously studying a diverse sample of objects, we hope to better understand the behaviour of the IMF in CSSs and how this fits into our current picture in other stellar systems.

This thesis is organized as follows: in Chapter 2 we describe our sample and data reduction. We describe the ALF full spectrum SPS model in Chapter 3. We present our fit results in Chapter 4, and discuss these results in Chapter 5. We propose directions for future study in Chapter 6. Finally, we make conclusions and summarize in Chapter 7.

Chapter 2

Sample and Data Reduction

2.1 Sample Selection

We examine a diverse set of stellar systems, including eleven M31 GCs, four Virgo cluster UCDs, and the centres of two Coma cluster BCGs. The full sample is listed in Table 2.1. We also include several objects from V17 and examine new data for B058 to directly compare our results. Among the UCD sample we include VUCD3 and M59-UCD3, which have evidence for central SMBHs (Ahn et al. 2017, 2018). As discussed in Section 1, this strongly suggests that they are stripped nuclei. Black hole masses in these galaxies are reported in Table 4.5.

We include G001, a massive star cluster in M31. G001 is intriguing because the mechanism of its formation remains highly debated, due to its unusual abundance patterns and unique location in M31's outer halo (Meylan et al. 2001; Sakari et al. 2021). It has been argued to host an intermediate-mass BH (Gebhardt et al. 2002, 2005), it could have originated as a nuclear star cluster (Baumgardt et al. 2003), or it may be a GC with large Fe spreads (Meylan et al. 2001; Nardiello et al. 2019). We choose the remaining M31 GCs in our sample to expand the metallicity range of that in V17.

Finally, we include the centres of the two Coma cluster BCGs from Zieleniewski et al. (2017) (Z17), both of which are in apparent contradiction to the trends of increasingly bottom-heavy IMFs with increasing σ found in other studies. In particular, near-MW IMFs were measured for both NGC 4874 and NGC 4889 in Z17. We compare our results to Z17 and address this tension in the characterization of the IMF.

The sample is deliberately chosen to span a wide range of metallicities, stellar masses, σ, and densities, to help us gain a more complete picture of IMF variation. This is illustrated

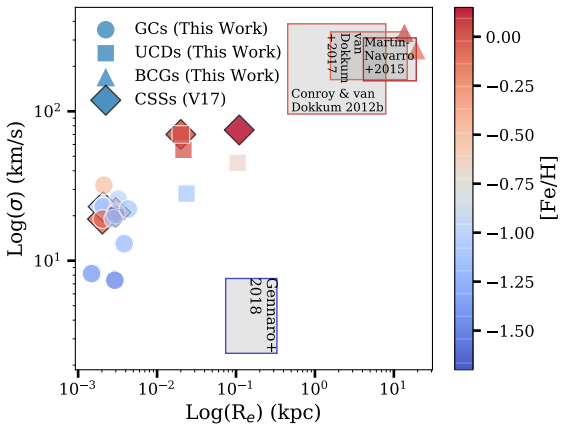

Figure 2.1 The extent of our sample, compared to previous studies. We show logarithmic effective radius ($R_{\rm e}$) versus logarithmic velocity dispersion (σ) for each of the GCs (circles), UCDs (squares), and BCGs (triangles) in our sample. These are colour-coded by metallicity. We compare our sample directly to that in V17 (diamonds) to show that we fill in the metallicity range examined there. The grey rectangles indicate parameter spaces covered by previous studies examining metal-rich ETGs (Conroy & van Dokkum 2012b; Martín-Navarro et al. 2015; van Dokkum et al. 2017) and metal-poor ultra-faint dwarf galaxies (Gennaro et al. 2018, which is an extension of Geha et al. (2013)). These are outlined by the colour that represents the average metallicity of each sample.

in Figure 2.1, where we plot logarithmic effective radius (R_e) versus logarithmic σ for each object, colour-coded by metallicity. For comparison, we also show individual points for the V17 sample. The grey rectangles indicate parameter spaces covered by previous studies, including those that examine metal-rich ETGs (Conroy & van Dokkum 2012b; Martín-Navarro et al. 2015; van Dokkum et al. 2017) and metal-poor UFDs (Gennaro et al. 2018). These rectangles are outlined by the colours that represent each respective study's average metallicity. This Figure shows that we cover a wide range of parameter space that has not previously been studied in detail. In particular, in regions of similar metallicities that have been studied previously, we also sample different σ and density regions.

2.2 Observing Strategy

These objects were observed over several nights in April 2016, October 2016, and April 2017, obtaining optical and red spectroscopy with the Low Resolution Imaging Spectrometer (LRIS, Oke et al. 1995; McCarthy et al. 1998; Rockosi et al. 2010) on the Keck I telescope at the W. M. Keck Observatory. Observation dates and exposure times are indicated in Table 2.1.

LRIS is an instrument for visible-wavelength imaging and spectroscopy (Oke et al. 1995). It consists of CCD detectors covering the blue and red wavelength ranges, respectively. Both cameras have a pixel scale of 0.135"/pixel. The 680 nm dichroic was used to split the light between the blue and red arms. On the blue side, the 300 lines/mm grism blazed at 5000 Å was used to give a spectral wavelength coverage of $\sim 3500 - 7500$ Å. On the red side, the 600 lines/mm grating blazed at 10 000 Å was used to give a spectral wavelength coverage of $\sim 7300 - 10600$ Å. We made use of each of the 0.7"- and 1.0"-width, 3'-long, long slits, as indicated in Table 2.1. Slit widths were chosen based on the apparent size of each object. The spectral full-width-at-half-maximum resolution is 8.4-9.2 Å and $\sim$ 4.7 Å for the blue and red arms, respectively, for a 1 slit width. The fraction of R_e that our apertures encompass for each object is indicated in Table 2.1.

Table 2.1 Observing parameters for the objects in our study. In the R_e column, the fraction of R_e that our aperture encompasses is indicated in brackets. References: (d) Federici et al. (2012); (e) From NED; (f) Holland (1998); (g) Paturel & Garnier (1992); (h) Mei et al. (2007); (i) Mieske et al. (2013); (j) Tully et al. (2016); (k) Peacock et al. (2010); (l) Strader et al. (2011); (m) Barmby et al. (2007); (n) Barmby (2010); (o) Sandoval et al. (2015); (p) Greene et al. (2019); (q) Galleti et al. (2004); (r) Paudel et al. (2010); (s) Kim et al. (2014); (t) Abazajian et al. (2009).

ID	RA	Dec	Type	Date(s) Observed	Slit	Exposure (s)	Blue S/N (Å^{-1})[a]	Red S/N (Å^{-1})[b]	Distance (Mpc)	R_e (pc)	r-Band Magnitude
B012	00:40:32.54	+41:21:44.3	GC	28/10/16	1.0”	1300	118	89	0.73[d]	3[k](0.44)	14.83 ± 0.02[k]
B058	00:41:53.06	+40:47:09.9	GC	20/12/14[c], 28/10/16	0.7”, 1.0”	4300, 900	246	208	0.74[d]	2.07[k](0.64)	14.71 ± 0.02[k]
B067	00:42:03.14	+41:04:23.7	GC	27/10/16	1.0”	2700	137	113	1.2[e]	1.48[k](0.37)	16.99 ± 0.05[k]
B074	00:42:08.04	+41:43:21.7	GC	29/10/16	1.0”	1350	145	106	0.783[f]	2.91[k](0.45)	16.37 ± 0.03[k]
B107	00:42:31.22	+41:19:38.9	GC	28/10/16	1.0”	720	128	95	0.783[f]	2.7[l](0.48)	15.48 ± 0.02[k]
B163	00:43:18.10	+41:28:04.2	GC	19/12/14[c]	0.7”	4300	108	98	1.02[g]	3[k](0.44)	14.65 ± 0.02[k]
B193	00:43:45.42	+41:36:57.4	GC	19/12/14[c]	0.7”	4300	317	248	0.61[g]	2.03[k](0.69)	14.95 ± 0.03[k]
B225	00:44:29.82	+41:21:36.6	GC	27/10/16	1.0”	450	143	123	0.81[d]	2.12[k](0.63)	13.82 ± 0.02[k]
B338	00:40:58.83	+40:35:48.0	GC	29/10/16	1.0”	540	286	267	0.73[d]	4.33[m](0.31)	13.93 ± 0.02[k]
B405	00:49:39.82	+41:35:29.7	GC	29/10/16	1.0”	600	243	203	0.83[d]	3.83[m](0.35)	14.88 ± 0.02[k]
G001	00:32:46.57	+39:34:40.6	GC	28/10/16	1.0”	540	167	130	0.82[d]	3.23[m](0.41)	13.208[q]
M59-UCD3	12:42:10.99	+11:38:41.6	UCD	20/12/14[c]	0.7”	4300	293	288	14.9[h]	20[o](4.75)	16 ± 0.05[o]
VUCD3	12:30:58.02	+12:25:51.5	UCD	19/04/17	0.7”	1800	59	60	16.5[i]	21.6[i](3.99)	18.1[r]
VUCD4	12:31:04.93	+11:56:38.2	UCD	19/04/17	0.7”	3600	80	68	16.5[i]	23.6[i](3.21)	18.6[r]
VUCD7	12:31:53.42	+12:15:54.3	UCD	19/04/17	1.0”	2400	121	101	16.5[i]	105[i](1.03)	17.34[s]
NGC 4874	12:59:35.68	+27:57:43.8	BCG	19/04/17	0.7”	270	84	78	104.71[j]	13600[p] (0.07)	12.101 ± 0.002[t]
NGC 4889	13:00:08.36	+27:58:47.4	BCG	19/04/17	0.7”	270	133	127	92.04[j]	19200[p] (0.11)	11.976 ± 0.002[t]

[a]Median S/N over the blue wavelength regions that we fit.

[b]Median S/N over the red wavelength regions that we fit.

[c]Data analyzed in V17.

2.3 Data Reduction

We reduce the data for each object using the semi-automated reduction package PypeIt[1], version 1.5 (Prochaska et al. 2020b; Prochaska et al. 2020a). In general, the reduction follows standard procedures, including overscan bias subtraction and slit tracing via flat field images. We do not perform flat fielding.

In the following sections, we detail the aspects of the data reduction that we treat with particular care due to the sensitivity of full-spectrum fitting in general and IMF results in particular to systematics in the data. For example, near-perfect (Poisson-limited) sky subtraction and telluric correction are necessary, to correct systematic uncertainties as robustly as possible and have a thorough understanding of any remaining statistical and systematic uncertainties. This is because the IMF only impacts spectral features at a level of $\sim 1-3\%$ (see, e.g. Smith 2020). Additionally, several of the most important IMF-sensitive features are near or overlap with sky lines (e.g. NaD near ~ 5900 Å) and/or regions heavily affected by telluric absorption (e.g. NaI near ~ 8200 Å, Wing-Ford band).

2.3.1 Wavelength Solution

PypeIt produces a master arc frame using individual frames taken using all of the Keck arc lamps (Hg, Cd, and Zn on the blue side and Ne, Ar, Kr, and Xe on the red side). These were taken for each night and instrument set up. We use this master arc frame for the wavelength calibration and to correct for spectral tilt (Prochaska et al. 2020a). We make several modifications to the default PypeIt wavelength solution, described below.

On the blue side, we use the `full_template` method with a polynomial of order $n = 5$, where arc spectra are cross-correlated against an archived template spectrum, with an algorithm to reduce non-linearities (Prochaska et al. 2020a). The resulting root mean square (RMS) of the residuals is between $\sim 0.14-0.31$ pixels ($\sim 12.6-28.0$ km/s).

To maintain consistency with the blue side, we alter the wavelength solution for the red frames as well, from the default `holy_grail` method (where detected lines are matched with those expected from observed arc lamps) to the `full_template` method. Since PypeIt does not have an archived template spectrum for the 600/10000 grating, we use PypeIt's interactive routine to manually produce a wavelength solution, which we then apply for all of our red side calibrations. This has now been included in the PypeIt code base. We find that the RMS of the residuals is similarly small, between $\sim 0.095-0.424$ pixels ($\sim 4.5-20.3$ km/s).

[1] https://pypeit.readthedocs.io/en/latest/ .

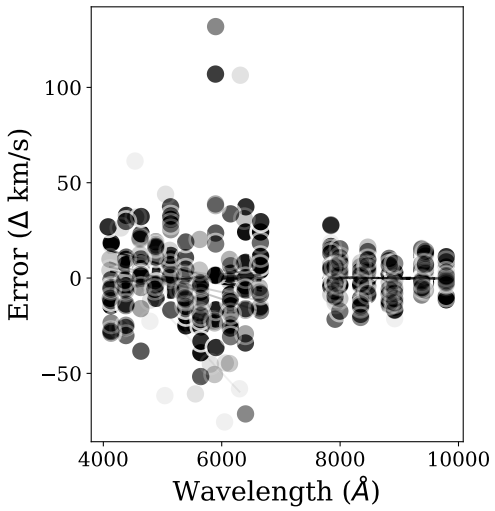

Figure 2.2 Remaining error in the wavelength solution as a function of wavelength, after flexure correction has been applied. Each object in our sample is shown as a series of grey points, to illustrate the range of wavelength solution errors. The absolute errors are relatively small ($\lesssim 150$ km/s) and are randomly scattered around ~ 0. This indicates that there is no longer a systematic pattern to the errors.

2.3.2 Flexure Correction

The wavelength solution is further corrected for spectral flexure. We do not use PypeIt's default, single-pixel shift flexure correction, as we find that a more complex, wavelength-dependent solution is required, based on examination of night sky emission lines.

On the red side, we compare the extracted sky spectrum from each object to a Paranal sky model (Noll et al. 2012; Jones et al. 2013), provided by PypeIt. We select 10 strong sky emission lines across the wavelength range and measure the centroids of the corresponding lines in the data and the model, using a Gaussian fitting routine. We find the differences between each set of centroids and fit a straight line to these deviations. This linear function is interpolated over the entire red wavelength range and subtracted from the wavelengths to produce a final, corrected wavelength array on the red side.

We cannot effectively perform this same procedure on the blue side due to a lack of strong sky emission lines at the bluest ends of our spectra, so instead we use a similar method as in van Dokkum & Conroy (2012). We create a template spectrum of the data with literature age and metallicity (see references in Table 4.5), using the `write_a_model` SSP framework in ALF. We split the template and our spectra into chunks of ~ 250 Å and compare these to measure the redshift in each chunk. Assuming the flexure is a linear function of the redshifted template wavelength, we fit a straight line to these redshifts and use this to solve for the coefficients in the flexure function. We shift our blue wavelengths by this flexure function to produce a final, flexure-corrected wavelength solution. For more details, see Appendix A.

In Figure 2.2, we show the remaining error in the wavelength solution after we apply the flexure correction. To produce this plot, we redo the redshift and centroid measurements on the blue and red sides, respectively, after we apply the flexure correction. The "errors" on the y-axes are the redshifts for the blue flexure correction procedure and the centroid differences for the red flexure correction procedure, respectively, converted to km/s. It is evident that the wavelength-dependence has been largely removed, as any remaining trend with wavelength is small compared with the random scatter around ~ 0. We also compare the flexure-corrected sky emission lines to the expected values and find that they are now consistent within measurement uncertainties.

2.3.3 Sky Subtraction

Prior to extracting the one-dimensional spectra of the objects, we perform sky subtraction. PypeIt first executes a global sky subtraction, using a two-dimensional, Kelson (2003) b-

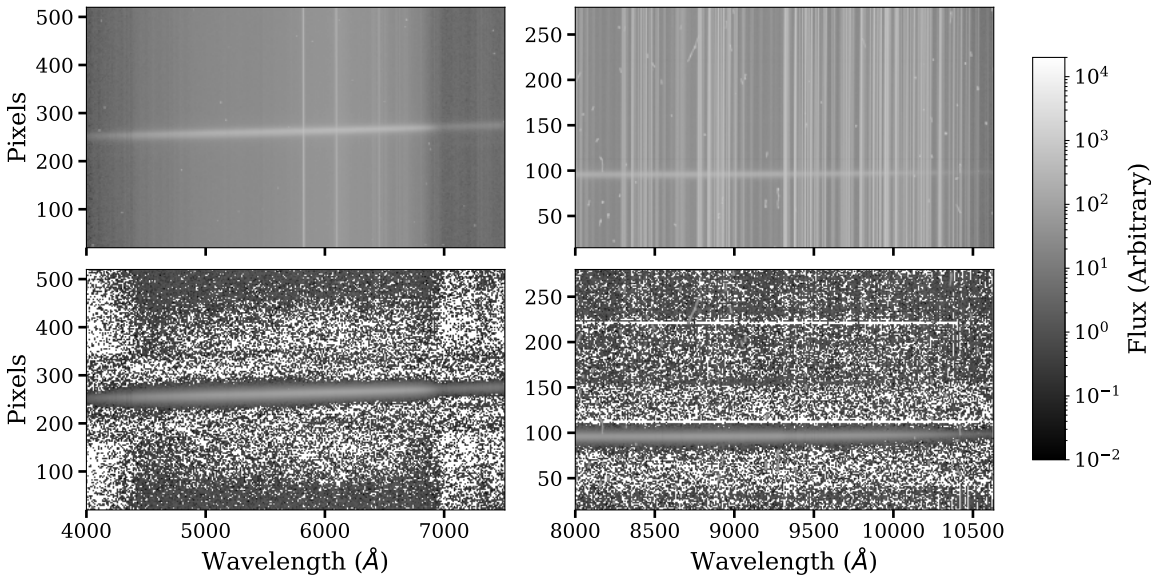

Figure 2.3 Examples of two-dimensional spectra from the 2016 B058 data. The left and right panels show the blue and red spectra, respectively, while the top and bottom panels show the spectra before and after sky subtraction. The horizontal strips represent the object traces. The bright vertical lines represent sky emission lines. In the bottom panels, the sky lines are well-subtracted and largely not visible across the object traces.

spline algorithm. Here, the background is well-sampled and accurately modeled by making use of information about camera distortions and spectral curvature. This method is insensitive to bad pixels (e.g. cosmic rays, hot pixels, etc.), making the cleaning of such pixels simple after the sky subtraction is complete (Kelson 2003). The sky model is then locally refined around the science target during object extraction (Prochaska et al. 2020a). This is done by interpolating sky regions on either side of the object trace and fitting a weighted least-squares polynomial to the sky background at each wavelength, with weights inversely proportional to the variances of individual sky pixels (Horne 1986).

In Figure 2.3, we show examples of two-dimensional spectra from the 2016 B058 data. The left panels show the blue spectra and the right panels show the red spectra. The top and bottom panels show the spectra before and after sky subtraction, respectively. In each panel, the bright, horizontal strips represent the object traces while the bright vertical lines represent sky emission lines. In the top panels, many strong sky lines cross the object traces, particularly in the red. However, these are largely very well-subtracted in the bottom panels, with a uniform background near the traces and very few lines being visible across the traces themselves.

2.3.4 Object Extraction

To extract objects, the Horne (1986) algorithm is used. In summary, the sky-subtracted image is summed over the pixels covered by the object, with nonuniform pixel weights applied to minimize statistical noise and retain photometric accuracy. The object profile is fitted with a polynomial. This accurate characterization of the spatial profile across the wavelength range allows the algorithm to accurately correct for cosmic rays, as a cosmic ray event results in a distortion of the object profile that can be easily recognized and masked. For some of our bright sources, we find that this can lead to excessive masking of key spectral features ($\gtrsim 10\%$ of pixels, Prochaska et al. 2020a). To avoid this, we increase the threshold for the cosmic ray rejection where necessary, until $\lesssim 10\%$ of pixels are masked and masked pixels are randomly scattered across the object trace. For particularly bad cases (i.e. where increasing the cosmic ray rejection threshold indefinitely does not reduce the masking), we suppress the masking entirely.

2.3.5 Flux Calibration and Co-addition

We do not flux calibrate the data. This is primarily because ALF does not require spectra to be fluxed, as we subtract the continuum prior to fitting them (see Section 3).

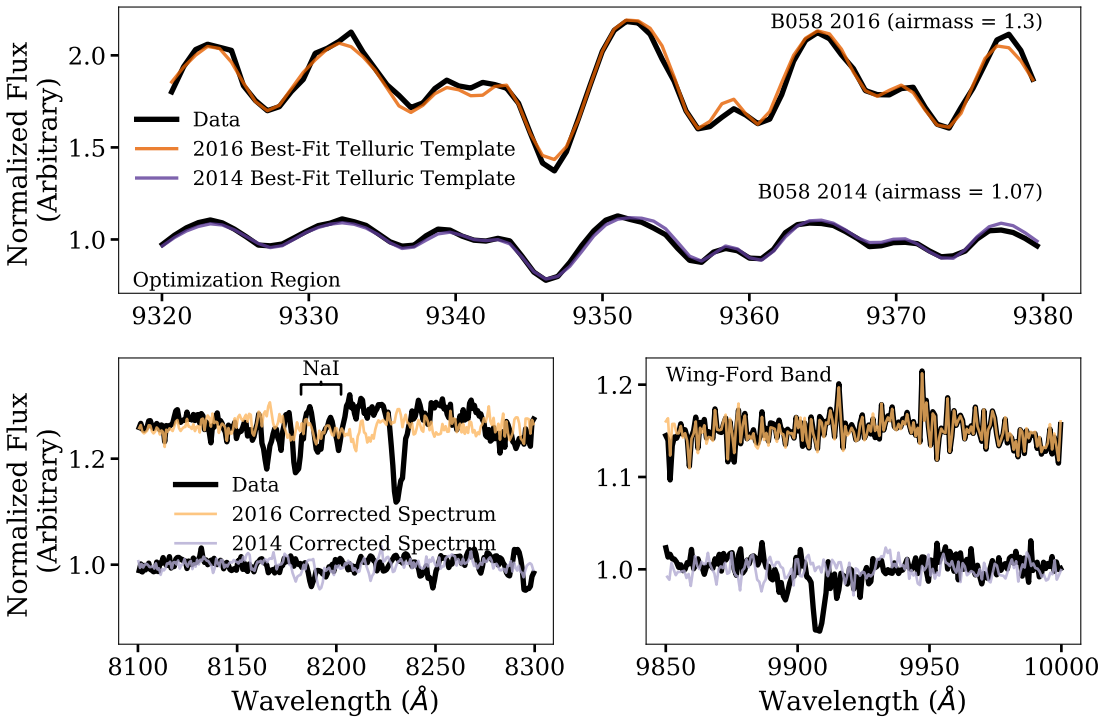

Figure 2.4 A demonstration of our telluric correction procedure. In the top panel, we show the normalized 2016 and 2014 B058 spectra, prior to telluric correction (black lines), as well as that for the 2014 B058 spectrum (black lines), over the narrow wavelength range containing many strong telluric lines that we use to select the atmospheric template. We compare each to the best-fitting template (dark orange for 2016/dark purple for 2014). In the bottom panels, we show the spectra prior to telluric correction compared to the final, corrected spectra (light orange for 2016/light purple for 2014). The left panel shows the spectra near the NaI spectral feature and the right panel shows them over the Wing-Ford band. Each set of spectra is arbitrarily shifted vertically, for clarity.

After the main reduction process, we use PypeIt's external co-adding routine to combine all of the one-dimensional spectra for each of our target objects, on each of the blue and red sides. This is done by optimally weighting each one-dimensional spectrum by its S/N at each pixel. The spectra are also cleaned of cosmic rays again at this stage, by scaling the fluxes using the root mean square of the squared S/N (Prochaska et al. 2020a). This combination step leaves us with one spectrum for each of the blue and red sides of each object that we analyze.

2.3.6 Telluric Correction

We tellurically-correct the spectra using a modified version of the method in van Dokkum & Conroy (2012). In summary, we scale a template spectrum to the observed atmospheric absorption, where the scaling is parameterized by Equation (2) in van Dokkum & Conroy (2012). We smooth each template spectrum from the Mauna Kea telluric grids included with PypeIt, originally produced via the Line-By-Line Radiative Transfer Model[2] (Clough et al. 2005; Gullikson et al. 2014), to the LRIS instrumental resolution and scale each of them. We divide each of the scaled template and target spectra by a polynomial of order 4 over the region $9250 - 9650$ Å to continuum-normalize them. We choose the best-fitting template by minimizing the χ^2 of the difference between each scaled template and target spectra, over the optimization region $9320 - 9380$ Å (which contains many strong atmospheric absorption lines and no strong galaxy absorption features). This best-fitting template is used to divide the target spectrum to produce the final, corrected spectrum. See van Dokkum & Conroy (2012) for details.

We demonstrate our telluric correction procedure in Figure 2.4. At the top of each panel, we show the arbitrarily shifted, continuum-normalized 2016 B058 spectrum prior to telluric correction, and at the bottom we show that for the 2014 B058 spectrum (black). In the top panel, we compare each spectrum to the best-fitting template, with the minimum χ^2 of the difference between the scaled template and target spectrum. In the bottom panel, we compare each spectrum prior to telluric correction to the final, corrected spectrum, over regions with strong telluric and stellar absorption features (e.g. near NaI and the Wing-Ford band). Both sets of data are fit well by the scaled template over all regions, with many atmospheric features being divided out. This allows us to more easily identify important spectral features.

[2] http://rtweb.aer.com/lblrtm.html .

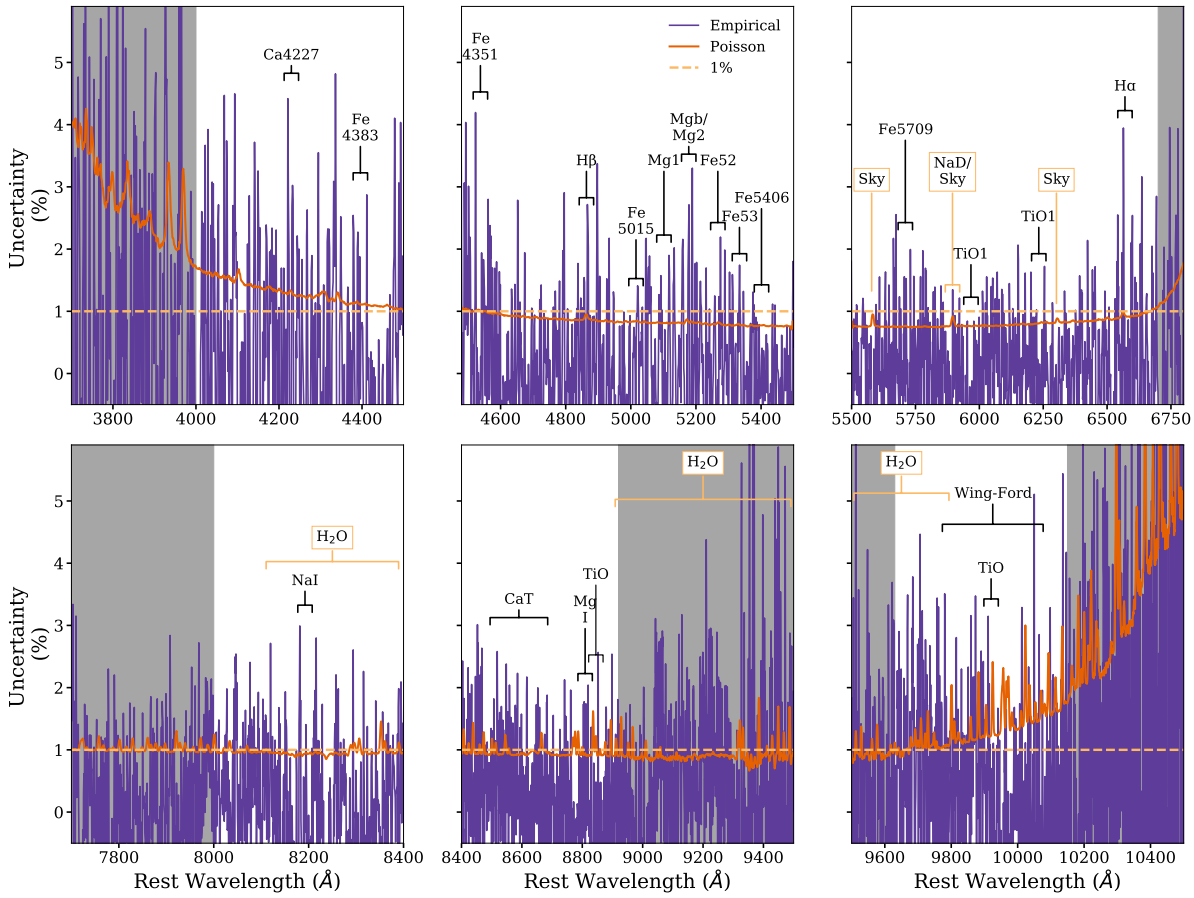

Figure 2.5 Quadrature sum of the Poisson uncertainties in the 2014 and 2016 B058 spectra (dark orange) compared to the empirical uncertainties between the two dates (purple). The dashed light orange line indicates 1% uncertainty. Prominent telluric and sky features are labelled in light orange and spectral features of interest are labelled in black. The grey regions indicate areas of the spectra that we do not fit or use in our analysis. In the areas of the spectra relevant for fitting and analysis, the empirical uncertainties are largely comparable to the Poisson uncertainties. In areas where the empirical uncertainties are larger, we are still able to constrain the majority of them to $\lesssim 5\%$.

2.3.7 Data Reduction Quality

We demonstrate the quality of our data reduction in Figure 2.5. Here, we compare the quadrature sum of the Poisson statistical uncertainties of observations of B058 from the two different dates (the 2014 data analyzed in V17 but newly reduced here and our new 2016 data, in orange), and the empirical or systematic uncertainties between the two observations (purple). Specifically, the Poisson statistical uncertainties represent the idealized uncertainties in the spectra (from photon counting and data calibrations), while the systematic uncertainties represents the systematics in our data (e.g. bad sky subtraction and telluric correction). The grey regions indicate areas of the spectra that we do not fit. In most areas of the spectra that are important to our analysis, the empirical uncertainties are comparable to the Poisson uncertainties, and that uncertainties are close to $\sim 1\%$ (dashed light orange line) at most wavelengths. Even in areas where our empirical uncertainties are larger than the Poisson expectation, they are still $\lesssim 5\%$ across the majority of the spectra.

There are certain key areas to point out specifically. For example, as discussed above, a sky line lies directly on top of the NaD feature near ~ 5900 Å. Even though this sky line contributes noise to the NaD feature, we are able to constrain the empirical uncertainty to be at a level of $\lesssim 2\%$. Similarly, we are able to characterize the uncertainty well at other key spectral features (labelled in black) and near sky emission and atmospheric absorption features (labelled in light orange), as well as across the entire spectrum. This demonstrates that any remaining systematic uncertainties are $\lesssim 1\%$.

Chapter 3

Methods

To model our data and derive stellar parameters, we fit the spectrum of each object with ALF[1], a full spectrum SPS model developed in Conroy & van Dokkum (2012a) and updated in Conroy et al. (2018) with expanded stellar parameter coverage. The empirical SSPs that underpin the ALF model were created with the MIST isochrones (Choi et al. 2016) and the Spectral Polynomial Interpolator (SPI, Villaume et al. 2017b)[2]. With SPI, we use the MILES optical stellar library (Sánchez-Blázquez et al. 2006), the Extended IRTF stellar library (E-IRTF, Villaume et al. 2017b), and a large sample of M dwarf spectra (Mann et al. 2015) to create a data-driven model from which we can generate stellar spectra as a function of $T_{\rm eff}$, surface gravity, and metallicity.

The empirical parameter space is set by the E-IRTF and Mann et al. (2015) samples, which together span $-2.0 \lesssim$ [Fe/H] $\lesssim 0.5$ and $3.9 \lesssim \log(T_{\rm eff}) \lesssim 3.5$. To preserve the quality of interpolation at the edges of the empirical parameter space, we augment the training set with a theoretical stellar library (C3K). The ALF models allow for variable abundance patterns by differentially including theoretical element response functions. We use the measured Mg abundances for the MILES stellar library stars from Milone et al. (2011) to derive the [Mg/Fe] versus [Fe/H] relation in our model.

ALF continuum-normalizes the target spectrum by multiplying the model by a high-order polynomial to match the shape of the continuum of the data. In particular, the ratio of the data and the model is fit by a polynomial of order n, where $n = (\lambda_{\rm max} - \lambda_{\rm min})/100$Å. The specific form of the polynomial is $p(\lambda) = \sum_{i=0}^{n} c_i(\lambda - \mu)^i$, where μ is the

[1] https://github.com/cconroy20/alf .

[2] https://github.com/AlexaVillaume/SPI_Utils .

mean wavelength of the region being fit. The polynomial coefficients c_i are determined by a least squares minimization and are re-fit during each iteration (Conroy et al. 2018).

ALF then samples the posteriors of 46 stellar parameters using a Fortran implementation of the Markov chain Monte Carlo (MCMC) algorithm `emcee` (Foreman-Mackey et al. 2013), allowing for arbitrary variation in the IMF, a two-component stellar age, and detailed chemical abundance patterns. It also fits for systematic parameters to characterize observed errors. In particular, a step is taken in parameter space, and this step is accepted if the new location as a lower χ^2 value compared to the previous location. Conversely, it is accepted with a certain probability if the χ^2 value is higher than the previous location. Each step in the chain is recorded, and after a "sufficient" ($\sim 10^5$ to achieve convergence in all parameters) number of steps, the chain will converge to the true underlying likelihood. The burn-in region, or the chain descending to the minimum χ^2, is discarded prior to analysis. In order to limit the parameter space, priors on the model parameters are specified. Outside of the prior range, the χ^2 is penalized by a Gaussian with a width of 0.01. However, note that these adopted priors do not have a significant impact on the fit results because the parameters are always well constrained within the prior range. For more details, see Conroy & van Dokkum (2012a) and Conroy et al. (2018).

We fit our data as in V17, using 512 walkers, 25,000 burn-in steps, and a 1,000 step production run. For all objects in our sample, we fit for the two slopes of a double PL IMF shape, with a break point at $m = 0.5\mathrm{M}_\odot$ and a fixed low-mass cutoff (m_c) at 0.08 $\mathrm{M}_\odot$. Above 1.0 $\mathrm{M}_\odot$, the IMF slope is assumed to have the Salpeter (1955) value of 2.35:

$$\frac{dN}{dm} = \begin{cases} k_1 m^{-\alpha_1}, & 0.08 < m < 0.5 \\ k_2 m^{-\alpha_2}, & 0.5 < m < 1.0 \\ k_3 m^{-2.3}, & m \geq 1.0 \end{cases} \tag{3.1}$$

k_1, k_2, and k_3 are normalization constants that ensure the IMF is continuous and they are not parameters for which we fit. This parameterization is widely used as it is the original form reported by Kroupa (2001) (the difference being that we allow α_1 and α_2 to vary while values of all slopes are fixed for a Kroupa (2001) IMF). For a MW IMF, we use the Kroupa (2001) values of $\alpha_1 = 1.3$ and $\alpha_2 = 2.3$. We show some different examples of this IMF parameterization in Figure 3.1, in particular a Kroupa (2001) IMF (dashed black), a bottom-heavy IMF (purple), and a bottom-light IMF (orange). The shaded regions demonstrate the break-points in the 2PL parameterization in Equation 3.1. These curves are normalized to the same total stellar mass.

As a caveat, note that we may not be able to differentiate a bottom-light IMF from a MW IMF as reliably as for a bottom-heavy one. To identify bottom-heaviness, we

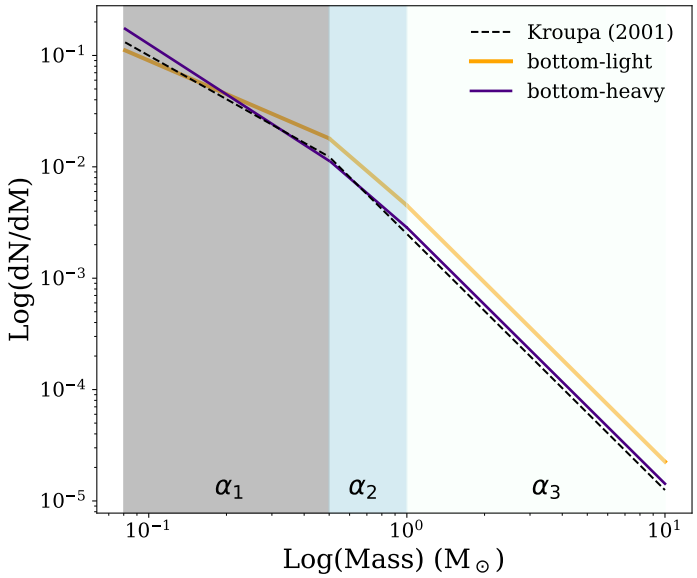

Figure 3.1 Examples of different characterizations of the IMF parameterization in Equation 3.1, as a function of stellar mass. The Kroupa (2001) IMF is shown by the dashed black line, a bottom-heavy characterization is shown in purple, and a bottom-light characterization is shown in orange. The shaded regions indicate the break-points of the 2PL, labelled by their slopes $(\alpha_1, \alpha_2, \alpha_3)$. These curves have been normalized to the same total stellar mass. The logarithmic nature of the axes means that there are more low-mass stars than high-mass stars depicted here.

search for stronger M dwarf-sensitive features and interpret this as an indication of more low-mass stars. The robustness of this method has been tested extensively (e.g. Conroy & van Dokkum 2012b; Villaume et al. 2017a; Newman et al. 2017; Conroy et al. 2017). However, it is unclear if *weaker* M dwarf-sensitive features can be interpreted to indicate *fewer* low-mass stars.

The intrinsic resolution of our CSSs is higher than the ALF models, which have a common resolution of $\sigma = 100$ km/s. To account for this, we broaden the spectra of the CSSs similar to V17, by 200 km/s (but see Appendix B for how different broadening values can affect our results). In particular, we use a modified version of the PROSPECTOR `smoothspec`[3] function, which uses Fast Fourier Transform convolutions to smooth the spectrum by a wavelength-dependent line-spread function. Using a model spectral library, the function generates a model spectrum and then smooths at each model generation step by the difference between the observed-frame instrumental resolution and the rest-frame library resolution. This is calculated for the model systemic velocity, velocity dispersion, and the instrumental line-spread function parameters. In this routine, it is assumed that the instrumental and library resolutions are approximated by a Gaussian at each wavelength, so the difference kernel can also be represented by a wavelength-dependent Gaussian. Then, the model spectrum is resampled onto a space in which the kernel is not varying with wavelength. See Johnson et al. (2021) for more details. To smooth by 200 km/s, we define the desired resolution to be 200 km/s. Prior to smoothing, we mask out and interpolate over any unphysical artefacts in the data. We broaden the blue and red sides individually so that the discontinuity in the centre of the spectrum is not interfering with adjacent spectral features. Broadening is not required for the BCGs, since their intrinsic resolution is lower than that of the ALF models.

We note that velocity dispersion is also a model parameter in ALF. In each case, during each MCMC step in the fitting procedure, ALF adjusts the velocity dispersion of the models to better fit the data (Conroy & van Dokkum 2012a; Conroy et al. 2018). In this way, the resolution of the data and the models during the fits will be equivalent. Thus, the CSSs must be broadened prior to fitting because otherwise the models will not be able to match the data. However, this means that ALF cannot be used to measure the actual velocity dispersions of these objects. On the other hand, the velocity dispersions of the BCGs can be estimated using ALF (though these must be added in quadrature to 100 km/s due to the native resolution of the ALF models).

We fit all of the objects in our sample over the wavelength ranges indicated in Figure 2.5. We show the fit residuals for the CSSs (GCs and UCDs) in the top panels of Figure 3.2 as a

[3] https://prospect.readthedocs.io/en/latest/api/utils_api.html .

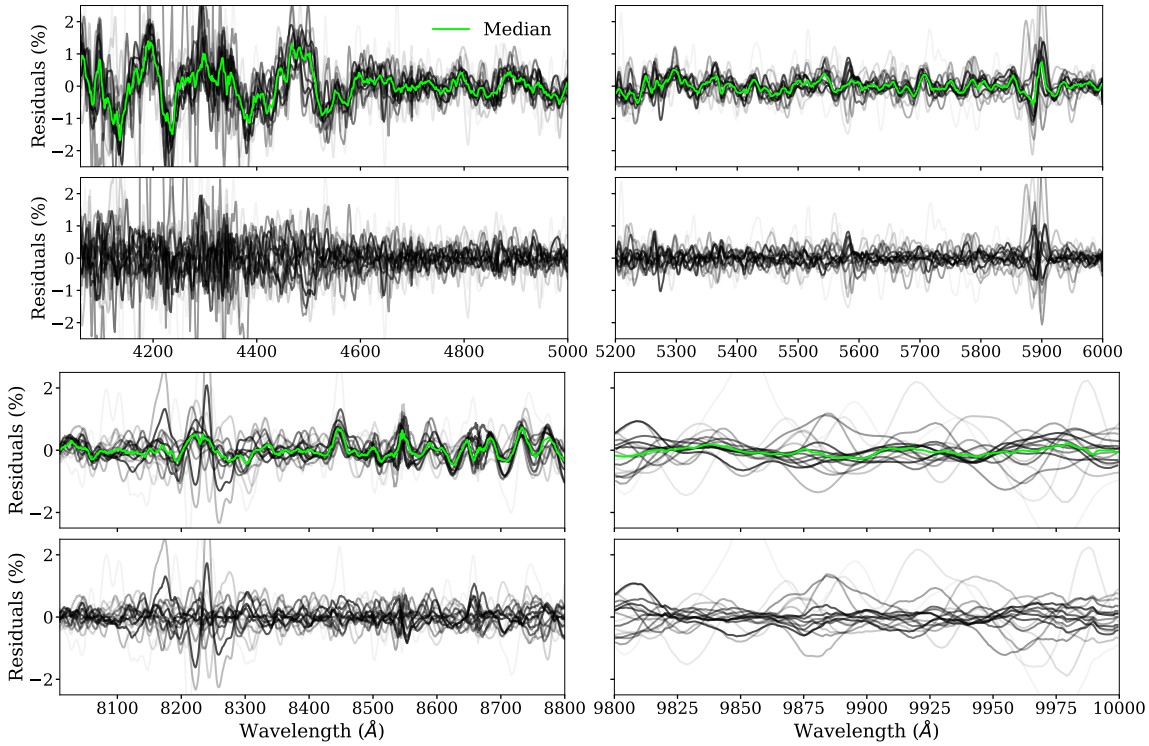

Figure 3.2 *Upper panels*: ALF model fit residuals for all CSSs, shown as a series of grey lines, ordered from lightest to darkest by increasing S/N. The median residual is shown in green. *Lower panels*: The same as the upper panels, but with the green median line subtracted. This allows us to examine the true variation in the spectra (i.e. not from the ALF models) on an individual object basis. The residuals near the NaD ($\sim$ 5900 Å) and NaI ($\sim$ 8200 Å) features are relatively large and structured, indicating that we do not model this variation well near these features.

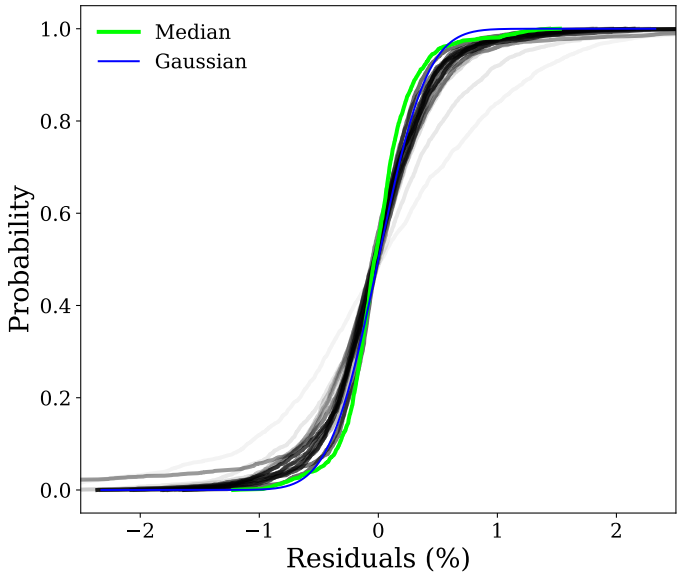

Figure 3.3 Cumulative distributions of the ALF model fit residuals for all CSSs, shown as a series of grey lines, ordered from lightest to darkest by increasing S/N. The cumulative distribution of the median residual is shown in green. A Gaussian cumulative distribution is shown in blue for comparison, with a mean of zero and a standard deviation equal to the standard deviation of the green median residual line.

series of grey lines, ordered from lightest to darkest by increasing S/N. The median residual is highlighted in green. In the lower panels, we show the median-subtracted residuals (i.e. the top panels, but with the green line subtracted out), which represents the "residuals of the residuals". In this way, we remove any systematic variations that result from the ALF models themselves, since all of our data were obtained with the same instrumental set-up and fit in the same way, and show the true variations in the spectra on an object-by-object basis. In Figure 3.3, we also show the cumulative distributions of the residuals from Figure 3.2. A Gaussian cumulative distribution is shown in blue for comparison, with a mean of zero and a standard deviation equal to the standard deviation of the green median residual line. Overall, our residuals are very small, and less than 2% over the entire spectral range. Additionally, for the majority of our objects, the cumulative distributions are steep and centred around zero. The residuals have a tail that is indicative of non-Gaussian, systematic noise, but this is limited to $< 1\%$ so the effect is small. This indicates that the fit residuals lie at or near zero and the ALF models fit the data well. This variation is well within the bounds of the expected about of variation introduced by different IMFs. The largest residuals are around the NaD (~ 5900 Å) and NaI (~ 8200 Å) features, which are still only at the 2% level. However, these Na features have been historically problematic in previous full-spectrum SPS studies (i.e. Conroy & van Dokkum 2012b; Newman et al. 2017). To be conservative, we fit the spectra with and without NaD and NaI included. We show the fits with the Na features included in Appendix B. We use the fits excluding the Na features in the rest of our main analysis.

Chapter 4

Results

We show some examples of our fits for G001 in Figure 4.1 and M59-UCD3 in Figure 4.2, as examples for a GC and a UCD, respectively. We also demonstrate our fits to the BCGs in Figure 4.3 for NGC 4874 and Figure 4.4 for NGC 4889, to highlight our comparison with the analysis in Z17 for the same objects. Similar figures for all remaining objects are shown in Appendix C. In the upper panels, we show the fully-reduced spectra for each object, along with a fit where we allow for a variable IMF (blue) and a fit where we fix a MW IMF (red). In the lower panels, we show the residuals for each fit. The residual uncertainties for the variable IMF fit are indicated by the grey bands. We highlight key, IMF-sensitive absorption features in the inset panels over the red wavelength regions. We also show the cumulative distributions of each fit in the upper right panel inset. A Gaussian cumulative distribution is shown for reference, with a mean of zero and with a standard deviation equal to the standard deviation of the distribution for the fit with a variable model (dashed black line). In general the models qualitatively provide a good fit to the spectrum overall and the key features.

We report the results of our fits in Table 4.1. Here we list our fitted [Fe/H], age, [Mg/Fe], V-band $(M/L)_*$ allowing for a variable IMF, and V-band $(M/L)_*$ where we fix a MW IMF. We also fit several other stellar parameters, which are listed in Tables 4.2, 4.3, and 4.4.

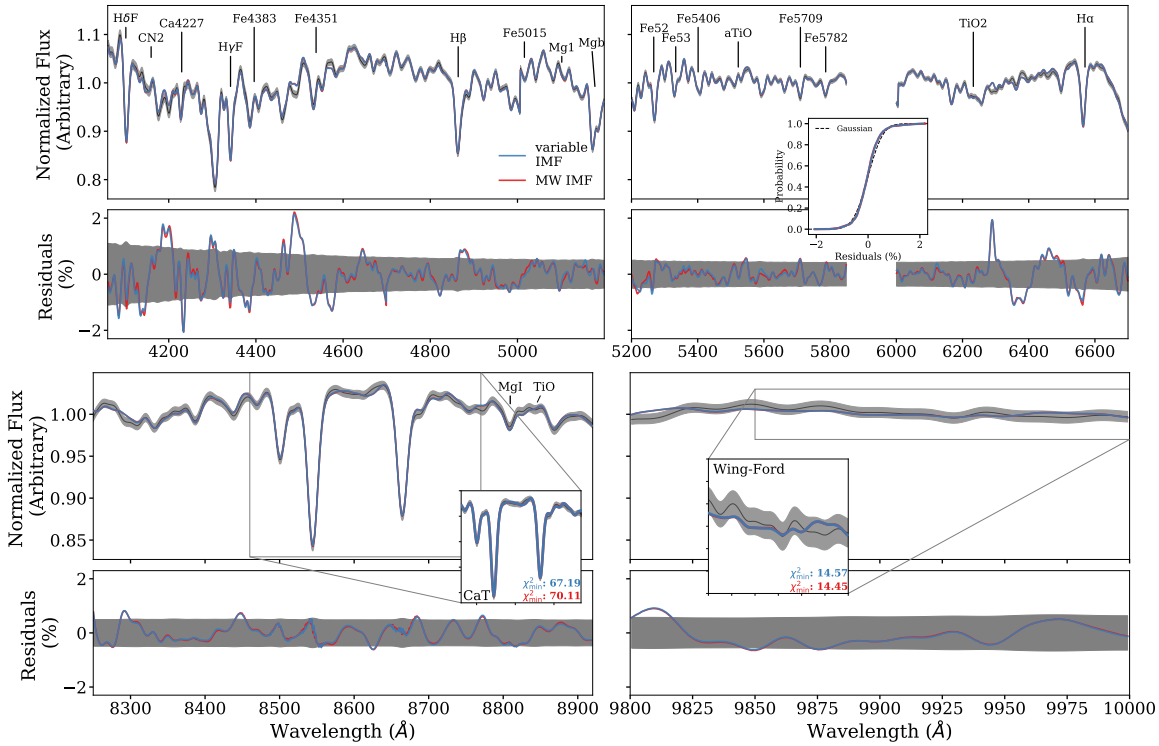

Figure 4.1 *Upper panels*: The best-fit ALF models for G001 (GC) over the fitted wavelength regions. The data are shown in black and the grey bands indicate the spectral uncertainties. A fit allowing for a variable IMF is shown in blue and a fit where we fix a MW IMF is shown in red. IMF-sensitive features and the $\chi^2_{\rm min}$ over these features for each respective fit are shown in the inset panels over the red wavelengths. In the upper right panel, the cumulative distributions of the residuals are shown inset for each fit. A Gaussian cumulative distribution is shown as a dashed black line for reference, with a mean of zero and with a standard deviation equal to the standard deviation of the distribution for the fit with a variable model. *Lower panels*: The corresponding fit residuals. The grey band indicates the uncertainty in the residuals for the variable IMF fit.

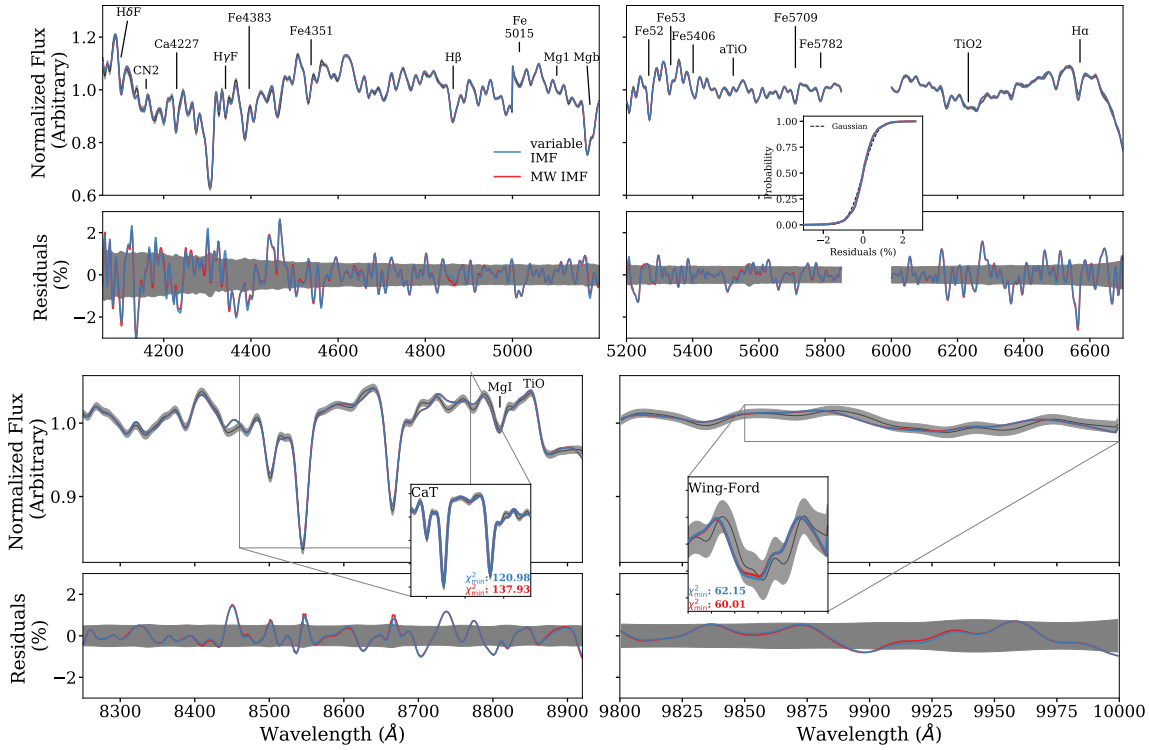

Figure 4.2 The same as Figure 4.1, but for M59-UCD3 (UCD).

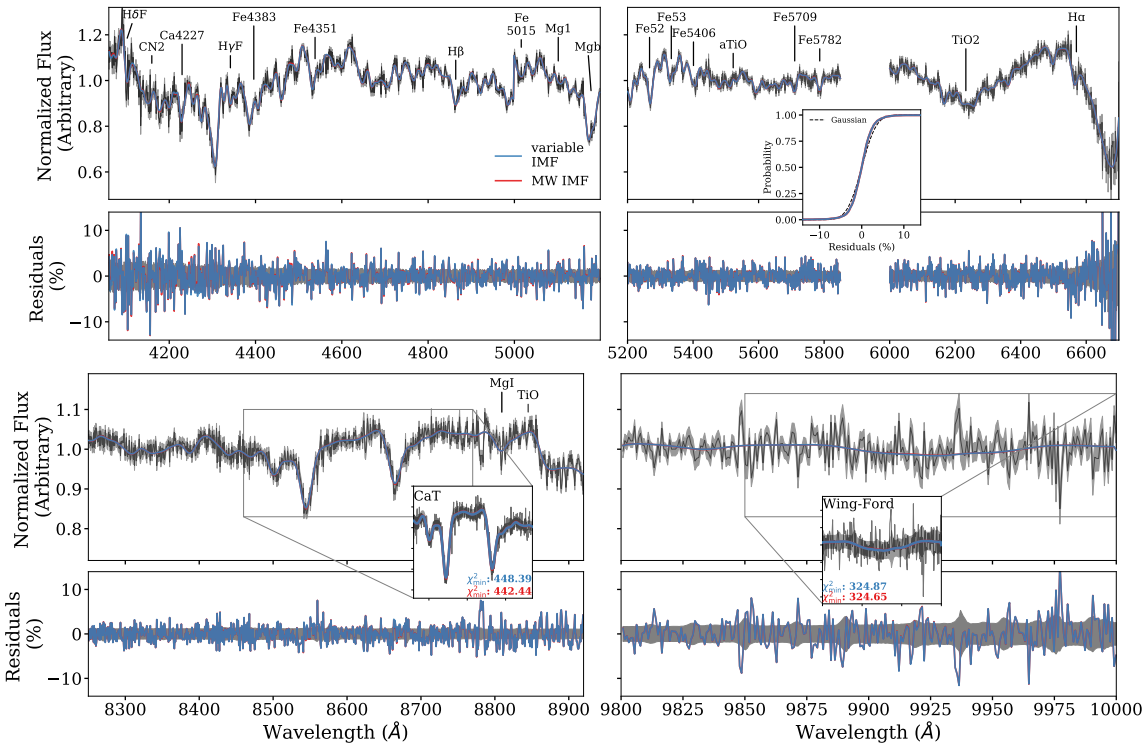

Figure 4.3 The same as Figure 4.1, but for NGC 4874 (BCG).

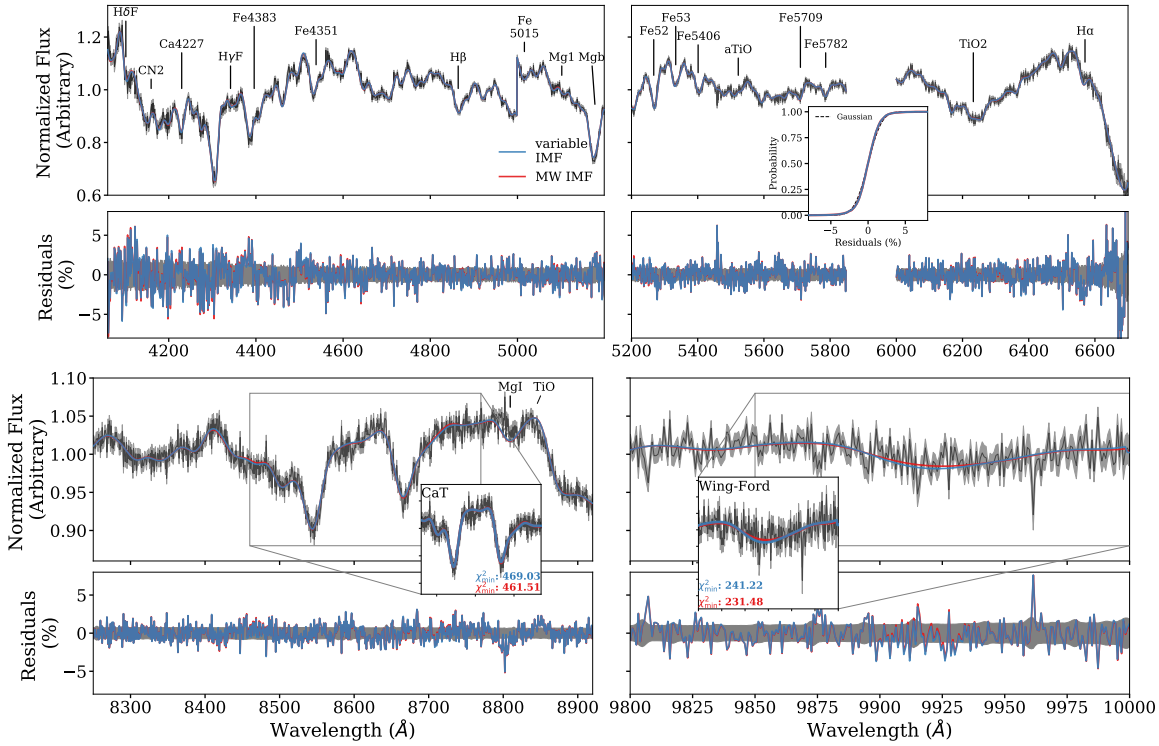

Figure 4.4 The same as Figure 4.1, but for NGC 4889 (BCG).

Table 4.1 Values of fitted parameters from ALF for all objects we examine.

ID	Age (Gyr)	[Fe/H]	[Mg/Fe]	M/L_v (2PL)	M/L_v (MW)
B012	$11.11^{+0.35}_{-0.28}$	$-1.68^{+0.03}_{-0.03}$	$0.33^{+0.03}_{-0.03}$	$1.66^{+0.13}_{-0.09}$	$2.14^{+0.06}_{-0.05}$
B058	$13.16^{+0.59}_{-1.03}$,	$-1.04^{+0.01}_{-0.03}$,	$0.36^{+0.02}_{-0.02}$,	$2.27^{+0.19}_{-0.16}$,	$2.7^{+0.07}_{-0.11}$,
(Original,	$13.65^{+0.26}_{-0.5}$	$-1.07^{+0.02}_{-0.02}$	$0.4^{+0.02}_{-0.02}$	$2.56^{+0.3}_{-0.23}$	$2.72^{+0.03}_{-0.06}$
New)					
B067	$13.74^{+0.19}_{-0.36}$	$-1.56^{+0.02}_{-0.02}$	$0.34^{+0.03}_{-0.03}$	$2.16^{+0.14}_{-0.09}$	$2.61^{+0.03}_{-0.05}$
B074	$12.28^{+0.61}_{-0.65}$	$-1.49^{+0.02}_{-0.03}$	$0.51^{+0.05}_{-0.05}$	$2.28^{+0.25}_{-0.28}$	$2.33^{+0.09}_{-0.09}$
B107	$12.82^{+0.87}_{-1.52}$	$-0.95^{+0.02}_{-0.03}$	$0.3^{+0.03}_{-0.03}$	$2.6^{+0.44}_{-0.38}$	$2.76^{+0.1}_{-0.19}$
B163	$10.92^{+0.39}_{-0.35}$	$-0.22^{+0.01}_{-0.01}$	$0.23^{+0.01}_{-0.01}$	$5.49^{+1.42}_{-1.34}$	$3.95^{+0.09}_{-0.08}$
B193	$13.41^{+0.39}_{-0.5}$	$-0.18^{+0.01}_{-0.01}$	$0.24^{+0.01}_{-0.01}$	$4.4^{+1.25}_{-0.92}$	$4.67^{+0.08}_{-0.12}$
B225	$11.41^{+0.49}_{-0.59}$	$-0.45^{+0.01}_{-0.02}$	$0.23^{+0.01}_{-0.01}$	$2.75^{+0.45}_{-0.28}$	$3.47^{+0.11}_{-0.11}$
B338	$13.76^{+0.18}_{-0.47}$	$-1.08^{+0.02}_{-0.11}$	$0.34^{+0.04}_{-0.04}$	$2.43^{+0.36}_{-0.21}$	$2.65^{+0.07}_{-0.07}$
B405	$11.12^{+0.32}_{-0.17}$	$-1.19^{+0.02}_{-0.02}$	$0.47^{+0.02}_{-0.02}$	$2.31^{+0.26}_{-0.25}$	$2.27^{+0.04}_{-0.03}$
G001	$13.66^{+0.26}_{-0.48}$	$-0.8^{+0.01}_{-0.01}$	$0.4^{+0.02}_{-0.02}$	$2.78^{+0.37}_{-0.31}$	$2.99^{+0.04}_{-0.06}$
M59-UCD3	$9.31^{+0.37}_{-0.85}$	$-0.02^{+0.01}_{-0.01}$	$0.19^{+0.01}_{-0.01}$	$4.55^{+1.22}_{-1.16}$	$4.03^{+0.11}_{-0.24}$
VUCD3	$13.48^{+0.35}_{-0.67}$	$-0.11^{+0.02}_{-0.02}$	$0.41^{+0.02}_{-0.02}$	$3.73^{+0.5}_{-0.34}$	$4.93^{+0.09}_{-0.14}$
VUCD4	$11.42^{+0.76}_{-1.29}$	$-1.04^{+0.02}_{-0.03}$	$0.42^{+0.03}_{-0.03}$	$1.9^{+0.15}_{-0.17}$	$2.42^{+0.09}_{-0.15}$
VUCD7	$13.82^{+0.14}_{-0.28}$	$-0.75^{+0.01}_{-0.01}$	$0.42^{+0.01}_{-0.01}$	$3.75^{+0.32}_{-0.3}$	$3.2^{+0.02}_{-0.04}$
NGC 4874	$12.69^{+0.88}_{-1.24}$	$0.0^{+0.02}_{-0.02}$	$0.31^{+0.02}_{-0.02}$	$5.98^{+1.21}_{-0.91}$	$5.36^{+0.21}_{-0.3}$
NGC 4889	$13.93^{+0.05}_{-0.14}$	$0.09^{+0.02}_{-0.01}$	$0.26^{+0.01}_{-0.01}$	$12.82^{+1.95}_{-1.92}$	$6.1^{+0.09}_{-0.08}$

Table 4.2 Values of other fitted parameters from ALF for all objects we examine.

ID	v_r[a](km/s)	$T_{\rm eff}$[b](K)	α_1[c]	α_2[d]
B012	$-354.6^{+2.02}_{-2.34}$	$0.08^{+1.24}_{-1.33}$	$0.96^{+0.42}_{-0.3}$	$0.8^{+0.13}_{-0.17}$
B058	$-212.06^{+1.18}_{-1.16}$,	$-0.41^{+1.59}_{-1.15}$,	$1.3^{+0.4}_{-0.48}$,	$0.79^{+0.19}_{-0.18}$,
(Original,	$-222.7^{+8.5}_{-0.38}$	$-0.33^{+1.48}_{-1.19}$	$1.68^{+0.3}_{-0.38}$	$0.84^{+0.31}_{-0.23}$
New)				
B067	$-348.75^{+0.78}_{-3.52}$	$-0.24^{+1.19}_{-1.31}$	$1.02^{+0.34}_{-0.32}$	$0.86^{+0.24}_{-0.24}$
B074	$-443.43^{+2.25}_{-1.99}$	$-0.19^{+1.39}_{-1.21}$	$1.88^{+0.32}_{-0.43}$	$0.79^{+0.23}_{-0.19}$
B107	$-330.66^{+0.52}_{-0.97}$	$0.02^{+1.35}_{-1.46}$	$1.8^{+0.5}_{-0.68}$	$0.84^{+0.26}_{-0.23}$
B163	$-166.89^{+1.31}_{-1.44}$	$-0.83^{+1.54}_{-0.89}$	$2.83^{+0.33}_{-0.49}$	$0.91^{+0.28}_{-0.26}$
B193	$-70.22^{+0.25}_{-0.49}$	$-0.46^{+1.48}_{-1.1}$	$2.03^{+0.51}_{-0.89}$	$0.97^{+0.37}_{-0.32}$
B225	$-164.27^{+1.31}_{-1.44}$	$-0.63^{+1.5}_{-0.98}$	$1.32^{+0.58}_{-0.56}$	$1.22^{+0.34}_{-0.4}$
B338	$-266.27^{+1.83}_{-1.93}$	$-0.15^{+1.37}_{-1.23}$	$1.33^{+0.53}_{-0.52}$	$1.4^{+0.58}_{-0.53}$
B405	$-164.48^{+1.45}_{-1.55}$	$-0.52^{+1.48}_{-1.13}$	$2.1^{+0.22}_{-0.33}$	$0.77^{+0.19}_{-0.18}$
G001	$-338.55^{+1.59}_{-1.24}$	$-0.55^{+1.44}_{-1.09}$	$1.74^{+0.35}_{-0.59}$	$0.92^{+0.42}_{-0.3}$
M59-	$379.54^{+1.06}_{-1.07}$	$-0.58^{+1.64}_{-1.07}$	$2.63^{+0.37}_{-0.59}$	$0.91^{+0.39}_{-0.27}$
UCD3				
VUCD3	$706.98^{+1.61}_{-1.16}$	$0.11^{+1.2}_{-1.56}$	$1.11^{+0.5}_{-0.44}$	$1.27^{+0.46}_{-0.52}$
VUCD4	$915.57^{+1.61}_{-0.91}$	$0.13^{+1.28}_{-1.49}$	$1.0^{+0.47}_{-0.32}$	$0.88^{+0.33}_{-0.24}$
VUCD7	$981.92^{+0.74}_{-0.46}$	$-0.71^{+1.45}_{-0.92}$	$2.28^{+0.18}_{-0.22}$	$0.95^{+0.34}_{-0.29}$
NGC 4874	$7156.86^{+1.02}_{-1.39}$	$-0.46^{+1.61}_{-1.09}$	$1.17^{+0.62}_{-0.46}$	$2.66^{+0.41}_{-0.51}$
NGC 4889	$6450.89^{+1.95}_{-2.59}$	$-1.06^{+1.4}_{-0.67}$	$2.37^{+0.27}_{-0.28}$	$2.71^{+0.25}_{-0.25}$

[a] Recession velocity in km/s.

[b] Effective temperature in K.

[c] Low-mass IMF slope.

[d] Intermediate-mass IMF slope.

Table 4.3 Values of other fitted chemical abundances from ALF for all objects we examine.

ID	[Ba/Fe]	[C/Fe]	[Co/Fe]	[Cr/Fe]	[Cu/Fe]	[Eu/Fe]	[K/Fe]
B012	$-0.22^{+0.18}_{-0.12}$	$0.09^{+0.03}_{-0.03}$	$0.19^{+0.13}_{-0.14}$	$0.06^{+0.05}_{-0.05}$	$0.18^{+0.24}_{-0.2}$	$0.1^{+0.29}_{-0.28}$	$0.15^{+0.25}_{-0.17}$
B058	$-0.46^{+0.16}_{-0.12}$,	$-0.11^{+0.02}_{-0.02}$,	$-0.01^{+0.07}_{-0.06}$,	$-0.05^{+0.03}_{-0.03}$,	$-0.06^{+0.17}_{-0.16}$,	$0.37^{+0.04}_{-0.08}$,	$0.2^{+0.15}_{-0.27}$,
(Original,	$-0.23^{+0.16}_{-0.19}$	$-0.1^{+0.02}_{-0.02}$	$0.1^{+0.08}_{-0.08}$	$-0.01^{+0.03}_{-0.04}$	$-0.01^{+0.2}_{-0.2}$	$0.23^{+0.13}_{-0.24}$	$0.15^{+0.19}_{-0.28}$
New)							
B067	$-0.34^{+0.08}_{-0.05}$	$0.13^{+0.02}_{-0.03}$	$0.39^{+0.08}_{-0.07}$	$-0.01^{+0.04}_{-0.03}$	$0.37^{+0.19}_{-0.17}$	$0.17^{+0.23}_{-0.21}$	$0.11^{+0.28}_{-0.16}$
B074	$-0.27^{+0.19}_{-0.15}$	$0.07^{+0.03}_{-0.04}$	$0.33^{+0.11}_{-0.12}$	$-0.08^{+0.05}_{-0.05}$	$0.24^{+0.21}_{-0.23}$	$0.29^{+0.2}_{-0.27}$	$0.14^{+0.29}_{-0.25}$
B107	$-0.21^{+0.19}_{-0.21}$	$-0.06^{+0.02}_{-0.03}$	$0.29^{+0.08}_{-0.08}$	$0.02^{+0.04}_{-0.03}$	$-0.0^{+0.22}_{-0.18}$	$0.33^{+0.12}_{-0.25}$	$0.03^{+0.28}_{-0.23}$
B163	$-0.53^{+0.03}_{-0.02}$	$-0.08^{+0.02}_{-0.02}$	$0.17^{+0.04}_{-0.03}$	$-0.03^{+0.02}_{-0.02}$	$0.44^{+0.08}_{-0.14}$	$0.5^{+0.04}_{-0.07}$	$0.31^{+0.17}_{-0.27}$
B193	$-0.58^{+0.07}_{-0.04}$	$-0.15^{+0.02}_{-0.02}$	$0.15^{+0.04}_{-0.04}$	$-0.14^{+0.02}_{-0.02}$	$0.36^{+0.08}_{-0.13}$	$0.43^{+0.03}_{-0.07}$	$0.25^{+0.17}_{-0.26}$
B225	$-0.44^{+0.09}_{-0.05}$	$-0.13^{+0.03}_{-0.02}$	$0.23^{+0.04}_{-0.03}$	$-0.01^{+0.02}_{-0.02}$	$0.37^{+0.14}_{-0.17}$	$0.55^{+0.04}_{-0.07}$	$0.21^{+0.26}_{-0.25}$
B338	$-0.37^{+0.19}_{-0.16}$	$-0.06^{+0.02}_{-0.04}$	$-0.02^{+0.11}_{-0.09}$	$-0.07^{+0.06}_{-0.04}$	$0.07^{+0.24}_{-0.22}$	$-0.38^{+0.25}_{-0.17}$	$0.04^{+0.27}_{-0.23}$
B405	$-0.5^{+0.16}_{-0.07}$	$-0.03^{+0.02}_{-0.02}$	$0.04^{+0.07}_{-0.07}$	$-0.05^{+0.03}_{-0.03}$	$0.01^{+0.19}_{-0.17}$	$-0.38^{+0.21}_{-0.16}$	$0.29^{+0.15}_{-0.27}$
G001	$-0.51^{+0.14}_{-0.09}$	$-0.0^{+0.01}_{-0.01}$	$0.17^{+0.06}_{-0.05}$	$-0.02^{+0.03}_{-0.02}$	$0.14^{+0.16}_{-0.18}$	$0.35^{+0.09}_{-0.17}$	$0.2^{+0.18}_{-0.31}$
M59-UCD3	$-0.38^{+0.11}_{-0.09}$	$0.2^{+0.01}_{-0.01}$	$0.12^{+0.03}_{-0.03}$	$-0.03^{+0.01}_{-0.01}$	$-0.16^{+0.08}_{-0.04}$	$0.52^{+0.04}_{-0.1}$	$-0.08^{+0.18}_{-0.11}$
VUCD3	$0.22^{+0.13}_{-0.16}$	$0.17^{+0.02}_{-0.01}$	$0.14^{+0.05}_{-0.05}$	$-0.06^{+0.02}_{-0.02}$	$-0.09^{+0.19}_{-0.14}$	$0.31^{+0.15}_{-0.26}$	$0.17^{+0.25}_{-0.27}$
VUCD4	$-0.65^{+0.1}_{-0.06}$	$-0.04^{+0.02}_{-0.03}$	$-0.07^{+0.08}_{-0.09}$	$-0.13^{+0.04}_{-0.04}$	$-0.27^{+0.17}_{-0.1}$	$0.1^{+0.2}_{-0.3}$	$-0.04^{+0.28}_{-0.25}$
VUCD7	$-0.59^{+0.08}_{-0.04}$	$-0.03^{+0.01}_{-0.01}$	$0.11^{+0.04}_{-0.04}$	$-0.15^{+0.02}_{-0.02}$	$0.23^{+0.11}_{-0.12}$	$0.25^{+0.13}_{-0.15}$	$0.37^{+0.05}_{-0.13}$
NGC 4874	$-0.03^{+0.19}_{-0.24}$	$0.37^{+0.02}_{-0.02}$	$0.26^{+0.06}_{-0.07}$	$0.08^{+0.04}_{-0.03}$	$-0.05^{+0.2}_{-0.1}$	$0.27^{+0.25}_{-0.32}$	$-0.01^{+0.26}_{-0.12}$
NGC 4889	$0.11^{+0.15}_{-0.19}$	$0.34^{+0.02}_{-0.02}$	$0.38^{+0.05}_{-0.05}$	$-0.03^{+0.03}_{-0.02}$	$-0.1^{+0.14}_{-0.08}$	$0.32^{+0.18}_{-0.28}$	$-0.04^{+0.26}_{-0.14}$

Table 4.4 Table 4.3 continued.

ID	[Mn/Fe]	[N/Fe]	[Na/Fe]	[Ni/Fe]	[O/Fe]	[Sr/Fe]	[V/Fe]
B012	$0.38^{+0.07}_{-0.06}$	$0.89^{+0.14}_{-0.13}$	$0.93^{+0.18}_{-0.19}$	$-0.06^{+0.05}_{-0.03}$	$1.17^{+0.06}_{-0.1}$	$-0.04^{+0.07}_{-0.05}$	$0.01^{+0.09}_{-0.06}$
B058	$0.28^{+0.04}_{-0.04}$,	$0.72^{+0.04}_{-0.04}$,	$0.42^{+0.11}_{-0.1}$,	$-0.08^{+0.04}_{-0.04}$,	$0.85^{+0.02}_{-0.05}$,	$-0.31^{+0.07}_{-0.05}$,	$0.14^{+0.06}_{-0.06}$,
(Original,	$0.2^{+0.04}_{-0.05}$	$0.88^{+0.03}_{-0.05}$	$0.36^{+0.13}_{-0.15}$	$-0.15^{+0.04}_{-0.04}$	$0.86^{+0.03}_{-0.05}$	$-0.31^{+0.07}_{-0.05}$	$-0.15^{+0.06}_{-0.06}$
New)							
B067	$0.36^{+0.04}_{-0.05}$	$0.92^{+0.07}_{-0.07}$	$0.05^{+0.13}_{-0.11}$	$0.03^{+0.05}_{-0.04}$	$1.13^{+0.05}_{-0.1}$	$-0.06^{+0.07}_{-0.04}$	$-0.09^{+0.03}_{-0.03}$
B074	$0.21^{+0.06}_{-0.06}$	$0.1^{+0.1}_{-0.11}$	$0.0^{+0.16}_{-0.14}$	$-0.14^{+0.06}_{-0.05}$	$0.89^{+0.13}_{-0.17}$	$-0.18^{+0.05}_{-0.04}$	$-0.18^{+0.04}_{-0.03}$
B107	$0.06^{+0.05}_{-0.05}$	$0.92^{+0.05}_{-0.06}$	$0.32^{+0.16}_{-0.17}$	$-0.11^{+0.05}_{-0.05}$	$0.82^{+0.04}_{-0.06}$	$-0.22^{+0.1}_{-0.06}$	$-0.07^{+0.07}_{-0.08}$
B163	$0.13^{+0.03}_{-0.03}$	$0.65^{+0.02}_{-0.02}$	$0.24^{+0.06}_{-0.08}$	$0.08^{+0.03}_{-0.03}$	$0.18^{+0.04}_{-0.04}$	$-0.13^{+0.08}_{-0.07}$	$0.02^{+0.04}_{-0.04}$
B193	$0.25^{+0.03}_{-0.03}$	$-0.11^{+0.05}_{-0.05}$	$0.71^{+0.09}_{-0.08}$	$0.04^{+0.03}_{-0.03}$	$0.16^{+0.04}_{-0.05}$	$0.23^{+0.14}_{-0.15}$	$0.07^{+0.05}_{-0.04}$
B225	$0.11^{+0.03}_{-0.03}$	$0.82^{+0.02}_{-0.03}$	$0.15^{+0.1}_{-0.09}$	$0.01^{+0.03}_{-0.04}$	$0.3^{+0.05}_{-0.05}$	$-0.09^{+0.09}_{-0.06}$	$0.01^{+0.04}_{-0.04}$
B338	$-0.07^{+0.05}_{-0.05}$	$0.94^{+0.04}_{-0.05}$	$0.24^{+0.17}_{-0.17}$	$-0.08^{+0.06}_{-0.06}$	$0.86^{+0.06}_{-0.12}$	$-0.25^{+0.08}_{-0.05}$	$-0.21^{+0.06}_{-0.07}$
B405	$0.05^{+0.04}_{-0.04}$	$0.35^{+0.05}_{-0.06}$	$0.05^{+0.16}_{-0.15}$	$-0.21^{+0.04}_{-0.04}$	$0.92^{+0.05}_{-0.09}$	$-0.27^{+0.06}_{-0.03}$	$-0.22^{+0.07}_{-0.05}$
G001	$0.05^{+0.04}_{-0.04}$	$0.92^{+0.03}_{-0.04}$	$0.27^{+0.1}_{-0.1}$	$-0.11^{+0.04}_{-0.04}$	$0.77^{+0.02}_{-0.02}$	$-0.23^{+0.1}_{-0.07}$	$-0.04^{+0.05}_{-0.06}$
M59-	$0.2^{+0.02}_{-0.02}$	$0.11^{+0.02}_{-0.02}$	$-0.04^{+0.07}_{-0.06}$	$0.0^{+0.02}_{-0.02}$	$0.31^{+0.03}_{-0.03}$	$-0.0^{+0.08}_{-0.08}$	$-0.04^{+0.03}_{-0.03}$
UCD3							
VUCD3	$0.09^{+0.05}_{-0.04}$	$0.61^{+0.04}_{-0.04}$	$0.26^{+0.07}_{-0.1}$	$-0.11^{+0.05}_{-0.05}$	$0.55^{+0.02}_{-0.02}$	$0.36^{+0.1}_{-0.12}$	$0.12^{+0.06}_{-0.06}$
VUCD4	$0.36^{+0.03}_{-0.03}$	$0.74^{+0.06}_{-0.08}$	$-0.22^{+0.14}_{-0.13}$	$-0.16^{+0.05}_{-0.05}$	$0.77^{+0.06}_{-0.13}$	$-0.29^{+0.13}_{-0.09}$	$-0.04^{+0.08}_{-0.08}$
VUCD7	$0.24^{+0.03}_{-0.03}$	$0.67^{+0.03}_{-0.02}$	$-0.01^{+0.07}_{-0.08}$	$-0.12^{+0.02}_{-0.02}$	$0.74^{+0.01}_{-0.02}$	$-0.02^{+0.07}_{-0.06}$	$0.05^{+0.04}_{-0.04}$
NGC 4874	$0.13^{+0.05}_{-0.05}$	$0.22^{+0.05}_{-0.06}$	$0.73^{+0.12}_{-0.11}$	$0.13^{+0.06}_{-0.06}$	$0.55^{+0.04}_{-0.06}$	$0.24^{+0.18}_{-0.17}$	$0.27^{+0.06}_{-0.07}$
NGC 4889	$0.05^{+0.04}_{-0.04}$	$0.29^{+0.04}_{-0.03}$	$0.6^{+0.07}_{-0.07}$	$0.0^{+0.04}_{-0.05}$	$0.56^{+0.03}_{-0.03}$	$0.22^{+0.13}_{-0.13}$	$0.13^{+0.05}_{-0.05}$

Since we fit for the two slopes of a 2PL IMF for each object (Equation 3.1), we show each of these slopes in Figure 4.5. In the top panels, we show the low-mass slope (α_1) against our fitted [Fe/H] and σ from the literature. In the bottom panels, we show the same but for (α_2). M31 GCs are shown in purple, UCDs are shown in orange, and BCGs are shown in green. In each panel, the dashed line at 1 represents the respective slope for a Kroupa (2001) IMF. We also show the measurements for ETGs from van Dokkum et al. (2017) as grey circles for comparison. van Dokkum et al. (2017) measure radial gradients, finding that the IMF varies from bottom-heavy in the centres of ETGs to MW-like at the outskirts. Their measurements are spatially resolved, unlike ours, so we distinguish these points by effective radius, to differentiate between the core (filled circles; we take the core to be $\leq 0.1R_e$, which is approximately the aperture for our BCG measurements) and outskirt (open circles) regions. Note also that the van Dokkum et al. (2017) fits include NaD and NaI (in contrast to our measurements), but this does not impact the trends that we discuss. The van Dokkum et al. (2017) data are otherwise identical to ours, in terms of instrumental set-up and spectral fitting. It is difficult to determine a clear picture from our IMF slopes as they are presented here, but we note some objects have both α_1 and α_2 inconsistent with a Kroupa (2001) value (i.e. G001, M59-UCD3, VUCD7, and NGC 4889).

Interesting trends begin to emerge in Figure 4.6, where we examine the IMF mismatch parameter ($\alpha_{\rm IMF}$, Treu et al. 2010). This is the ratio between $(M/L)_*$ where we allow for the IMF to vary to $(M/L)_*$ assuming a Kroupa (2001) IMF. We compare our sample and the van Dokkum et al. (2017) ETGs to the fitted [Fe/H] (left), [Mg/Fe] (middle), and literature σ (right). Figure 4.6 is comparable to Figure (3) in V17.

In general, we confirm the results of V17, where CSSs do not follow the [Fe/H] and [Mg/Fe] trends that have been previously established for ETGs (e.g. Conroy & van Dokkum 2012b; Martín-Navarro et al. 2015; van Dokkum et al. 2017). Regarding the BCGs specifically, while they are both consistent with the main body of ETG results from the literature in general, NGC 4889 is the only object for which we measure a significantly bottom-heavy IMF.

We emphasize that the inclusion or exclusion of the Na features does not affect our overall conclusions. In particular, our conclusions about IMF trends are the same. In Figure B.4 in Appendix B, while there is evidence of bottom-heaviness in more of our higher-metallicity objects, the overall trends do not change. In particular, CSSs still do not follow the same [Fe/H] and [Mg/Fe] trends as ETGs. This is emphasized in Figure 4.7, reproduced from Conroy & van Dokkum (2012b) (the top panel of their Figure 12). This shows tests of the ALF models, where fits including the Na features are compared to fits where various IMF-sensitive features are removed. Qualitatively, the same increasing trend is present in every panel, no matter which set of features is used in the fits. This demon-

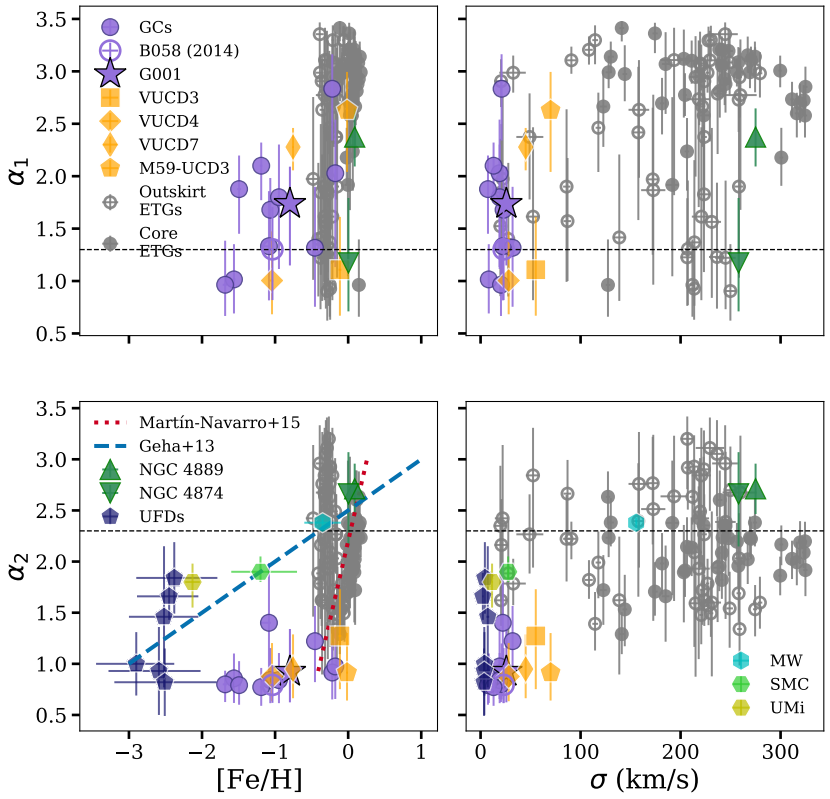

Figure 4.5 Comparison of trends with metallicity and σ from G13 and MN15. G13 examines these trends in ultra-faint dwarf galaxies and MN15 examined massive ETGs. Our fitted low-mass IMF slopes (α_1) are in the top panel, which cannot be directly compared to G13 and MN15 as their mass ranges differ. We compare our intermediate-mass IMF slopes (α_2), which cover similar mass ranges, in the bottom panels. We include individual points from Fig. 15 in G13, including those representing the MW (Bochanski et al. 2010), the SMC (Kalirai et al. 2013), and UMi (Wyse et al. 2002). We also add the UFDs from the extended sample in Gennaro et al. (2018). In the left panels we plot [Fe/H] and on the right we plot σ. In the bottom-left panel, we include the linear fits to metallicity defined in G13 (the Kroupa (2001) empirical relation plus a zero-point shift, dashed blue) and MN15 (dotted pink). In each panel, the horizontal dashed line represents the corresponding slope for a Kroupa (2001) IMF.

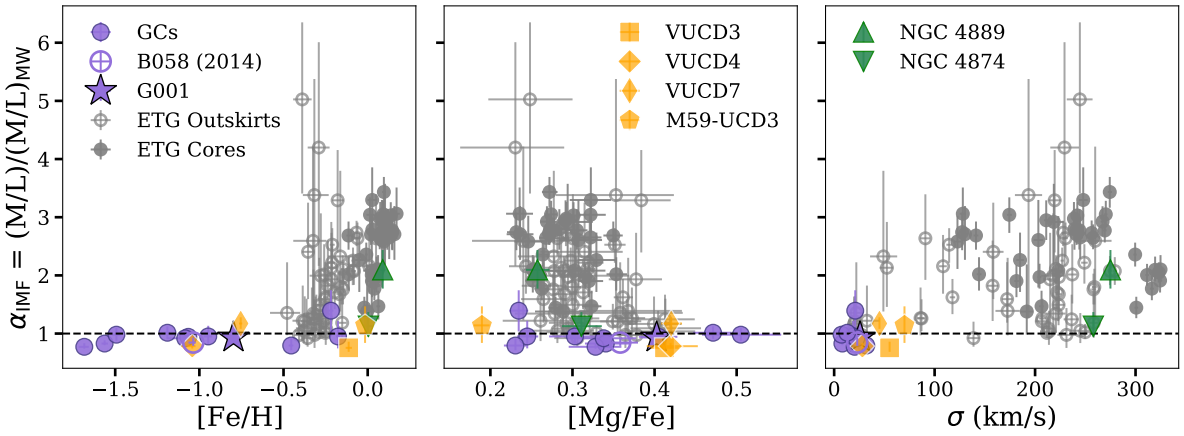

Figure 4.6 The IMF mismatch parameter, $\alpha_{\rm IMF}$ as a function of stellar parameters including [Fe/H] (left-most panel), [Mg/Fe] (second panel), and velocity dispersion (σ, right-most panel). This is similar to Figure 3 in V17. The GCs are shown as purple points. G001 (star) is highlighted to recognize the debate about its characterization in the literature. The newly reduced B058 data from V17 (open symbol) is highlighted to demonstrate the consistency between data taken on different dates and reduced differently. The UCDs are shown in orange and the BCGs are shown in green. We also include the sample of local ETG values from van Dokkum et al. (2017), as in V17, where the filled grey circles indicate "core" measurements (i.e. ≤ 0.1 R_e of the BCGs) and the open circles indicate "outskirt" measurements. The dashed line represents the value of $\alpha_{\rm IMF}$ for a Kroupa (2001) IMF.

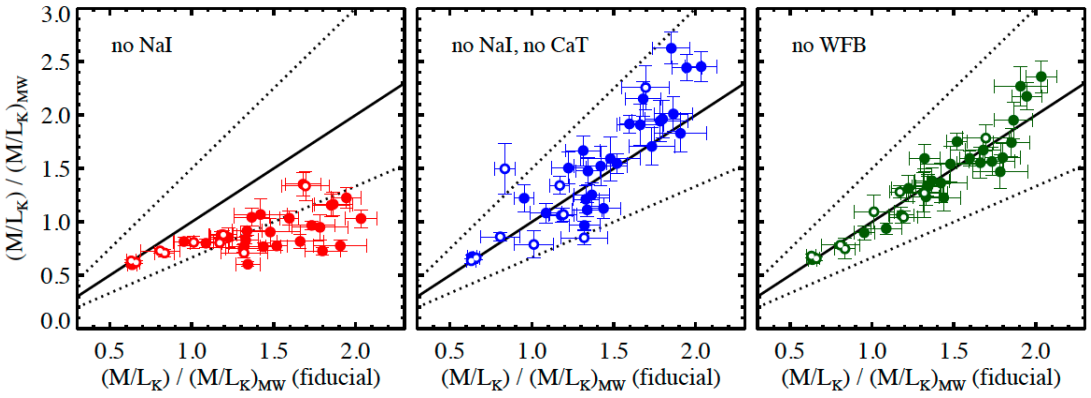

Figure 4.7 $\alpha_{\rm IMF}$ where Na features are included (x-axis) compared to $\alpha_{\rm IMF}$ where various IMF-sensitive features are excluded. In the first panel, NaI is excluded. In the second panel, NaI and CaT are excluded. In the third panel, the Wing-Ford band is excluded. The solid line in each panel is the one-to-one line and the dashed lines indicate slope changes of $\pm$50%. This tests the systematic effects of the derived M/L in ALF.

strates that the basic results are not influenced by any single spectroscopic feature. There are some offsets or slope differences between the different tests, however, in particular when the Na features are removed. This indicates that, in detail, different features favour different M/L. This means that there are still model systematics that need to be understood. For example, these spectral features are all sensitive to different mass ranges, which indicates that a more flexible IMF shape may be necessary to fully explain the data.

There is a caveat to note about our choice to remove NaD and NaI in the main body of this thesis. Specifically, NaI is also IMF-sensitive, and it is crucial to correctly measure all abundances in order to measure the IMF correctly as well (Lonoce et al. 2021). Thus, removing this feature affects our measurement of both the IMF and Na abundances. In particular, it has been found that removing Na systematically reduces the measured bottom-heaviness of the IMF (Newman et al. 2017). We will proceed with our discussion of the fits with the Na features removed with these caveats in mind.

The consistency with a MW IMF for all objects is interesting given the inconsistency that we see for some objects in Figure 4.5. In particular, it is unclear why IMFs that are significantly different from that of Kroupa (2001) in α_1 and α_2 are not reflected in either $\alpha_{\rm IMF}$ in Figure 4.6 or in the well-known IMF-sensitive features shown in the inset panels of Figures 4.3, 4.4, 4.1, and 4.2. Specifically, it is surprising that, despite the fact that NGC 4889 is the only object for which a non-MW IMF is formally preferred in Figure 4.6, this

is not reflected in the inset panels of Figure 4.4. Here we show fits over key IMF-sensitive features, including CaT ($\sim 8484 - 8682$ Å) and the Wing-Ford band ($\sim 9880 - 9970$Å). For each feature, we show a fit allowing for a variable IMF (blue line) and a fit where we fix the IMF to the Kroupa (2001) MW value (red line). We compute the $\chi^2_{\rm min}$ for each fit. Note that we have calculated these $\chi^2_{\rm min}$ outside of the fits for the purposes of these visualizations. Specifically, these are not the same χ^2 values that are used in the MCMC fitting routine described in Chapter 3. Across these features, the variable IMF model and the model where we fix a MW IMF are indistinguishable. Specifically, it is not clear which IMF-sensitive features are driving the variable α_1, α_2, and $\alpha_{\rm IMF}$ in Figures 4.5 and 4.6. More work needs to be done to understand the relationship between α_1, α_2 and $\alpha_{\rm IMF}$ as it is not clear what is driving the variation in α_1 and α_2.

However, if we proceed with the assumption that we are seeing a real effect in our results for the BCGs, for example, this could indicate that the centre of NGC 4874 truly has a MW IMF while NGC 4889 is bottom-heavy. Further study is needed to determine the cause of this difference, but it has been found that the core of the Coma cluster may be a double cluster, with the BCGs originating in separate, presently-distinct clusters (Gu et al. 2018). Thus, perhaps this difference is due to different assembly or merger histories. For example, Nipoti et al. (2020) found that dry mergers tend to make the $\alpha_{\rm IMF}$ profile in an ETG shallower due to mixing with stellar populations with more bottom-light IMFs and the destruction of IMF gradients. Moreover, if confirmed, this could also imply that "discrepant" measurements like those from Newman et al. (2017); Alton et al. (2017, 2018); Feldmeier-Krause et al. (2021); etc., need to be more closely examined. They may not necessarily be easily explained by data systematics only, as previously thought.

We compare some of our fitted stellar parameters to their corresponding literature values in Figure 4.8. Here we fit each GC in our sample twice, once by fitting only the blue wavelength range of the spectrum with ALF's "simple fit" mode, and once by fitting the whole spectrum with the "full fit" mode. We examine the GCs only so that we can compare our results to the wide body of literature ages and abundances, which are not as robust for the UCDs. The simple mode fits for a single age, metallicity, recession velocity, velocity dispersion, and the abundances of C, N, O, Mg, Si, Ca, Ti, and Na, while the full mode fits for all 46 parameters in ALF. We fit the blue sides using the simple mode only because the majority of the other parameters in the full mode are not significantly affected by the blue side and so cannot be reliably fit with such a short wavelength range (we will discuss the significance of these different types of fits further in Section 5.4). We plot the fitted values of age, [Fe/H], [Mg/Fe], [Si/Fe], [Ca/Fe], and [Ti/Fe] for each type of fit against their literature values (listed in Table 4.5).

Our fitted [Fe/H] are largely consistent with literature values. The discrepancies be-

tween our fitted ages and literature values can primarily be attributed to the fact that the Hβ feature, which is a strong indicator of age, is highly degenerate with the blue horizontal branch in GCs (Rich & Origlia 2005; Ocvirk 2010). As such, it is difficult to derive accurate ages from ALF. For the chemical abundances ([Mg/Fe], [Si/Fe], [Ca/Fe], and [Ti/Fe]) inconsistencies could be due to different chemical abundance measurement methods, as the studies from which we obtain the literature values derive abundances using estimations via Lick indices, spectral line synthesis, or full spectrum SPS fitting, for example. Alternatively, as discussed in Section 1, old GCs may have multiple stellar populations, evidenced by anticorrelations in their light elements. As such, abundances can vary greatly on a star-to-star basis (e.g. Carretta et al. 2010), which could be contributing to these differences. Since we are studying the integrated light of these GCs, we are examining the average population abundances, to which ALF is very sensitive. Differences in abundance ratios as a result of these anticorrelations can alter the average abundance ratio significantly.

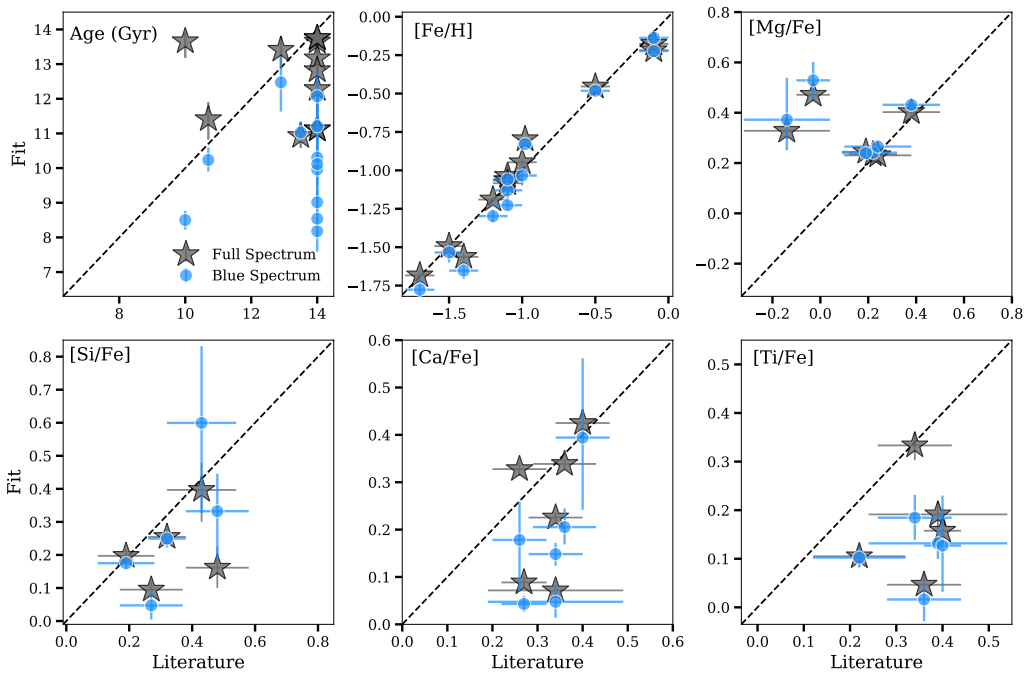

Figure 4.8 A comparison between parameters derived from the full spectrum fits of the integrated light and literature parameters for the GCs (see Table 4.5). We compare fits over the blue wavelength range only (blue points) versus fits over the entire spectrum (grey stars). The consistency that we see between the blue and full wavelength range fits indicates that our sky subtraction and telluric correction are robust.

Table 4.5 Literature parameters for each object in our sample. A dashed entry indicates no literature value available. References: (b) Caldwell et al. (2011); (c) Sakari et al. (2021); (d) Janz et al. (2016); (e) From NED; (f) Paudel et al. (2010); (g) Strader et al. (2011); (h) Janz et al. (2016); (i) Forbes et al. (2014); (j) Veale et al. (2018); (k) Sandoval et al. (2015); (l) Mieske et al. (2013); (m) Greene et al. (2019); (n) Sakari et al. (2016); (o) Colucci et al. (2014); (p) Ahn et al. (2018); (q) Ahn et al. (2017); (r) σ-based mass from Dullo (2019); (s) McConnell et al. (2012).

ID	Age (Gyr)	σ (km/s)	FeH	MgFe	SiFe	CaFe	TiFe	Black Hole
B012-G064	14[b]	20.4[g]	-1.7 ± 0.1[b]	-0.14 ± 0.18[n]	0.43 ± 0.11[n]	0.4 ± 0.06[o]	-	unconfirmed
B058-G119[a]	14[b]	23[g]	-1.1 ± 0.1[b]	-	-	-	-	unconfirmed
B067-G129	14[b]	8.2[g]	-1.4 ± 0.1[b]	-	-	-	-	unconfirmed
B074-G135	14[b]	7.4[g]	-1.5 ± 0.1[b]	-	-	-	-	unconfirmed
B107-G169	14[b]	19.1[g]	-1 ± 0.1[b]	-	-	-	-	unconfirmed
B163[a]	13.5[b]	21[g]	-0.1 ± 0.1[b]	0.22 ± 0.1[n]	0.19 ± 0.09[n]	0.27 ± 0.05[n]	0.22 ± 0.1[n]	unconfirmed
B193[a]	12.9[b]	19[g]	-0.1 ± 0.1[b]	0.19 ± 0.1[n]	0.27 ± 0.1[n]	0.34 ± 0.15[n]	0.36 ± 0.08[n]	unconfirmed
B225-G280	10.7[b]	32[g]	-0.5 ± 0.1[b]	0.24 ± 0.14[n]	0.32 ± 0.06[n]	0.34 ± 0.06[n]	0.39 ± 0.15[n]	unconfirmed
B338-G076	14[b]	22.2[g]	-1.1 ± 0.1[b]	-	-	-	-	unconfirmed
B405-G351	14[b]	13[g]	-1.2 ± 0.1[b]	-0.03 ± 0.07[o]	0.48 ± 0.1[o]	0.26 ± 0.06[o]	0.4 ± 0.04[o]	unconfirmed
G001-MII	10[c]	25.8[g]	-0.98 ± 0.05[c]	0.38 ± 0.12[o]	-	0.36 ± 0.07[c]	0.34 ± 0.08[o]	debated
M59-UCD3[a]	11.7[d]	70[h]	-0.01 ± 0.04[k]	-	-	-	-	$4.2^{+2.1}_{-1.7} \times 10^6$ M$_\odot$[p]
VUCD3	13.754[e]	55.2[i]	-0.011[l]	-	-	-	-	$4.4^{+2.5}_{-3.0} \times 10^6$ M$_\odot$[q]
VUCD4	11.9[f]	28.1[i]	-1.1[l]	-	-	-	-	unconfirmed
VUCD7	10.7[f]	45.1[i]	-0.66[l]	-	-	-	-	unconfirmed
NGC 4874	13.453[e]	258[j]	-0.13 ± 0.06[m]	-	-	-	-	$8.1^{+7.9}_{-7.9} \times 10^8$ M$_\odot$[r]
NGC 4889	13.486[e]	275[j]	0.01 ± 0.02[m]	-	-	-	-	$2.1^{+1.6}_{-1.6} \times 10^{10}$ M$_\odot$[s]

[a] Analyzed in Villaume et al. (2017a).

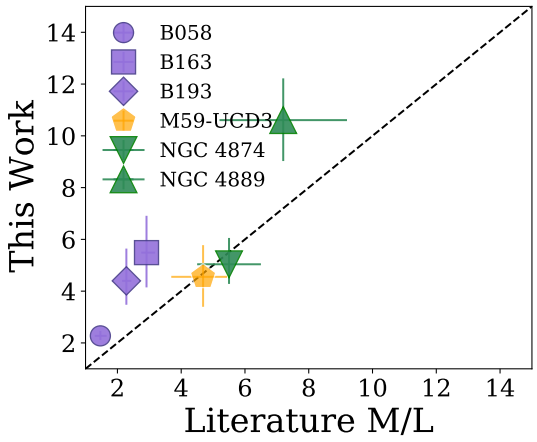

Figure 4.9 Comparison between M/L derived in this study vs. that in V17 and Z17. All studies derive M/L allowing for a variable IMF. The GCs (B058, B163, and B193) are shown as purple points, M59-UCD3 is shown as an orange pentagon, and the BCGs are shown as green triangles. For the V17 points, we compare M/L in the V-band (used throughout this study). To be consistent with Z17, we re-derive our M/L in the r-band for the BCGs and plot them here.

We compare the objects that are common between this study and V17 (i.e. B058, B163, B193, and M59-UCD3), as well as those from Zieleniewski et al. (2017) (NGC 4874 and NGC 4889) in Figure 4.9. For the V17 objects, we show our V-band $(M/L)_*$ from ALF for the data taken in 2014 that we have reduced here on the y-axis (reported in Table 4.1), compared to the results in V17 for the same data on the x-axis. Note that the V17 fits include NaD and NaI. For the BCGs, we re-derive our $(M/L)_*$ in the r-band and compare to those that Z17 compute using SSP models. We emphasize that all $(M/L)_*$ shown in Figure 4.9 allow for a variable IMF. While the GC results between our study and V17 are not entirely consistent, the differences are minor and do not change their overall conclusions. On the other hand, M59-UCD3 is exactly consistent with the value in V17, despite the fact that we measure a significantly different $\alpha_{\rm IMF}$. More work needs to be done to understand the relationship between these quantities. Regarding Zieleniewski et al. (2017) (Z17 hereafter), our $(M/L)_*$ for NGC 4874 appears to be consistent while our $(M/L)_*$ for NGC 4889 does not (although the discrepancy is not significant).

It is unclear what features in the data are driving the fit (specifically the large α_1 for some objects), as it does not seem to be the traditional IMF-sensitive features. More work needs to be done to understand these discrepancies and discern precisely what is driving

any possible IMF variability. Despite this, there are several interesting things we can say about the general trends we see from fitting the full spectra of these objects and allowing stellar population parameters like ages and chemical abundances to vary in addition to the IMF.

Chapter 5

Discussion

5.1 The Relationship between IMF Variations and Metallicity

With our expanded sample, we confirm the general conclusion in V17 that CSSs overall have less variation in $\alpha_{\rm IMF}$ compared to ETGs at similar metallicities. This contributes to the significant scatter in $\alpha_{\rm IMF}$ at the metal-rich end in the left-most panel of Figure 4.6. Furthermore, the $\alpha_{\rm IMF}$ values of CSSs do not vary with metallicity over ~ 1.5 dex in [Fe/H].

We emphasize these results in Figure 4.5, in the context of the commonly-used, metallicity-dependent relationships from Geha et al. (2013) (G13) and Martín-Navarro et al. (2015) (MN15), for low and high metallicities, respectively. Direct comparison of these results is challenging due to the fact that we examine different IMF parameterizations, mass ranges, and measurement methods (i.e. G13 use resolved star counts and MN15 use spectral indices on spatially resolved spectra). We attempt to make indirect comparisons, but these caveats must be kept in mind. We cannot directly compare the low-mass slopes (α_1) in the top panels to G13 and MN15 since they examine higher mass ranges (i.e. G13 examines $0.5 - 0.8$ M$_\odot$ and MN15 examines $\gtrsim 0.6$ M$_\odot$, but our α_1 captures $0.08 - 0.5$ M$_\odot$, see Equation 3.1).

However, we can better compare our intermediate-mass slopes ($\alpha_2, 0.5 - 1.0$ M$_\odot$). In the bottom panels of Figure 4.5, we add the corresponding points from Figure (5) in Gennaro et al. (2018) (an extension of G13, blue pentagons) and points for the MW, Small Magellanic Cloud, and Ursa Minor (hexagons) from Figure (5) in G13. We also plot G13's empirical relationship with [Fe/H] (dashed blue, relationship is from Kroupa (2001) with

a zero-point shift applied to fit their data) and MN15's relationship (dotted pink). This can still give us qualitative insight into how our measured IMF depends on metallicity compared to G13 and MN15. The MN15 relationship qualitatively holds for metal-rich objects only and does not extend down to lower metallicities (this was noted in MN15 as well). The G13 relationship fits the data better, but it does not describe well the scatter introduced by our intermediate-metallicity objects. In particular, while it may not be surprising that the GCs do not lie on this relationship (since they are not galaxies), this is interesting for the galaxy-like UCDs, especially since they are intermediate between the ultra-faint dwarf galaxies studied in G13 and the ETGs studied in M15 and van Dokkum et al. (2017) in [Fe/H] and σ. Thus, we find that more work is needed to fully understand the relationship between metallicity and the IMF.

Our results complicate the picture of a metallicity-dependent IMF that has been found in previous observational studies (e.g. G13, MN15; see also the similar conclusions in V17; La Barbera et al. 2019). We have shown that these may change in complex ways when considering diverse objects and well-populated metallicity ranges. This metallicity-dependence is now being adopted in some models of SF (e.g. Dopcke et al. 2013; Hopkins 2013; Clauwens et al. 2016; Gutcke & Springel 2019; Chon et al. 2021; Prgomet et al. 2021; Sharda & Krumholz 2022). It is beyond the scope of this thesis to directly address these models, but we advise caution when adopting metallicity-dependent IMFs. Other parameters, such as σ or α-element abundances, may also be important (e.g. Treu et al. 2010; Cappellari et al. 2012; Conroy & van Dokkum 2012b; Li et al. 2017; V17; Gennaro et al. 2018; La Barbera et al. 2019; Martín-Navarro et al. 2021, etc.). To interpret our results, we can examine the following question in different ways in Sections 5.2 and 5.3: what is causing the general CSS population to contrast with the ETG population in this parameter space?

5.2 Discrepancies with Dynamical M/L Measurements

Both UCDs and M31 GCs have well-known, distinct, metallicity-dependent discrepancies in their $(M/L)_{dyn}$ behaviour (Mieske et al. 2013; Strader et al. 2011). UCDs have elevated $(M/L)_{dyn}$ compared to SSP expectations. This may be explained by excess dark mass, in the form of a central SMBH, a bottom-heavy IMF, highly concentrated DM, or some combination (Mieske et al. 2013). SMBHs comprising up to $\sim 20\%$ M_* have been detected in 5 UCDs (Seth et al. 2014; Ahn et al. 2017, 2018; Afanasiev et al. 2018), furthermore confirming that at least some fraction are stripped nuclei. Recent studies have additionally extrapolated these results to predict black hole occupancy fractions in UCDs using their

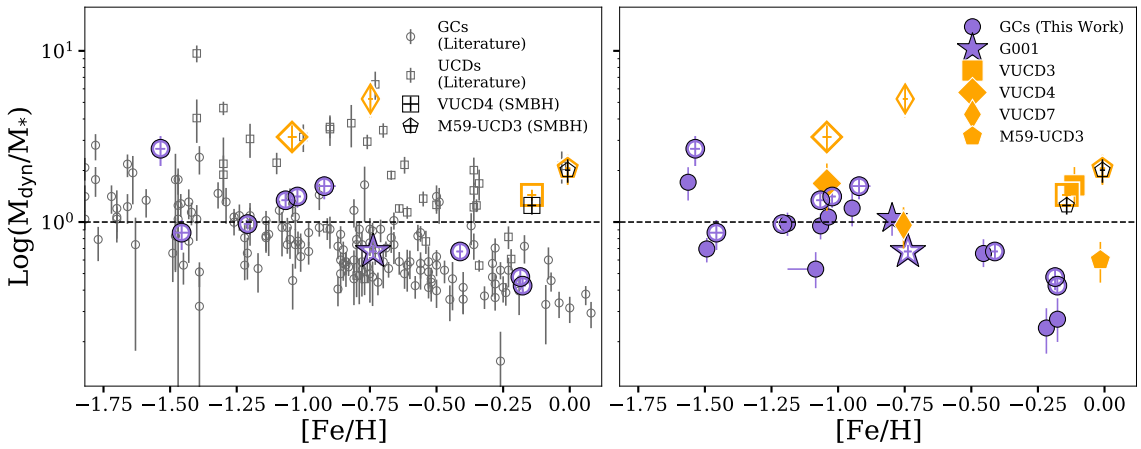

Figure 5.1 Logarithmic M_{dyn}/M_* vs. [Fe/H] for CSSs in our metallicity range. Objects common to this study are highlighted via symbols and colours similar to Figure 4.6, for which we show our fitted [Fe/H] on the x-axis. The dashed line in each panel indicates where $M_{dyn} = M_*$. *Left panel*: Values from the literature which assume a MW IMF. For M59-UCD3, M_{dyn} is from Liu et al. (2015) and M_* is from Sandoval et al. (2015). For the remaining UCDs (open grey squares and open orange symbols), [Fe/H] and M_{dyn} are from Table (3) in Mieske et al. (2013). For the GCs (open grey circles and open purple symbols), [Fe/H] and M_{dyn} are from Strader et al. (2011). For all remaining objects, M_* are from Table (A1) in Norris et al. (2014). We account for SMBH masses for VUCD3 (Ahn et al. 2017) and M59-UCD3 (Ahn et al. 2018) with open black symbols. Note the uncertainties for 3 objects extend beyond the bottom of the plot. *Right panel*: The ratio between $(M/L)_{dyn}$ from the literature (Strader et al. 2011 for GCs, Mieske et al. 2013 for VUCDs, and Ahn et al. 2018 for M59-UCD3) and our fitted $(M/L)_*$ as closed symbols, but this is analogous to M_{dyn}/M_* since $(M/L)_{dyn}$ and $(M/L)_*$ are all in the V-band. We repeat the open symbols from the left panel for the objects in this study, to demonstrate that we lessen the discrepancy between $(M/L)_{dyn}$ and $(M/L)_*$.

$(M/L)_{dyn}$ (e.g. Voggel et al. 2019). However, many UCDs have $M_{dyn}/M_* \gtrsim 2$ (Dabringhausen et al. 2008; Mieske et al. 2008a; Taylor et al. 2010, and see open grey squares in the left panel of Figure 5.1). Moreover, SMBHs emit in the X-ray but the amount of emission detected in massive UCDs is inconsistent with the claim that the majority host SMBHs (Pandya et al. 2016 cf., e.g. Voggel et al. 2019; Dumont et al. 2021). This indicates that SMBHs cannot account for the full excess in all UCDs.

We emphasize this in Figure 5.1, where we compare M_{dyn}/M_* for the two UCDs in our sample with confirmed SMBHs (VUCD3, square and M59-UCD3, pentagon), measured under different considerations: a MW IMF for M_* and not correcting M_{dyn} for the mass of the SMBH (open orange symbols), a MW IMF but accounting for the SMBH mass (open black symbols), and a variable IMF (closed orange symbols, right panel). We obtain the MW IMF and SMBH measurements from various literature sources (see the references in the caption of Figure 5.1), while we fit for the variable IMF measurements. Note that the closed symbols denote the ratio between literature $(M/L)_{dyn}$ and our $(M/L)_*$, but this is analogous to M_{dyn}/M_* since all M/L are in the V-band. The dashed line indicates where $M_{dyn} = M_*$.

To account for SMBH masses, we reduce M_{dyn} by the SMBH mass fraction. Specifically, we subtract the percentage of M_{dyn} made up by the SMBH from the respective UCD's M_{dyn}[1]. Figure 5.1 shows that simply accounting for this mass while fixing a MW IMF does not significantly improve the discrepancy between M_{dyn} and M_*. By allowing the IMF and other stellar population parameters to vary, we find little change for VUCD3, which still has $M_{dyn}/M_* \sim 2$. For M59-UCD3, we find a much lower $M_{dyn}/M_* < 1$. We cannot attribute this fully to variations in the IMF, which is only marginally bottom-heavy relative to the Kroupa (2001) value. However, presumably differences in other parameters are playing a role, since Figure 4.5 shows that M59-UCD3 has an IMF that is very different from that of the MW. We find that VUCD4 and VUCD7, which do not have observed SMBHs, are now fully consistent with $M_{dyn}/M_* \sim 1$. Again, this change cannot be fully attributed to IMF variation, since they have $\alpha_{IMF} \sim 1$. In summary, we find that only VUCD3 shows a modestly large M_{dyn}/M_* after fitting its full spectrum and allowing many stellar population parameters to vary simultaneously. Thus, perhaps an additional source of dark mass (i.e. concentrated dark matter, Haşegan et al. 2005; Goerdt et al. 2008; Baumgardt & Mieske 2008) is required for this object. Further study is required to determine to what extent the combination of the effects of SMBHs, IMF variability, and variation in other stellar population parameters can explain the elevated $(M/L)_{dyn}$ (see, e.g., Mahani et al. 2021),

[1]Note that this is different than the correction done in Ahn et al. (2017) and Ahn et al. (2018). They fit for the SMBH-mass-corrected $(M/L)_{dyn}/(M/L)_*$ and find consistency between dynamics and spectroscopy, but it is not clear how this correction was done.

but this should be considered when searching for SMBHs in UCDs (e.g. Voggel et al. 2019; Dumont et al. 2021).

On the other hand, discrepancies between $(M/L)_*$ with $(M/L)_{dyn}$ in GCs are particularly troubling because they are not expected to contain DM (Grillmair et al. 1995; Odenkirchen et al. 2003; Conroy et al. 2011), so their $(M/L)_*$ and $(M/L)_{dyn}$ should be equivalent. Additionally, Strader et al. (2011) found a trend of decreasing $(M/L)_{dyn}$ with increasing [Fe/H] for M31 GCs, which cannot be explained by SSP models. Since GCs have been expected to be the closest physical representation of SSPs, the M/L differences and this surprising trend could indicate a significant gap in our understanding of GCs or a major shortcoming of SPS models.

We also show the M31 GCs allowing for variation in the IMF and other stellar parameters (solid purple symbols, right panel) and fixing a MW IMF (open purple symbols) in Figure 5.1. As a consequence of our full spectrum fitting, we reduce the discrepancy with $(M/L)_{dyn}$, with only the most metal-poor GC still showing a modest elevation. Our sample is small, but the results are not inconsistent with the trend found in Strader et al. (2011). In particular, we find that the two highest metallicity GCs have very low M_{dyn}/M_*, and these look more discrepant than the ones with low [Fe/H]. Interestingly, these are significantly lower than those found for the two UCDs near this metallicity.

Numerous effects have been suggested to explain this trend for the M31 GCs, including dynamical effects which remove low-mass stars (e.g. a metallicity-dependent spread in mass segregation, Shanahan & Gieles 2015; metallicity- or density-dependent relaxation times, Bianchini et al. 2017; or dynamical evolution, Bianchini et al. 2017; Dalgleish et al. 2020) and differences in GC stellar populations (e.g. the age-metallicity relation, (Haghi et al. 2017); or a metallicity-dependent α-enhancement, Baumgardt et al. 2020).

The uniformity of α_{IMF} over a wide range of metallicities for the M31 GCs suggests that the cause is not some dynamical process that removes low-mass stars in a metallicity-dependent manner as these should be captured by our low-mass IMF measurements[2]. Additionally, our results indicate that systematic differences in important stellar population parameters (e.g. age, α-element abundances) are likely not the cause (since all of our GCs

[2]However, as we note in Section 3, we may not be able to reliably differentiate a bottom-light IMF from a MW IMF. Additionally, for the M31 GCs, we are actually measuring the present-day mass function (PDMF). We assume that the GCs have long relaxation times due to their high masses, so the PDMF should look similar to the IMF (e.g. Equation 17 in Portegies Zwart et al. 2010), however it is possible this is not the case. A metallicity-dependent change in PDMF shape due to dynamical mechanisms could have an effect, but because we use a certain IMF parameterization and do not have the S/N to fit for more flexibility for individual objects, we cannot detect this.

are old and we have shown that α-element abundances are not affecting $(M/L)_*$ in the middle panel of Figure 4.6).

An alternative solution is a metallicity-dependent remnant retention prescription. In particular, ALF currently uses the prescription in Renzini & Ciotti (1993), where the remnant retention fraction is the same for all objects. However, this fraction could vary with physical parameters such as escape velocity or metallicity. Zonoozi et al. (2016) showed that a retention fraction that is linear from 0.4 at [Fe/H] = -2 to 0 at [Fe/H] = 0.5, combined with a variable IMF, could plausibly explain the trend between $(M/L)_{dyn}$ and metallicity in M31 GCs. The Renzini & Ciotti (1993) prescription that ALF uses is standard in SPS models, but there is no metallicity dependence. Thus, updates to the remnant retention prescription may be necessary. Incorporating this is beyond the scope of this paper, but a metallicity-dependence could mitigate some of these discrepancies (e.g. Belczynski et al. 2010; Sippel et al. 2012; Morscher et al. 2015; Zonoozi et al. 2016; see also Mahani et al. 2021).

5.3 Insights into the Formation Pathways of Compact Stellar Systems

As discussed in Section 1, the characterization of UCDs is ambiguous. In the emerging picture, most high-mass UCDs ($M \gtrsim 10^7 M_\odot$) are likely stripped nuclei, containing some dark mass (e.g. dark matter, a central SMBH, or excess low-mass stars) to explain their elevated $(M/L)_{dyn}$. Lower-mass UCDs ($\lesssim 2\times10^6 M_\odot$) are likely comprised of a combination of populations, with some stripped nuclei and some merged or giant star clusters (Norris & Kannappan 2011; Da Rocha et al. 2011; Mieske et al. 2013; Pfeffer et al. 2014, 2016). There are also suggestions that this bimodality extends into galaxy colours and metallicities, with redder UCDs being predominantly stripped nuclei and blue UCDs having mixed origins (Mieske et al. 2006; Brodie et al. 2011; Chilingarian et al. 2011; Voggel et al. 2019). Differentiating the formation pathways of UCDs is therefore challenging.

Several objects in our sample show evidence for being stripped nuclei in the literature. For example, VUCD3 and M59-UCD3 are likely stripped nuclei due to their confirmed SMBHs (Ahn et al. 2017, 2018). G001 is often identified as being part of the M31 GC population, but it is extremely massive, luminous, and contains extreme chemical abundances, potentially indicating that it is a stripped nucleus (Meylan et al. 2001; Nardiello et al. 2019; Sakari et al. 2021). These properties, in conjunction with the debated presence of an intermediate-mass black hole in the centre of G001 (Gebhardt et al. 2002; Baumgardt

et al. 2003; Gebhardt et al. 2005; Pooley & Rappaport 2006; Kong 2007; Ulvestad et al. 2007; Miller-Jones et al. 2012), indicate that its origin is still highly debated.

We do not find any differences in the shape of the IMF between those systems that have been suggested to be stripped nuclei (i.e. VUCD3, M59-UCD3, and G001) and other CSSs. Thus, at the precision of our data, the IMF does not appear to be distinct between objects with proposed different formation pathways.

5.4 Caveats: Systematic Effects and Model Assumptions

Systematics are a major aspect of the debate about the validity of variable IMF measurements, due to discrepancies in SPS studies on an object-by-object basis (e.g. Smith 2014; Lyubenova et al. 2016) and from study-to-study (e.g. our study vs. Z17). In particular, some spectroscopic studies have found individual ETGs that are discrepant with the general picture of increasing bottom-heaviness with σ (e.g. Newman et al. 2017; Alton et al. 2017, 2018), and some have doubted that the IMF is variable at all (e.g. Bastian et al. 2010; Z17, etc.). Thus, it has been difficult to disentangle the physical reality of these outliers from nuisance effects (e.g. data systematics, model parameterization differences).

We have taken care to minimize object-to-object systematics by fitting a range of objects observed with the same instrument set-up and fit with the same spectral fitting procedure, allowing our analysis to be homogeneous. These systematics are the same as those from van Dokkum et al. (2017), so all of the objects plotted in Figure 4.6 are directly comparable.

One potential systematic is that, by nature of using the LRIS instrument, our spectra are divided into blue and red wavelength ranges, each with different instrumental properties (i.e. resolution) as well as physical effects (i.e. sky and telluric absorption lines). It is therefore useful to test whether any of our results are sensitive to one side or the other. We demonstrate this in Figure 4.8. For most of the parameters, the simple, blue side fits are consistent with the full spectrum fits. The exception is for age in the top-left panel. These discrepancies can be explained by the fact that the simple mode only fits for a single-component age, while the full mode fits for a two-component age. The consistency between the two types of fits shows that there are no important systematic differences between the data reduction for the blue and red sides. For example, since sky emission and telluric absorption features are more prominent in the red wavelength regions, if these features were not properly subtracted, we would expect them to confuse the fits and alter the fitted

parameters significantly when including the red side. However, our chemical abundances are largely consistent between the two types of fits, for all GCs studied, indicating that we have mitigated this issue.

However, as we note in Sections 3 and 4, there are still data systematics that are affecting our results. In particular, the lack of variability that we find in the IMF, especially for galaxy-like objects (e.g. the UCDs) is surprising, especially keeping in mind the results of V17. To determine whether the ALF models are performing as expected, we re-create Figure (7) in Conroy & van Dokkum (2012b) (the original is shown in the left panel of Figure 5.2). We show our results in the right panel of Figure 5.2. We refit their data (provided by A. Villaume, private communication), both allowing for a variable IMF and fixing a MW IMF. Note that we compute $\chi^2_{\rm min}$ instead of $\chi^2_{\rm dof}$ from Conroy & van Dokkum (2012b) as it is not clear what they used for their degrees of freedom, as the number of degrees of freedom for such a non-linear model is not well defined (e.g. Andrae et al. 2010; To et al. 2020). We find that, in order to recreate their results, we must remove the jitter parameter introduced in ALF to account for any uncharacterized systematic uncertainties. This parameter was added after Conroy & van Dokkum (2012b) was published. With this modification, our results are relatively consistent, with NGC 4621 strongly preferring a variable IMF over a MW one and NGC 524 being equally well-fit by a variable or MW IMF. However, we note that the MW IMF for NGC 4621 is not as discrepant with the data as it is in Conroy & van Dokkum (2012b), and overall the ALF models (which have been improved upon since Conroy & van Dokkum (2012b) was published) actually fit the data better (compare NGC 524 here with the corresponding panel in Conroy & van Dokkum 2012b). Thus, it is clear that data systematics are playing an important role here (we emphasize this further by including the NaD and NaI features in our fits, in Appendix B).

Specifically, we note that the S/N for the Conroy & van Dokkum (2012b) data is higher on average than our data. In particular, NGC 4621 has an average S/N $\sim$ 343 and NGC 524 has an average S/N $\sim$ 259. These are greater than the S/N for most of our objects, especially over the red wavelength regions where most of the IMF-sensitive features are located. Thus, we conclude that, especially with the modifications made to the ALF models, we do not have sufficient S/N to truly constrain the IMF in our sample. Higher S/N would be preferred in the future, to truly understand the behaviour of the IMF in CSSs.

There also remain study-to-study differences that we do not yet understand fully. For example, we find a discrepancy with V17 for M59-UCD3. We use the exact same data as them, so perhaps there is some key difference in our data reduction procedures or the updates to the ALF models that is impacting our results. In particular, if we are correcting our sky or telluric absorption lines differently, this could be biasing the results. Further investigation is needed.

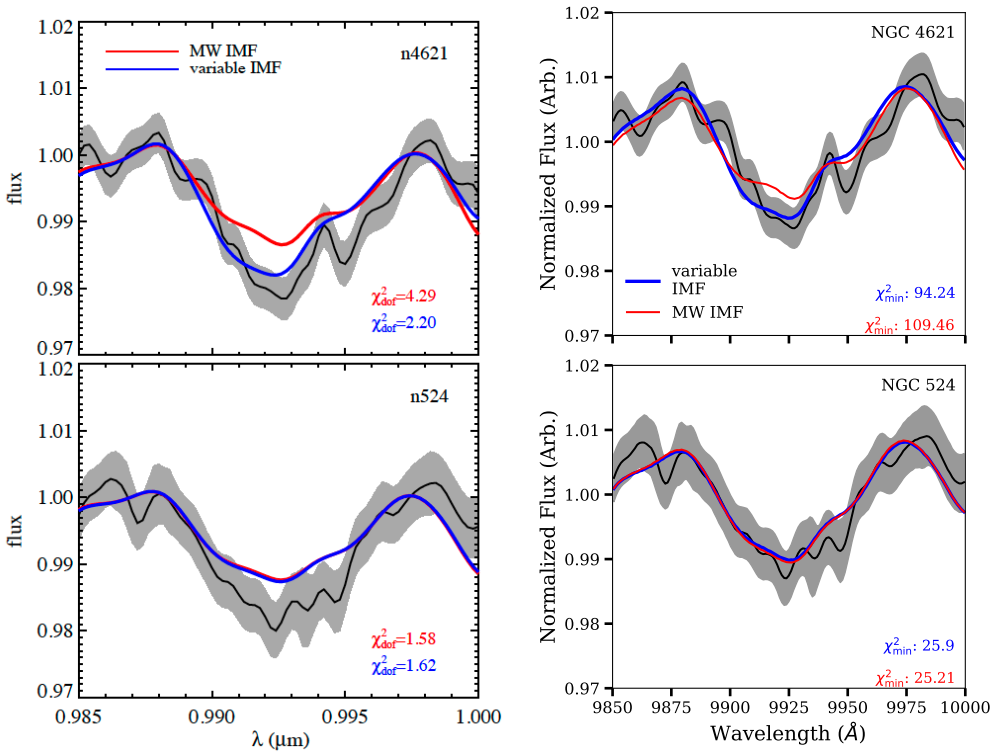

Figure 5.2 Fits for NGC 4621 (top) and NGC 524 (bottom) from Conroy & van Dokkum (2012b). The data are shown in black with the grey bands indicating the spectral uncertainties. A fit where allowing for a variable IMF is shown in blue and a fit where a MW IMF is fixed is shown in red. *Left panels*: Figure (7) reproduced from Conroy & van Dokkum (2012b). *Right panels*: Our reproduction of Figure (7) in Conroy & van Dokkum (2012b), where we re-fit their data with the updated ALF models.

Additionally, Z17 find that NGC 4889 is consistent with a MW IMF, while we find some evidence for bottom-heaviness. A possible physical explanation for the discrepancies between our study and Z17 is the strong degeneracies between spectral features (McConnell et al. 2016; Z17; Lonoce et al. 2021). In particular, IMF-sensitive features are also sensitive to age, metallicity, and many chemical abundances. IMF-driven fluctuations in individual indices are also often too weak to exclude variation in other parameters. Thus, these parameters must be carefully constrained by examining a wide wavelength range and correctly measuring ages, metallicities, and as many chemical abundances as possible (Lonoce et al. 2021). Furthermore, blue and red spectral features can be combined, which has been found to produce a powerful constraint on the low-mass IMF (Conroy & van Dokkum 2012a). However, most studies only use a handful of indices over a limited wavelength range. For example, Z17 analyzed 5 red indices and found unexpected IMFs in the BCGs. On the other hand, Martín-Navarro et al. (2015) also analyzed 5 indices but included blue spectra, and found that the IMF becomes more bottom-heavy with increasing metallicity. To this end, we fit a wider wavelength range of $\sim 4000-10150$ Å, while Z17 only examines features from $\sim 8140-9970$ Å. Our ability to separate these degeneracies is further evident in the middle panel of Figure 4.6, where there is no clear relationship between $\alpha_{\rm IMF}$ and [Mg/Fe]. If we were not sufficiently disentangling the degeneracies, we would expect to see a similar trend as in the [Fe/H] panel. This is because GCs have similar metallicities and element enhancements as ETGs, but should have different IMFs due to their different SF histories. Thus, if the degeneracies were not being properly separated, we would expect to see similarly bottom-heavy $\alpha_{\rm IMF}$ for both types of objects. Before we can conclude degeneracies and the need for a wide wavelength range as explanations, however, we must rule out systematic effects that could be causing these discrepancies.

We find that this discrepancy is likely not due to aperture effects, since our apertures are of a similar size to those in Z17 (i.e. we cover $\sim 0.1R_{\rm e}$ for each BCG and Z17 encompass $0.2R_{\rm e}$, both of which are in the bottom-heavy regime of IMF gradients found in van Dokkum et al. 2017). Moreover, NGC 4874 has a larger $R_{\rm e}$, indicating that we are examining more information from its *core* than the more bottom-heavy NGC 4889 (and would therefore expect NGC 4874 to be more bottom-heavy). Data and instrumental set-up differences could be playing a small role, but on a per-wavelnegth basis, our data have higher S/N. Model systematics could also be playing a small role, since we use a different IMF parameterization than Z17 (2PL, see Section 3, and Z17 use a unimodal parameterization), and it is difficult to account for these differences. However, as we discuss in Section 4, data systematics may be important, since NGC 4889 is bottom-heavy in Figure 4.6 but its IMF-sensitive features are equally well-fit by a variable or MW IMF in Figure 4.4. Thus, NGC 4889's consistency with Z17 is unclear. It is possible that, even if the bottom-heavy IMF

in Figure 4.6 is true, there may be unidentified residuals (for example bad sky subtraction or telluric correction) that are biasing the fits in Figure 4.4.

An additional issue is the discrepancies between $(M/L)_*$ and $(M/L)_{dyn}$ in Figure 5.1. For the closed symbols in the right panel, one GC has $(M/L)_* > (M/L)_{dyn}$ and some GCs have $(M/L)_* < (M/L)_{dyn}$ at the $> 2\sigma$ level. These discrepancies are unlikely to be due to aperture effects. Our GC apertures are slightly smaller than those in Strader et al. (2011) (see Table 2.1), but as a result we would expect $(M/L)_* < (M/L)_{dyn}$ since higher mass stars sink to the centre due to mass segregation (Meylan & Heggie 1997) and giant stars have lower $(M/L)_*$ (e.g. Strader et al. 2011).

A recent burst of SF or excess of AGB/RGB stars could contaminate our IMF measurements, since light dominated by a young population or excess giant stars may be underpredicted in SPS models (Schiavon et al. 2002; Girardi et al. 2010; Strader et al. 2011). However, we have examined the mass fractions of the young components fit in ALF and find that they are negligible, ruling out recent SF. We also examine our fitted [α/Fe] and [α/Ba], which are sensitive probes of SF history (Conroy et al. 2013). We see no strong trends, indicating relatively uniform SF rates and histories.

Since these issues are likely not the result of systematics, our models and expectations may need to be updated. For example, more flexible IMF parameterizations (i.e. flexible m_c or non-parametric shape) may alleviate these tensions (e.g. V17; Conroy et al. 2017; Newman et al. 2017). However, V17 showed that m_c would have to be increased by an extreme (perhaps unrealistic) amount for $(M/L)_*$ and $(M/L)_{dyn}$ to match. Furthermore, a flexible m_c may exacerbate our issue of $(M/L)_* < (M/L)_{dyn}$ for metal-poor GCs as it will systematically lower $(M/L)_*$ across all metallicities. The metallicity-dependent remnant retention fraction discussed above may also be able to mitigate this.

For GCs with $(M/L)_* < (M/L)_{dyn}$, some theoretical studies have proposed that GCs form in DM haloes, breaking from the conventional view of GC formation (e.g. Trenti et al. 2015; Peñarrubia et al. 2017; Wirth et al. 2020; Carlberg & Grillmair 2022; Errani et al. 2022). This could provide an explanation for our GCs with $(M/L)_* < (M/L)_{dyn}$, but further study is needed.

Chapter 6

Future Work

There are several avenues for future study based on this work. There are some discrepancies with the literature (i.e. NGC 4889 in Z17 and M59-UCD3 in V17) that are not understood. In particular, it is not clear from Figure 4.4 which features in the data are driving our determination that $\alpha_{\rm IMF} > 1$ in NGC 4889. Work is ongoing, and some tests are shown in Appendix B.

An immediate follow-up is to increase the S/N. As noted in Section 1, IMF sensitive features vary at a level of 1-3% (Smith 2020). Thus the S/N in our data may not be sufficient to detect these modest differences. Additionally, more work can always be done to improve the ALF models. There are a variety of limitations to the models as they currently stand. For example, ALF makes use of theoretical spectral models, which may be affected by incomplete line lists, adopted microturbulence, assumptions of one-dimensional hydrostatic atmospheres, and local thermodynamic equilibrium. ALF combines these with empirical libraries, but these are not able to uniformly sample all regions of parameter space due to observational limitations (e.g. $T_{\rm eff}$, $\log g$, metallicities, and abundance patterns). They are also often limited by data reduction issues (e.g. flux calibration, telluric correction). Furthermore, the choice of one certain fitting technique over another can impact the precision of the derived parameters. Finally, it can be difficult to understand the integrated effect of all of these limitations on the derived parameters. These are active areas of study and the ALF models will continue to be updated as we improve our understanding of these issues (Conroy & van Dokkum 2012a).

We can also further increase the sample size, to achieve more definitive conclusions on some of the open questions that we raised here. For example, we could add higher S/N data of more UCDs. This would be particularly useful to further fill in the parameter

space that we explore here, since we find that our intermediate-metallicity objects (i.e. the UCDs) introduce scatter into previously established, metallicity-dependent relationships (Section 5.1). By adding more UCDs over a wide metallicity range, the significance of the metal-rich scatter in $\alpha_{\rm IMF}$ at a fixed [Fe/H] would be evident. Including a wider range of masses would furthermore be beneficial to the arguments presented in Section 5.3, and in particular might allow us to more concretely explore the IMF's potential as an indirect probe to identify UCD formation pathways. Additionally, including UCDs from other environments could be interesting, as we only study a handful belonging to the Virgo cluster. For example, it has been suggested that there are key differences in age and DM content between UCDs located in Virgo and those located in Fornax, with Fornax UCDs having M/L lower by 30-40% than Virgo UCDs on average (Mieske et al. 2008b; Chilingarian et al. 2011). Additionally, only one SMBH has been found in a Fornax UCD (Afanasiev et al. 2018), compared to the 4 that have been found in Virgo UCDs (Seth et al. 2014; Ahn et al. 2017, 2018).

A natural starting point is to study the UCD sample presented in Mieske et al. (2013). This is well-placed to begin to address all of these issues, since it includes a wide range of metallicities ($-1.40 \lesssim$ [Fe/H] $\lesssim 0.18$), masses straddling the proposed cutoffs for stripped nuclei and merged star clusters ($\gtrsim 10^7$ M$_\odot$ and $\lesssim 10^6$ M$_\odot$, e.g. Norris & Kannappan 2011; Mieske et al. 2013; Pfeffer et al. 2016), objects located in the Fornax, Virgo, and CenA galaxy clusters, and a total sample size of ~ 50 UCDs (> 10 times as large as our current sample of UCDs). Additionally, Mieske et al. (2013) measured $(\mathrm{M/L})_{\rm dyn}$ for all of these objects, which would allow us to fill in Figure 5.1.

On the other hand, while our conclusions about GCs having bottom-light IMFs across all metallicities seem relatively reliable and consistent with some other measurements (e.g. Hénault-Brunet et al. 2020), expanding our sample of GCs could still prove to be interesting. In particular, this may help to solidify our statement that all GCs have bottom-light IMFs. This could also clarify the discussion around the trend between $(\mathrm{M/L})_{\rm dyn}$ and [Fe/H] in Section 5.2. Examining all of the GCs included in Strader et al. (2011) would be useful in this context, increasing our sample size by a factor of ~ 20. This would also allow us to further extend and fill in the metallicity range (the Strader et al. 2011 GCs encompass $-2.45 \lesssim$ [Fe/H] $\lesssim 0.29$). It would additionally be relatively straightforward to apply the same analysis and assumptions regarding dynamical evolution to these additional GCs since they have similar masses to the sample studied here.

Finally, it would be illustrative to obtain higher S/N data for the BCGs studied here and include the two remaining galaxies studied in Z17 (NGC4839 and NGC4873). This data was not obtained originally due to poor observing conditions, but in principle it would be relatively easy to obtain (for example, an exposure time of $\sim 1-2$ hours in

good observing conditions on the Keck LRIS instrument would be required to achieve the S/N ~ 300/Å for each BCG). This would allow us to determine whether these BCGs truly have IMFs that are consistent with that of the MW, as found in Z17, or whether they are bottom-heavy, in agreement with the literature (e.g. Conroy & van Dokkum 2012b; van Dokkum et al. 2017). We could also use this data to extend the analysis in Section 5.4 and clarify the advantage of full spectrum SPS models over limited-wavelength-range spectral indices and the validity of variable IMF measurements in general.

The main limitation for increasing the sample size to this degree is the S/N we require to make detailed measurements of the IMF. V17 showed that a S/N of $\gtrsim 100$/Å is needed to recover the true $(M/L)_*$ using the ALF models (and in fact we suggest that this is not high enough). In order to achieve the minimum of S/N ~ 100/Å, however, a minimum of ~ 4 nights would be required for the expanded sample of GCs using the Keck LRIS instrument, which could be feasible. However, $\sim 30-35$ nights ($\gtrsim 275$ hours) would be required for the expanded sample of UCDs. This is because even the closest UCDs to us are very faint, necessitating long exposure times of up to 1.5 hours. While it may be possible to obtain such a large program with Keck, the exposure time limitations for this large sample size could be mitigated in the future with new state-of-the-art instruments. For example, the Thirty Metre Telescope (TMT) and the 39-metre European Extremely Large Telescope (E-ELT) will have much larger apertures compared to Keck (10 metres). This can potentially allow for higher S/N observations in a much shorter period of time. Furthermore, their very high spatial resolution may allow us to measure IMF gradients in CSSs, which we can compare to those found in ETGs (i.e. van Dokkum et al. 2017). Finally, they may allow us to perform resolved star counts in more distant stellar systems, potentially allowing us to resolve the distinct but crucial problem of reconciling MW IMF measurements with those in distant galaxies (i.e. Guszejnov et al. 2019).

Looking further afield, we can expand this project to include even more diverse objects and wider parameter spaces by examining stellar systems at higher redshifts (z). In particular, studying the progenitors of present-day stellar systems would allow us to better understand their present-day behaviour, reveal key information about their formation at high-z, and inform models of SF in extreme environments (Smith 2020). High-z analyses would also help us to characterize the proposed cosmic evolution of the IMF (Davé 2008; van Dokkum 2008; Auger et al. 2010; Martín-Navarro 2015). Some exploration of the IMF in high-z systems has been done using dynamical methods (e.g. Cappellari et al. 2006; van de Sande et al. 2015; Price et al. 2016), and it is possible to obtain some ground-based spectroscopic data that are potentially deep and detailed enough to measure the IMF (e.g. Kriek et al. 2015). However, achieving a large enough sample size to complete an analysis like the one done in this paper is extremely difficult using current instrumentation. With

ultra-deep, near-infrared instruments like the James Webb Space Telescope (JWST) set to begin collecting data this summer, we will soon be able to undertake these explorations (e.g. see Newman et al. 2021).

Another follow-up is to update the remnant retention prescriptions for full-spectrum SPS models, which may help to decrease the discrepancies between $(M/L)_{dyn}$ and $(M/L)_*$ that we find in Figure 5.1. In particular, we are interested in examining a metallicity-dependent prescription. These could be added to SPS models like ALF and the data could be re-fit to see if this improves the discrepancies between dynamical and spectroscopic measurements. While it may be difficult to execute this update in the immediate future due to the fact that stellar evolution is currently not well-understood, this would allow us to better characterize the true significance of any difference between the behaviour of metal-rich and metal-poor objects.

We can also fit the spectra with more flexible IMF shapes, as it is not clear that the parameterization we are currently using is something to which the data are sensitive (i.e. it is unclear how α_1 and α_2 relate to α_{IMF}). V17 fit all of their objects using a 2PL IMF shape with a low-mass cutoff (m_c) fixed at 0.08 $M_\odot$ (see Equation 3.1). They were unable to fit for more flexible shapes, for example a 2PL with a variable m_c, or even a non-parametric IMF, due to S/N constraints. However, they pointed out that a higher m_c could bring $(M/L)_*$ into closer agreement with $(M/L)_{dyn}$ from Strader et al. (2011), potentially alleviating the tension between the dynamical and spectroscopic measurements. As we discuss in Section 5.2 and above, this cannot solve the problem completely as flexible IMF shapes will likely act to systematically lower $(M/L)_*$, worsening the discrepancy at the metal-poor end. A more realistic (potentially metallicity-dependent) remnant retention prescription, as discussed above, would first be needed to bring both the low- and high-metallicity ends into agreement. However, once this has been established, a useful test would be to establish if a more flexible IMF improves any remaining discrepancy. We may be able to do this using the spectra presented in this paper, as we have a larger sample size and higher S/N than V17. In particular, we can stack the spectra of similar objects that do not meet the S/N constraints (i.e. metal-poor GCs vs. metal-rich GCs).

More flexible IMF models may also give us more insight into IMF variations in general. Specifically, while a 2PL IMF parameterization is useful in teasing out general IMF variation, if, for example, different IMF-sensitive features are sensitive to a different range of stellar masses, then a more complicated IMF shape may be necessary to properly describe the data (Conroy & van Dokkum 2012b). Some work has been done to place stronger constraints on the shape of the IMF (e.g. Spiniello et al. 2015; Lyubenova et al. 2016), but the ALF models can be used to directly constrain the general form of the IMF from the spectra, as long as the quality of the data is high (Conroy et al. 2017). Addition-

ally, this may lead us closer to resolving the tension between local and extragalactic IMF measurements identified in Guszejnov et al. (2019), as Newman et al. (2017) found that models with more flexibility at the low-mass end were able to alleviate tension in IMF measurements obtained with different methods.

Pursuing a different line of thought, a fascinating area of study is to examine how chemical evolution and IMF variability are related. In particular, IMF variations can have strong implications on chemical evolution, since the IMF determines not only the number of massive stars but also the amount of gas locked in the form of low-mass stars. However, it is not clear precisely how these concepts are related (Martín-Navarro 2015). Since we have fit the objects in this study with ALF, we now have several well-measured chemical abundances for each, including Fe, O, C, N, Na, Mg, Si, K, Ca, Ti, V, Cr, Mn, Co, Ni, Cu, Sr, Ba, and Eu. These could be used to begin to examine this relationship.

A specific direction in this context is to follow-up on Martín-Navarro (2015). As we discussed in Section 1, it is not clear how to reconcile IMF variability with previously established ideas about chemical evolution and SF history. In particular, it has been established that massive ETGs are [Mg/Fe]-enhanced, which could be due to different formation timescales or a variable IMF, where formation timescales have been the preferred explanation due to the perceived universality of the IMF (Worthey et al. 1992). However, influenced by the increasing evidence that the IMF is not universal (e.g. Conroy & van Dokkum 2012b), Martín-Navarro (2015) explored the impact that a variable IMF would have on this explanation. They found that simultaneously considering high [Mg/Fe] and a bottom-heavy IMF implies unphysically short and intense formation events for massive ETGs, and suggested that this may be explained by a non-canonical IMF shape or time-varying IMF. Since we measure both the IMF and [Mg/Fe], it would be interesting to perform a similar analysis with these measurements in hand and for more diverse objects. For example, we could determine the expected formation timescales for CSSs and ETGs and examine how this relates to the conclusions in Martín-Navarro (2015).

Finally, as discussed in Section 5.3, we can measure the detailed SF histories of the UCDs as an additional constraint on whether they have a galactic or star cluster origin. To achieve this, code for measuring detailed SF histories, such as FSPS[1] (Conroy et al. 2009; Conroy & Gunn 2010) combined with PROSPECTOR[2] (Johnson et al. 2021), is necessary. The main limitation with this measurement however is that there are strong degeneracies between ages and metallicities as well as metallicities and dust, especially for old stellar systems (Conroy 2013). As such, broad wavelength coverage is needed, including spectra

[1] https://github.com/cconroy20/fsps .
[2] https://github.com/bd-j/prospector .

in the optical as well as UV and near-infrared photometry.

In conclusion, this is a rich area for future study. With the launch of the next generation of 30-metre telescopes (i.e. E-ELT, TMT), we will be able to efficiently achieve high spatial resolution, high S/N observations of large sample sizes, allowing us to understand the IMF in diverse objects. We will also be able mitigate systematic uncertainties by measuring it via different methods. Furthermore, with imminently-available data from JWST, we will be able to characterize the IMF in more detail, by accessing surface-gravity-sensitive spectral features in the near- and mid-infrared at a much higher S/N than is currently available (i.e. M dwarf-sensitive features such as NaI at 11400 Å and 22100 Å, CaI at 19800 Å, and H_2O lines in the near-infrared; and giant-sensitive features such as CO at 23000 Å; Frogel et al. 1978; Kleinmann & Hall 1986; Ivanov et al. 2004; Rayner et al. 2009). We will also be able to, for the first time, probe the detailed shape of the IMF at high-z. This will advance our understanding of the IMF and stellar populations significantly, fundamentally changing our interpretation of galaxy evolution.

Chapter 7

Summary and Conclusions

The initial mass function is essential to our understanding of star formation and galaxy evolution, but a clear consensus regarding its origin or form has yet to be achieved. One of the major observational limitations is the fact that primarily metal-rich, early-type galaxies have been examined, representing a narrow region of mass-metallicity-density parameter space. To overcome this, we expand the parameter space of variable IMF measurements by examining a diverse sample of extragalactic objects, including compact stellar systems (M31 GCs and Virgo cluster UCDs) and brightest cluster galaxies from the Coma cluster (Figure 2.1). We obtain integrated Keck LRIS spectra for each object and carefully reduce the data using a combination of PypeIt (Prochaska et al. 2020a; Prochaska et al. 2020b) and external routines. As such, we have been able to capture the subtle, $\sim 1-3\%$ (Smith 2020) spectral differences introduced by IMF variations and robustly understand any remaining systematic uncertainties (Figure 2.5). We fit the data using the flexible, full spectrum SPS model alf, which allows for arbitrary variation in the IMF, stellar age, and detailed chemical abundance patterns. We use this to derive 46 stellar parameters, including the two slopes of a 2PL IMF shape (Equation 3.1, Conroy & van Dokkum 2012a; Conroy et al. 2018). Examples of fits are shown in Figures 4.3, 4.4, 4.1, and 4.2 (see also Appendix C).

Our main results are presented in Figure 4.6. We find that overall, all CSSs have IMFs consistent with that of the MW or slightly bottom-light over a wide range of [Fe/H] and [Mg/Fe]. For the BCGs, we find that NGC 4874 has an IMF that is similar to that of the MW, while NGC 4889 has tentative evidence for a bottom-heavy IMF. However, it is unclear which features in the data are driving this result. More work needs to be done to understand this.

We broadly confirm the results of V17, where CSSs do not follow previously-established [Fe/H] and [Mg/Fe] trends (e.g. Conroy & van Dokkum 2012b; Martín-Navarro et al. 2015; van Dokkum et al. 2017). We also confirm the conclusion in V17 that the IMFs of CSSs are less variable compared to ETGs at similar metallicity, contributing to significant scatter in the IMF mismatch parameter at high metallicities. This, combined with the fact that CSSs are ubiquitiously MW-to-bottom light over a wide range of metallicities, indicates that metallicity-dependent trends with IMF variability observed in the literature may not hold equally for different types of stellar systems. In particular, our intermediate-metallicity objects introduce a lot of scatter that is not well-described by the commonly-used G13 or MN15 metallicity-dependent IMF relationships (Figure 4.5). We advise caution when adopting a metallicity-dependent IMF. To interpret our results, we examine the potential cause of the contrast between the general CSS and ETG populations in this parameter space.

Since UCDs and M31 GCs both have unexpected $(M/L)_{dyn}$ behaviour, we first compare our $(M/L)_*$ to $(M/L)_{dyn}$ from the literature (Figure 5.1). We find that fitting the full spectra of these objects and allowing stellar population parameters to vary (including the IMF, ages, and chemical abundances) reduces the trend between $(M/L)_{dyn}$ and metallicity found in Strader et al. (2011), although does not explain it entirely. However, we are able to bring most of the $(M/L)_*$ for the UCDs into agreement with $(M/L)_{dyn}$, with the exception of VUCD3. We suggest that including a metallicity-dependent remnant retention prescription in SPS models may be able to provide some clarity.

We also examine the different UCD formation pathways that have been suggested in the literature and how our results fit into this paradigm. We find that, at the precision of these data, objects with proposed different formation pathways do not appear to have distinct IMFs.

We address a variety of caveats that may be affecting our results. We minimize object-to-object systematics well, but there are a variety of systematics in the data that may be impacting our IMFs. We suggest that higher S/N data is necessary to truly constrain the IMF. Regarding the discrepancies between our results and those of Z17, we find that aperture effects are likely not an explanation, but data systematics and model and instrument set-up differences may be contributing factors. In particular, the question of what is driving the weak IMF variations in Figure 4.6 for NGC 4889 must be solved before definitive conclusions can be made. However, if we assume that our results are true and systematics are not the problem, then the discrepancies may be due to degeneracies between IMF and chemical abundance variations. These are most effectively disentangled by examining many spectral features over a wide wavelength range, which we can achieve with our full spectrum SPS models. If we are seeing a real effect, this could indicate genuine scatter in

the IMFs of the BCGs in our sample at similar metallicites. If this is the case, this may also imply that "discrepant" ETG measurements (e.g. Newman et al. 2017; Alton et al. 2017, 2018; Feldmeier-Krause et al. 2021) may also be genuine and not the result of data systematics only.

For objects in Figure 5.1 that are inconsistent with the expectation that $(M/L)_{dyn}$ is an upper limit for $(M/L)_*$, we find that aperture effects, a recent burst of SF, and excess giant stars likely cannot explain this inconsistency. Fitting our objects with more flexible IMF parameterizations could help, but this would likely worsen the discrepancy at the metal-poor end. For the GCs, the presence of a DM halo has been suggested (i.e. Trenti et al. 2015; Peñarrubia et al. 2017; Wirth et al. 2020; Carlberg & Grillmair 2022; Errani et al. 2022, but further study is required.

An immediate follow-up to this study is to determine what is driving the IMF in Figure 4.6, and this will be done in a forthcoming publication. This study can additionally be expanded upon by improving the ALF models, extending the sample of CSSs, and obtaining higher S/N data, to achieve more definitive conclusions on some of these open questions. In particular, we can include all of the UCDs in Mieske et al. (2013), all of the GCs in Strader et al. (2011), and all of the BCGs in Z17. This may help us to better understand the metallicity-dependence of the IMF and how different UCD formation pathways may manifest in the IMF mismatch parameter. We can also gain more insight by extending our observations to high-z, updating the ALF remnant retention prescription, fitting the spectra with more flexible IMF shapes, examining how chemical evolution and IMF variability are related, and measuring detailed SF histories of the UCDs as an additional constraint on their formation pathways. With the launch of the next generation of 30-metre telescopes (i.e. E-ELT, TMT) and JWST, our understanding of the IMF and stellar populations in extreme environments will change significantly.

In conclusion, with the data that we currently have, we find that CSSs do not follow the same [Fe/H] and [Mg/Fe] trends as massive ETGs. Moreover, this indicates that the form of the metallicity-dependence of the IMF may have to be reconsidered over this expanded parameter space. Several aspects of our study need to be addressed in detail before definitive conclusions can be made, however the lack of IMF variation in CSSs is a potential way forward to better understand GCs and UCDs, and SF more broadly.

References

Abazajian, K. N., Adelman-McCarthy, J. K., Agüeros, M. A., et al. 2009, , 182, 543, doi: 10.1088/0067-0049/182/2/543

Afanasiev, A. V., Chilingarian, I. V., Mieske, S., et al. 2018, , 477, 4856, doi: 10.1093/mnras/sty913

Ahn, C. P., Seth, A. C., den Brok, M., et al. 2017, , 839, 72, doi: 10.3847/1538-4357/aa6972

Ahn, C. P., Seth, A. C., Cappellari, M., et al. 2018, , 858, 102, doi: 10.3847/1538-4357/aabc57

Alton, P. D., Smith, R. J., & Lucey, J. R. 2017, , 468, 1594, doi: 10.1093/mnras/stx464

—. 2018, , 478, 4464, doi: 10.1093/mnras/sty1242

Andersen, M., Gennaro, M., Brandner, W., et al. 2017, , 602, A22, doi: 10.1051/0004-6361/201322863

Andrae, R., Schulze-Hartung, T., & Melchior, P. 2010, arXiv e-prints, arXiv:1012.3754. https://arxiv.org/abs/1012.3754

Auger, M. W., Treu, T., Gavazzi, R., et al. 2010, , 721, L163, doi: 10.1088/2041-8205/721/2/L163

Barber, C., Crain, R. A., & Schaye, J. 2018, Monthly Notices of the Royal Astronomical Society, doi: 10.1093/mnras/sty1826

Barber, C., Schaye, J., & Crain, R. A. 2019a, , 482, 2515, doi: 10.1093/mnras/sty2825

—. 2019b, , 483, 985, doi: 10.1093/mnras/sty3011

Barmby, P. 2010, in From Stars to Galaxies: Connecting our Understanding of Star and Galaxy Formation, 109

Barmby, P., McLaughlin, D. E., Harris, W. E., Harris, G. L. H., & Forbes, D. A. 2007, , 133, 2764, doi: 10.1086/516777

Bastian, N., Covey, K. R., & Meyer, M. R. 2010, , 48, 339, doi: 10.1146/annurev-astro-082708-101642

Bastian, N., & Lardo, C. 2018, Annual Review of Astronomy and Astrophysics, 56, 83–136, doi: 10.1146/annurev-astro-081817-051839

Baumgardt, H., Makino, J., Hut, P., McMillan, S., & Portegies Zwart, S. 2003, , 589, L25, doi: 10.1086/375802

Baumgardt, H., & Mieske, S. 2008, , 391, 942, doi: 10.1111/j.1365-2966.2008.13949.x

Baumgardt, H., Sollima, A., & Hilker, M. 2020, , 37, e046, doi: 10.1017/pasa.2020.38

Bekki, K., Couch, W. J., & Drinkwater, M. J. 2001, , 552, L105, doi: 10.1086/320339

Bekki, K., Couch, W. J., Drinkwater, M. J., & Shioya, Y. 2003, , 344, 399, doi: 10.1046/j.1365-8711.2003.06916.x

Belczynski, K., Bulik, T., Fryer, C. L., et al. 2010, , 714, 1217, doi: 10.1088/0004-637X/714/2/1217

Bianchini, P., Sills, A., van de Ven, G., & Sippel, A. C. 2017, , 469, 4359, doi: 10.1093/mnras/stx1114

Bochanski, J. J., Hawley, S. L., Covey, K. R., et al. 2010, , 139, 2679, doi: 10.1088/0004-6256/139/6/2679

Brodie, J. P., Romanowsky, A. J., Strader, J., & Forbes, D. A. 2011, , 142, 199, doi: 10.1088/0004-6256/142/6/199

Brüns, R. C., & Kroupa, P. 2012, , 547, A65, doi: 10.1051/0004-6361/201219693

Brüns, R. C., Kroupa, P., Fellhauer, M., Metz, M., & Assmann, P. 2011, , 529, A138, doi: 10.1051/0004-6361/201016220

Caldwell, N., Schiavon, R., Morrison, H., Rose, J. A., & Harding, P. 2011, , 141, 61, doi: 10.1088/0004-6256/141/2/61

Cappellari, M., Bacon, R., Bureau, M., et al. 2006, , 366, 1126, doi: 10.1111/j.1365-2966.2005.09981.x

Cappellari, M., McDermid, R. M., Alatalo, K., et al. 2012, Nature, 484, 485–488, doi: 10.1038/nature10972

Cappellari, M., McDermid, R. M., Alatalo, K., et al. 2013, , 432, 1862, doi: 10.1093/mnras/stt644

Carlberg, R. G., & Grillmair, C. J. 2022, arXiv e-prints, arXiv:2203.01365. https://arxiv.org/abs/2203.01365

Carretta, E., Bragaglia, A., Gratton, R. G., et al. 2010, Astronomy and Astrophysics, 516, A55, doi: 10.1051/0004-6361/200913451

Carroll, B. W., & Ostlie, D. A. 2017, An Introduction to Modern Astrophysics, 2nd ed. (United Kingdom: Cambridge University Press)

Carter, D., Visvanathan, N., & Pickles, A. J. 1986, , 311, 637, doi: 10.1086/164804

Cenarro, A. J., Gorgas, J., Vazdekis, A., Cardiel, N., & Peletier, R. F. 2003, , 339, L12, doi: 10.1046/j.1365-8711.2003.06360.x

Chabrier, G. 2003, , 115, 763, doi: 10.1086/376392

Chabrier, G., Hennebelle, P., & Charlot, S. 2014, , 796, 75, doi: 10.1088/0004-637X/796/2/75

Charbonnel, C., Däppen, W., Schaerer, D., et al. 1999, , 135, 405, doi: 10.1051/aas:1999454

Charbonnel, C., Meynet, G., Maeder, A., & Schaerer, D. 1996, , 115, 339

Chilingarian, I. V., Mieske, S., Hilker, M., & Infante, L. 2011, , 412, 1627, doi: 10.1111/j.1365-2966.2010.18000.x

Choi, J., Dotter, A., Conroy, C., et al. 2016, , 823, 102, doi: 10.3847/0004-637X/823/2/102

Chon, S., Omukai, K., & Schneider, R. 2021, , 508, 4175, doi: 10.1093/mnras/stab2497

Clauwens, B., Schaye, J., & Franx, M. 2016, , 462, 2832, doi: 10.1093/mnras/stw1808

Clough, S. A., Shephard, M. W., Mlawer, E. J., et al. 2005, , 91, 233, doi: 10.1016/j.jqsrt.2004.05.058

Cohen, J. G. 1978, , 221, 788, doi: 10.1086/156081

Colucci, J. E., Bernstein, R. A., & Cohen, J. G. 2014, , 797, 116, doi: 10.1088/0004-637X/797/2/116

Conroy, C. 2013, Annual Review of Astronomy and Astrophysics, 51, 393–455, doi: 10.1146/annurev-astro-082812-141017

Conroy, C., & Gunn, J. E. 2010, , 712, 833, doi: 10.1088/0004-637X/712/2/833

Conroy, C., Gunn, J. E., & White, M. 2009, , 699, 486, doi: 10.1088/0004-637X/699/1/486

Conroy, C., Loeb, A., & Spergel, D. N. 2011, , 741, 72, doi: 10.1088/0004-637X/741/2/72

Conroy, C., & van Dokkum, P. 2012a, , 747, 69, doi: 10.1088/0004-637X/747/1/69

Conroy, C., & van Dokkum, P. G. 2012b, The Astrophysical Journal, 760, 71, doi: 10.1088/0004-637x/760/1/71

Conroy, C., van Dokkum, P. G., & Graves, G. J. 2013, , 763, L25, doi: 10.1088/2041-8205/763/2/L25

Conroy, C., van Dokkum, P. G., & Villaume, A. 2017, , 837, 166, doi: 10.3847/1538-4357/aa6190

Conroy, C., Villaume, A., van Dokkum, P. G., & Lind, K. 2018, , 854, 139, doi: 10.3847/1538-4357/aaab49

Conroy, C., White, M., & Gunn, J. E. 2010, , 708, 58, doi: 10.1088/0004-637X/708/1/58

Couture, J., & Hardy, E. 1993, , 406, 142, doi: 10.1086/172426

Da Rio, N., Robberto, M., Hillenbrand, L. A., Henning, T., & Stassun, K. G. 2012, , 748, 14, doi: 10.1088/0004-637X/748/1/14

Da Rocha, C., Mieske, S., Georgiev, I. Y., et al. 2011, , 525, A86, doi: 10.1051/0004-6361/201015353

Dabringhausen, J., Hilker, M., & Kroupa, P. 2008, , 386, 864, doi: 10.1111/j.1365-2966.2008.13065.x

Dabringhausen, J., Kroupa, P., Pflamm-Altenburg, J., & Mieske, S. 2012, , 747, 72, doi: 10.1088/0004-637X/747/1/72

Dalgleish, H., Kamann, S., Usher, C., et al. 2020, , 492, 3859, doi: 10.1093/mnras/staa091

Damian, B., Jose, J., Samal, M. R., et al. 2021, , 504, 2557, doi: 10.1093/mnras/stab194

Davé, R. 2008, , 385, 147, doi: 10.1111/j.1365-2966.2008.12866.x

Dekel, A., Birnboim, Y., Engel, G., et al. 2009, , 457, 451, doi: 10.1038/nature07648

Delisle, S., & Hardy, E. 1992, , 103, 711, doi: 10.1086/116096

Dib, S., Shadmehri, M., Padoan, P., et al. 2010, , 405, 401, doi: 10.1111/j.1365-2966.2010.16451.x

Dopcke, G., Glover, S. C. O., Clark, P. C., & Klessen, R. S. 2013, , 766, 103, doi: 10.1088/0004-637X/766/2/103

Drinkwater, M. J., Gregg, M. D., Hilker, M., et al. 2003, , 423, 519, doi: 10.1038/nature01666

Drinkwater, M. J., Jones, J. B., Gregg, M. D., & Phillipps, S. 2000, , 17, 227, doi: 10.1071/AS00034

Dullo, B. T. 2019, , 886, 80, doi: 10.3847/1538-4357/ab4d4f

Dumont, A., Seth, A. C., Strader, J., et al. 2021, arXiv e-prints, arXiv:2112.04504. https://arxiv.org/abs/2112.04504

Elmegreen, B. G., & Scalo, J. 2004, , 42, 211, doi: 10.1146/annurev.astro.41.011802.094859

Errani, R., Navarro, J. F., Ibata, R., et al. 2022, arXiv e-prints, arXiv:2203.02513. https://arxiv.org/abs/2203.02513

Evstigneeva, E. A., Drinkwater, M. J., Jurek, R., et al. 2007, , 378, 1036, doi: 10.1111/j.1365-2966.2007.11856.x

Faber, S. M., & French, H. B. 1980, , 235, 405, doi: 10.1086/157644

Federici, L., Cacciari, C., Bellazzini, M., et al. 2012, , 544, A155, doi: 10.1051/0004-6361/201219317

Feldmeier-Krause, A., Lonoce, I., & Freedman, W. L. 2021, , 923, 65, doi: 10.3847/1538-4357/ac281e

Fellhauer, M., & Kroupa, P. 2002, , 330, 642, doi: 10.1046/j.1365-8711.2002.05087.x

Ferreras, I., La Barbera, F., de La Rosa, I. G., et al. 2013, , 429, L15, doi: 10.1093/mnrasl/sls014

Forbes, D. A., Norris, M. A., Strader, J., et al. 2014, Monthly Notices of the Royal Astronomical Society, 444, 2993–3003, doi: 10.1093/mnras/stu1631

Foreman-Mackey, D., Hogg, D. W., Lang, D., & Goodman, J. 2013, , 125, 306, doi: 10.1086/670067

Frank, M. J., Hilker, M., Mieske, S., et al. 2011, , 414, L70, doi: 10.1111/j.1745-3933.2011.01058.x

Frogel, J. A., Persson, S. E., Aaronson, M., & Matthews, K. 1978, , 220, 75, doi: 10.1086/155883

Galleti, S., Federici, L., Bellazzini, M., Fusi Pecci, F., & Macrina, S. 2004, , 416, 917, doi: 10.1051/0004-6361:20035632

Gebhardt, K., Rich, R. M., & Ho, L. C. 2002, , 578, L41, doi: 10.1086/342980

—. 2005, , 634, 1093, doi: 10.1086/497023

Geha, M., Brown, T. M., Tumlinson, J., et al. 2013, , 771, 29, doi: 10.1088/0004-637X/771/1/29

Gennaro, M., Tchernyshyov, K., Brown, T. M., et al. 2018, , 855, 20, doi: 10.3847/1538-4357/aaa973

Girardi, L., Williams, B. F., Gilbert, K. M., et al. 2010, , 724, 1030, doi: 10.1088/0004-637X/724/2/1030

Goerdt, T., Moore, B., Kazantzidis, S., et al. 2008, , 385, 2136, doi: 10.1111/j.1365-2966.2008.12982.x

Greene, J. E., Veale, M., Ma, C.-P., et al. 2019, , 874, 66, doi: 10.3847/1538-4357/ab01e3

Grillmair, C. J., Freeman, K. C., Irwin, M., & Quinn, P. J. 1995, , 109, 2553, doi: 10.1086/117470

Gu, M., Conroy, C., Law, D., et al. 2018, arXiv e-prints, arXiv:1810.13242. https://arxiv.org/abs/1810.13242

Gullikson, K., Dodson-Robinson, S., & Kraus, A. 2014, , 148, 53, doi: 10.1088/0004-6256/148/3/53

Guszejnov, D., Hopkins, P. F., & Graus, A. S. 2019, Monthly Notices of the Royal Astronomical Society, 485, 4852–4862, doi: 10.1093/mnras/stz736

Guszejnov, D., Hopkins, P. F., & Ma, X. 2017, , 472, 2107, doi: 10.1093/mnras/stx2067

Gutcke, T. A., & Springel, V. 2019, , 482, 118, doi: 10.1093/mnras/sty2688

Haşegan, M., Jordán, A., Côté, P., et al. 2005, , 627, 203, doi: 10.1086/430342

Haghi, H., Khalaj, P., Hasani Zonoozi, A., & Kroupa, P. 2017, , 839, 60, doi: 10.3847/1538-4357/aa6719

Hallakoun, N., & Maoz, D. 2021, , 507, 398, doi: 10.1093/mnras/stab2145

Hardy, E., & Couture, J. 1988, , 325, L29, doi: 10.1086/185103

Hénault-Brunet, V., Gieles, M., Strader, J., et al. 2020, , 491, 113, doi: 10.1093/mnras/stz2995

Hennebelle, P., & Chabrier, G. 2008, , 684, 395, doi: 10.1086/589916

Hilker, M., Infante, L., Vieira, G., Kissler-Patig, M., & Richtler, T. 1999, , 134, 75, doi: 10.1051/aas:1999434

Holland, S. 1998, The Astronomical Journal, 115, 1916–1920, doi: 10.1086/300348

Hopkins, A. M. 2018, , 35, e039, doi: 10.1017/pasa.2018.29

Hopkins, P. F. 2012, , 423, 2037, doi: 10.1111/j.1365-2966.2012.20731.x

—. 2013, , 433, 170, doi: 10.1093/mnras/stt713

Horne, K. 1986, , 98, 609, doi: 10.1086/131801

Ivanov, V. D., Rieke, M. J., Engelbracht, C. W., et al. 2004, , 151, 387, doi: 10.1086/381752

Janz, J., Forbes, D. A., Norris, M. A., et al. 2015, , 449, 1716, doi: 10.1093/mnras/stv389

Janz, J., Norris, M. A., Forbes, D. A., et al. 2016, , 456, 617, doi: 10.1093/mnras/stv2636

Johnson, B. D., Leja, J., Conroy, C., & Speagle, J. S. 2021, , 254, 22, doi: 10.3847/1538-4365/abef67

Jones, A., Noll, S., Kausch, W., Szyszka, C., & Kimeswenger, S. 2013, , 560, A91, doi: 10.1051/0004-6361/201322433

Kalirai, J. S., Anderson, J., Dotter, A., et al. 2013, , 763, 110, doi: 10.1088/0004-637X/763/2/110

Kelson, D. 2003, Publications of the Astronomical Society of the Pacific, 115, 688–699, doi: 10.1086/375502

Kennicutt, R. C., J. 1983, , 272, 54, doi: 10.1086/161261

Kereš, D., Katz, N., Weinberg, D. H., & Davé, R. 2005, , 363, 2, doi: 10.1111/j.1365-2966.2005.09451.x

Khochfar, S., Emsellem, E., Serra, P., et al. 2011, , 417, 845, doi: 10.1111/j.1365-2966.2011.19486.x

Kim, S., Rey, S.-C., Jerjen, H., et al. 2014, , 215, 22, doi: 10.1088/0067-0049/215/2/22

Kleinmann, S. G., & Hall, D. N. B. 1986, , 62, 501, doi: 10.1086/191149

Kong, A. K. H. 2007, , 661, 875, doi: 10.1086/517880

Kriek, M., Shapley, A. E., Reddy, N. A., et al. 2015, , 218, 15, doi: 10.1088/0067-0049/218/2/15

Kroupa, P. 1998, , 300, 200, doi: 10.1046/j.1365-8711.1998.01892.x

—. 2001, , 322, 231, doi: 10.1046/j.1365-8711.2001.04022.x

Krumholz, M. R. 2014, , 539, 49, doi: 10.1016/j.physrep.2014.02.001

Krumholz, M. R., Klein, R. I., & McKee, C. F. 2011, , 740, 74, doi: 10.1088/0004-637X/740/2/74

Krumholz, M. R., & McKee, C. F. 2020, , 494, 624, doi: 10.1093/mnras/staa659

La Barbera, F., Ferreras, I., Vazdekis, A., et al. 2013, , 433, 3017, doi: 10.1093/mnras/stt943

La Barbera, F., Vazdekis, A., Ferreras, I., et al. 2019, , 489, 4090, doi: 10.1093/mnras/stz2192

Lada, C. J., & Lada, E. A. 2003, , 41, 57, doi: 10.1146/annurev.astro.41.011802.094844

Larson, R. B. 1986, , 218, 409, doi: 10.1093/mnras/218.3.409

—. 2005, , 359, 211, doi: 10.1111/j.1365-2966.2005.08881.x

Li, H., Ge, J., Mao, S., et al. 2017, , 838, 77, doi: 10.3847/1538-4357/aa662a

Liu, C., Peng, E. W., Toloba, E., et al. 2015, , 812, L2, doi: 10.1088/2041-8205/812/1/L2

Lonoce, I., Feldmeier-Krause, A., & Freedman, W. L. 2021, arXiv e-prints, arXiv:2107.02335. https://arxiv.org/abs/2107.02335

Lyubenova, M., Martín-Navarro, I., van de Ven, G., et al. 2016, Monthly Notices of the Royal Astronomical Society, 463, 3220–3225, doi: 10.1093/mnras/stw2434

Mac Low, M.-M., & Klessen, R. S. 2004, Reviews of Modern Physics, 76, 125, doi: 10.1103/RevModPhys.76.125

Mahani, H., Zonoozi, A. H., Haghi, H., et al. 2021, , 502, 5185, doi: 10.1093/mnras/stab330

Mann, A. W., Feiden, G. A., Gaidos, E., Boyajian, T., & von Braun, K. 2015, , 804, 64, doi: 10.1088/0004-637X/804/1/64

Martín-Navarro, I. 2015, Monthly Notices of the Royal Astronomical Society: Letters, 456, L104–L108, doi: 10.1093/mnrasl/slv181

Martín-Navarro, I., Vazdekis, A., Barbera, F. L., et al. 2015. https://arxiv.org/abs/1506.00638

Martín-Navarro, I., Pinna, F., Coccato, L., et al. 2021, Fornax 3D project: assessing the diversity of IMF and stellar population maps within the Fornax Cluster. https://arxiv.org/abs/2107.14243

Mathew, S. S., & Federrath, C. 2021, , doi: 10.1093/mnras/stab2338

Mayes, R. J., Drinkwater, M. J., Pfeffer, J., et al. 2020, Monthly Notices of the Royal Astronomical Society, 501, 1852–1867, doi: 10.1093/mnras/staa3731

McCarthy, J. K., Cohen, J. G., Butcher, B., et al. 1998, in Society of Photo-Optical Instrumentation Engineers (SPIE) Conference Series, Vol. 3355, Optical Astronomical Instrumentation, ed. S. D'Odorico, 81–92, doi: 10.1117/12.316831

McConnell, N. J., Lu, J. R., & Mann, A. W. 2016, , 821, 39, doi: 10.3847/0004-637X/821/1/39

McConnell, N. J., Ma, C.-P., Murphy, J. D., et al. 2012, , 756, 179, doi: 10.1088/0004-637X/756/2/179

McDermid, R. M., Cappellari, M., Alatalo, K., et al. 2014, , 792, L37, doi: 10.1088/2041-8205/792/2/L37

McKee, C. F., & Ostriker, E. C. 2007, , 45, 565, doi: 10.1146/annurev.astro.45.051806.110602

Mei, S., Blakeslee, J. P., Côté, P., et al. 2007, , 655, 144, doi: 10.1086/509598

Meylan, G., & Heggie, D. C. 1997, , 8, 1, doi: 10.1007/s001590050008

Meylan, G., Sarajedini, A., Jablonka, P., et al. 2001, , 122, 830, doi: 10.1086/321166

Mieske, S., Frank, M. J., Baumgardt, H., et al. 2013, , 558, A14, doi: 10.1051/0004-6361/201322167

Mieske, S., Hilker, M., Infante, L., & Jordán, A. 2006, , 131, 2442, doi: 10.1086/500583

Mieske, S., Hilker, M., & Misgeld, I. 2012, , 537, A3, doi: 10.1051/0004-6361/201117634

Mieske, S., & Kroupa, P. 2008, , 677, 276, doi: 10.1086/528739

Mieske, S., Hilker, M., Jordán, A., et al. 2008a, , 487, 921, doi: 10.1051/0004-6361:200810077

—. 2008b, , 487, 921, doi: 10.1051/0004-6361:200810077

Miller, G. E., & Scalo, J. M. 1979, , 41, 513, doi: 10.1086/190629

Miller-Jones, J. C. A., Wrobel, J. M., Sivakoff, G. R., et al. 2012, , 755, L1, doi: 10.1088/2041-8205/755/1/L1

Milone, A. D. C., Sansom, A. E., & Sánchez-Blázquez, P. 2011, , 414, 1227, doi: 10.1111/j.1365-2966.2011.18457.x

Morscher, M., Pattabiraman, B., Rodriguez, C., Rasio, F. A., & Umbreit, S. 2015, , 800, 9, doi: 10.1088/0004-637X/800/1/9

Murray, N. 2009, , 691, 946, doi: 10.1088/0004-637X/691/2/946

Nam, D. G., Federrath, C., & Krumholz, M. R. 2021, , 503, 1138, doi: 10.1093/mnras/stab505

Nardiello, D., Piotto, G., Milone, A. P., et al. 2019, , 485, 3076, doi: 10.1093/mnras/stz629

Newman, A. B., Belli, S., Ellis, R. S., et al. 2021, Resolved Studies of a Unique Lensed Quiescent Galaxy at z=2: Testing Models of Assembly History, Quenching, and IMF Variations, JWST Proposal. Cycle 1, ID. #2345

Newman, A. B., Smith, R. J., Conroy, C., Villaume, A., & van Dokkum, P. 2017, The Astrophysical Journal, 845, 157, doi: 10.3847/1538-4357/aa816d

Nipoti, C., Cannarozzo, C., Calura, F., Sonnenfeld, A., & Treu, T. 2020, , 499, 559, doi: 10.1093/mnras/staa2812

Noll, S., Kausch, W., Barden, M., et al. 2012, , 543, A92, doi: 10.1051/0004-6361/201219040

Norris, M. A., & Kannappan, S. J. 2011, , 414, 739, doi: 10.1111/j.1365-2966.2011.18440.x

Norris, M. A., Kannappan, S. J., Forbes, D. A., et al. 2014, , 443, 1151, doi: 10.1093/mnras/stu1186

Ocvirk, P. 2010, , 709, 88, doi: 10.1088/0004-637X/709/1/88

Odenkirchen, M., Grebel, E. K., Dehnen, W., et al. 2003, , 126, 2385, doi: 10.1086/378601

Offner, S. S. R., Clark, P. C., Hennebelle, P., et al. 2014, in Protostars and Planets VI, ed. H. Beuther, R. S. Klessen, C. P. Dullemond, & T. Henning, 53, doi: 10.2458/azu_uapress_9780816531240-ch003

Oke, J. B., Cohen, J. G., Carr, M., et al. 1995, , 107, 375, doi: 10.1086/133562

Padoan, P., & Nordlund, Å. 2002, , 576, 870, doi: 10.1086/341790

Pandya, V., Mulchaey, J., & Greene, J. E. 2016, The Astrophysical Journal, 819, 162, doi: 10.3847/0004-637x/819/2/162

Paturel, G., & Garnier, R. 1992, , 254, 93

Paudel, S., Lisker, T., & Janz, J. 2010, The Astrophysical Journal, 724, L64–L68, doi: 10.1088/2041-8205/724/1/l64

Peña Ramírez, K., Béjar, V. J. S., Zapatero Osorio, M. R., Petr-Gotzens, M. G., & Martín, E. L. 2012, , 754, 30, doi: 10.1088/0004-637X/754/1/30

Peñarrubia, J., Varri, A. L., Breen, P. G., Ferguson, A. M. N., & Sánchez-Janssen, R. 2017, , 471, L31, doi: 10.1093/mnrasl/slx094

Peacock, M. B., Maccarone, T. J., Knigge, C., et al. 2010, , 402, 803, doi: 10.1111/j.1365-2966.2009.15952.x

Pfeffer, J., Griffen, B. F., Baumgardt, H., & Hilker, M. 2014, , 444, 3670, doi: 10.1093/mnras/stu1705

Pfeffer, J., Hilker, M., Baumgardt, H., & Griffen, B. F. 2016, , 458, 2492, doi: 10.1093/mnras/stw498

Pooley, D., & Rappaport, S. 2006, , 644, L45, doi: 10.1086/505344

Portegies Zwart, S. F., McMillan, S. L. W., & Gieles, M. 2010, , 48, 431, doi: 10.1146/annurev-astro-081309-130834

Posacki, S., Cappellari, M., Treu, T., Pellegrini, S., & Ciotti, L. 2015, , 446, 493, doi: 10.1093/mnras/stu2098

Prantzos, N., & Charbonnel, C. 2006, Astronomy Astrophysics, 458, 135–149, doi: 10.1051/0004-6361:20065374

Prgomet, M., Rey, M. P., Andersson, E. P., et al. 2021, EDGE: The sensitivity of ultra-faint dwarfs to a metallicity-dependent initial mass function. https://arxiv.org/abs/2107.00663

Price, S. H., Kriek, M., Shapley, A. E., et al. 2016, , 819, 80, doi: 10.3847/0004-637X/819/1/80

Prochaska, J. X., Hennawi, J. F., Westfall, K. B., et al. 2020a, Journal of Open Source Software, 5, 2308, doi: 10.21105/joss.02308

Prochaska, J. X., Hennawi, J., Cooke, R., et al. 2020b, pypeit/PypeIt: Release 1.0.0, v1.0.0, Zenodo, doi: 10.5281/zenodo.3743493

Rayner, J. T., Cushing, M. C., & Vacca, W. D. 2009, , 185, 289, doi: 10.1088/0067-0049/185/2/289

Renzini, A., & Ciotti, L. 1993, , 416, L49, doi: 10.1086/187068

Rich, R. M., & Origlia, L. 2005, , 634, 1293, doi: 10.1086/432592

Rockosi, C., Stover, R., Kibrick, R., et al. 2010, in Society of Photo-Optical Instrumentation Engineers (SPIE) Conference Series, Vol. 7735, Ground-based and Airborne Instrumentation for Astronomy III, ed. I. S. McLean, S. K. Ramsay, & H. Takami, 77350R, doi: 10.1117/12.856818

Russell, H. N. 1934, , 79, 317, doi: 10.1086/143539

Sagar, R., Munari, U., & de Boer, K. S. 2001, , 327, 23, doi: 10.1046/j.1365-8711.2001.04438.x

Sakari, C. M., Shetrone, M. D., McWilliam, A., & Wallerstein, G. 2021, , 502, 5745, doi: 10.1093/mnras/stab141

Sakari, C. M., Shetrone, M. D., Schiavon, R. P., et al. 2016, , 829, 116, doi: 10.3847/0004-637X/829/2/116

Salpeter, E. E. 1955, , 121, 161, doi: 10.1086/145971

Sánchez-Blázquez, P., Peletier, R. F., Jiménez-Vicente, J., et al. 2006, , 371, 703, doi: 10.1111/j.1365-2966.2006.10699.x

Sánchez-Janssen, R., Côté, P., Ferrarese, L., et al. 2019, , 878, 18, doi: 10.3847/1538-4357/aaf4fd

Sandoval, M. A., Vo, R. P., Romanowsky, A. J., et al. 2015, The Astrophysical Journal, 808, L32, doi: 10.1088/2041-8205/808/1/l32

Scalo, J. M. 1986, , 11, 1

Schaller, G., Schaerer, D., Meynet, G., & Maeder, A. 1992, , 96, 269

Schiavon, R. P., Faber, S. M., Rose, J. A., & Castilho, B. V. 2002, , 580, 873, doi: 10.1086/343789

Schwarzschild, M., & Spitzer, L. 1953, The Observatory, 73, 77

Seth, A. C., van den Bosch, R., Mieske, S., et al. 2014, , 513, 398, doi: 10.1038/nature13762

Shanahan, R. L., & Gieles, M. 2015, , 448, L94, doi: 10.1093/mnrasl/slu205

Sharda, P., & Krumholz, M. R. 2022, , 509, 1959, doi: 10.1093/mnras/stab2921

Sippel, A. C., Hurley, J. R., Madrid, J. P., & Harris, W. E. 2012, , 427, 167, doi: 10.1111/j.1365-2966.2012.21969.x

Smith, R. J. 2014, Monthly Notices of the Royal Astronomical Society: Letters, 443, L69–L73, doi: 10.1093/mnrasl/slu082

Smith, R. J. 2020, , 58, 577, doi: 10.1146/annurev-astro-032620-020217

Sparke, Linda, S., & Gallagher, John, S. I. 2007, Galaxies in the Universe: An Introduction, 2nd ed. (New York: Cambridge University Press)

Spiniello, C., Trager, S., Koopmans, L. V. E., & Conroy, C. 2014, , 438, 1483, doi: 10.1093/mnras/stt2282

Spiniello, C., Trager, S. C., & Koopmans, L. V. E. 2015, , 803, 87, doi: 10.1088/0004-637X/803/2/87

Spiniello, C., Trager, S. C., Koopmans, L. V. E., & Chen, Y. P. 2012, , 753, L32, doi: 10.1088/2041-8205/753/2/L32

Spinrad, H., & Taylor, B. J. 1971, , 22, 445, doi: 10.1086/190232

Strader, J., Caldwell, N., & Seth, A. C. 2011, , 142, 8, doi: 10.1088/0004-6256/142/1/8

Strader, J., Seth, A. C., Forbes, D. A., et al. 2013, , 775, L6, doi: 10.1088/2041-8205/775/1/L6

Suárez, G., Downes, J. J., Román-Zúñiga, C., et al. 2019, , 486, 1718, doi: 10.1093/mnras/stz756

Taylor, M. A., Puzia, T. H., Harris, G. L., et al. 2010, , 712, 1191, doi: 10.1088/0004-637X/712/2/1191

Tinsley, B. M. 1980, , 5, 287

To, C.-H., Reddick, R. M., Rozo, E., Rykoff, E., & Wechsler, R. H. 2020, , 897, 15, doi: 10.3847/1538-4357/ab9636

Trenti, M., Padoan, P., & Jimenez, R. 2015, , 808, L35, doi: 10.1088/2041-8205/808/2/L35

Treu, T., Auger, M. W., Koopmans, L. V. E., et al. 2010, , 709, 1195, doi: 10.1088/0004-637X/709/2/1195

Tsuji, T. 1973, , 23, 411

Tully, R. B., Courtois, H. M., & Sorce, J. G. 2016, , 152, 50, doi: 10.3847/0004-6256/152/2/50

Ulvestad, J. S., Greene, J. E., & Ho, L. C. 2007, , 661, L151, doi: 10.1086/518784

van de Sande, J., Kriek, M., Franx, M., Bezanson, R., & van Dokkum, P. G. 2015, , 799, 125, doi: 10.1088/0004-637X/799/2/125

van Dokkum, P., Conroy, C., Villaume, A., Brodie, J., & Romanowsky, A. J. 2017, The Astrophysical Journal, 841, 68, doi: 10.3847/1538-4357/aa7135

van Dokkum, P. G. 2008, , 674, 29, doi: 10.1086/525014

van Dokkum, P. G., & Conroy, C. 2012, The Astrophysical Journal, 760, 70, doi: 10.1088/0004-637x/760/1/70

Veale, M., Ma, C.-P., Greene, J. E., et al. 2018, , 473, 5446, doi: 10.1093/mnras/stx2717

Villaume, A., Brodie, J., Conroy, C., Romanowsky, A. J., & van Dokkum, P. 2017a, , 850, L14, doi: 10.3847/2041-8213/aa970f

Villaume, A., Conroy, C., Johnson, B., et al. 2017b, , 230, 23, doi: 10.3847/1538-4365/aa72ed

Voggel, K. T., Seth, A. C., Baumgardt, H., et al. 2019, , 871, 159, doi: 10.3847/1538-4357/aaf735

Ward, J. L., Kruijssen, J. M. D., & Rix, H.-W. 2020, , 495, 663, doi: 10.1093/mnras/staa1056

Wing, R. F., & Ford, W. Kent, J. 1969, , 81, 527, doi: 10.1086/128814

Wirth, H., Bekki, K., & Hayashi, K. 2020, , 496, L70, doi: 10.1093/mnrasl/slaa089

Worthey, G. 1994, , 95, 107, doi: 10.1086/192096

Worthey, G., Faber, S. M., & Gonzalez, J. J. 1992, , 398, 69, doi: 10.1086/171836

Wyse, R. F. G., Gilmore, G., Houdashelt, M. L., et al. 2002, , 7, 395, doi: 10.1016/S1384-1076(02)00156-2

Zieleniewski, S., Houghton, R. C. W., Thatte, N., Davies, R. L., & Vaughan, S. P. 2017, , 465, 192, doi: 10.1093/mnras/stw2712

Zonoozi, A. H., Haghi, H., & Kroupa, P. 2016, The Astrophysical Journal, 826, 89, doi: 10.3847/0004-637x/826/1/89

APPENDICES

Appendix A

Flexure Correction Methodology

Here we describe our blue-side flexure correction in detail. As discussed in Section 2.3.2, we create a template spectrum of the data with literature age and metallicity, using the `write_a_model` SSP framework in ALF. Letting λ_t be the template wavelength and λ_o be the observed wavelength of the data, we see that the observed wavelength will be equal to the redshifted template wavelength, plus some wavelength-dependent function of flexure, $\delta(\lambda)$:

$$\lambda_o = \lambda_t(1+z) + \delta(\lambda). \tag{A.1}$$

Here, we assume $\delta(\lambda)$ is a linear function of the redshifted template wavelength:

$$\delta(\lambda) = b\lambda_t(1+z) + a \tag{A.2}$$

Thus, our goal is to recover $\delta(\lambda)$ by disentangling both z and $\delta(\lambda)$ from λ_o, by completing the following:

1. Divide the data into regions of $\sim$ 250 Å (similar to van Dokkum & Conroy 2012) and continuum-normalize the observed regions.
2. Divide the template into similar regions, by taking the central wavelength, λ_c, in each of the bins in step 1 and using this to define regions of the same length, plus an overhang of $\sim$ 20 Å on either side to account for wavelength shift from redshift and spectral flexure. Continuum-normalize the template regions.
3. Compare the corresponding observed and template regions and measure the redshift of each region using a routine based on the ASTROPY SPECUTILS `template_redshift`[1]

[1] https://specutils.readthedocs.io/en/stable/api/specutils.analysis.template_redshift.html .

function. This measured redshift will be different from the assumed literature redshift as a result of the spectral flexure.

4. Multiply the measured redshift in each chunk by the de-redshifted λ_c (where we assume that the literature value of z in SIMBAD is correct), such that the measured redshifts are in the rest-frame. Fit a straight line to these measured redshifts:

$$\lambda_{\text{error}} = c\lambda_c + d \tag{A.3}$$

5. Use Equation A.3 to solve for the coefficients a and b in Equation A.2. We start from an expression for the difference between the observed and template wavelength,as

$$\lambda_o - \lambda_t = \Delta\lambda = \lambda_t[(1+z)(1+b) - 1] + a. \tag{A.4}$$

This is equivalent to λ_{error} in Equation A.3, with $c = (1+z)(1+b) - 1$ and $d = a$. Thus

$$a = d \qquad b = \frac{c - z}{1 + z}. \tag{A.5}$$

6. Create a "correction factor", which represents the flexure $\delta(\lambda)$, by rewriting Equation A.2 in terms of λ_o:

$$\delta(\lambda) = \frac{b\lambda_0 + a}{1 + b} \tag{A.6}$$

with a and b given by Equation A.5. We subtract this from the wavelength array to produce a final, flexure-corrected wavelength solution.

Appendix B

Additional Systematics Tests

B.1 The Impact of Specific Lines

In Section 3, due to the large residuals near the NaD and NaI features in Figure 3.2, we removed them from the remainder of our analysis. We have also fit all objects with NaD and NaI included, and we present the results here.

We demonstrate our fits to the BCGs in Figure B.1 for NGC 4874 and Figure B.2 for NGC 4889, analogous to Figures 4.3 and 4.4 in Section 3. We also show our fit to G001 in Figure B.3, analogous to Figure 4.1.

We also show our results in Figure B.4, analogous to Figure 4.6 in Section 4. Here, we more strongly confirm the results of V17. With the exception of B107 and G001, GCs have IMFs consistent with that of the MW or slightly bottom-light over a large range of [Fe/H] and [Mg/Fe]. UCDs are generally more bottom-heavy, with the exception of M59-UCD3 and VUCD4. Regarding the BCGs, while they are both consistent with the main body of ETG results from the literature in general, NGC 4874 is much less bottom-heavy and more similar to a MW IMF (similar to the result found in Zieleniewski et al. 2017), while NGC 4889 is very bottom-heavy (inconsistent with Zieleniewski et al. 2017).

Despite the strong evidence that we see for IMF variability in Figure 4.6, in particular bottom-heavy IMFs for NGC 4889, G001, B107, VUCD3, and VUCD7, this is not strongly reflected in the inset panels of, for example, Figure B.2, similar to what we found for NGC 4889 in the main body of the paper. Here we show fits for these objects over key IMF-sensitive features, including NaI (~ 8200 Å), CaT ($\sim 8484 - 8682$ Å), and the Wing-Ford band ($\sim 9880 - 9970$Å). For each feature, we show a fit allowing for a variable IMF (blue

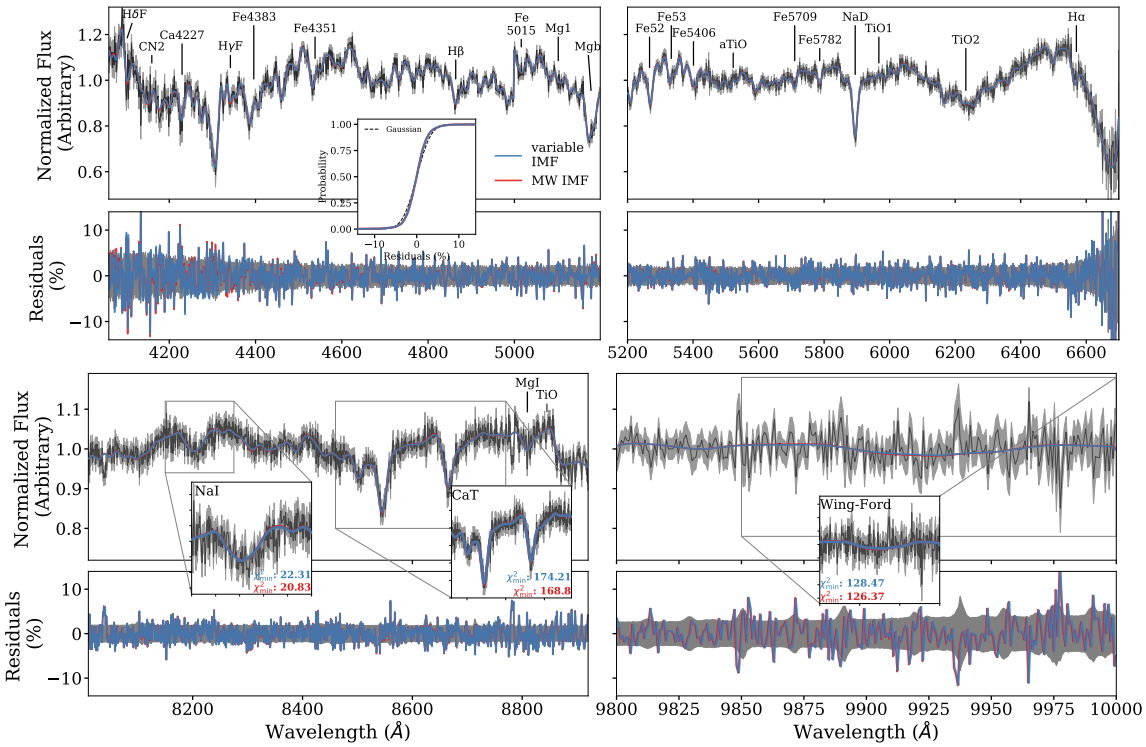

Figure B.1 The same as Figure 4.3 for NGC 4874, but with the NaD and NaI features included.

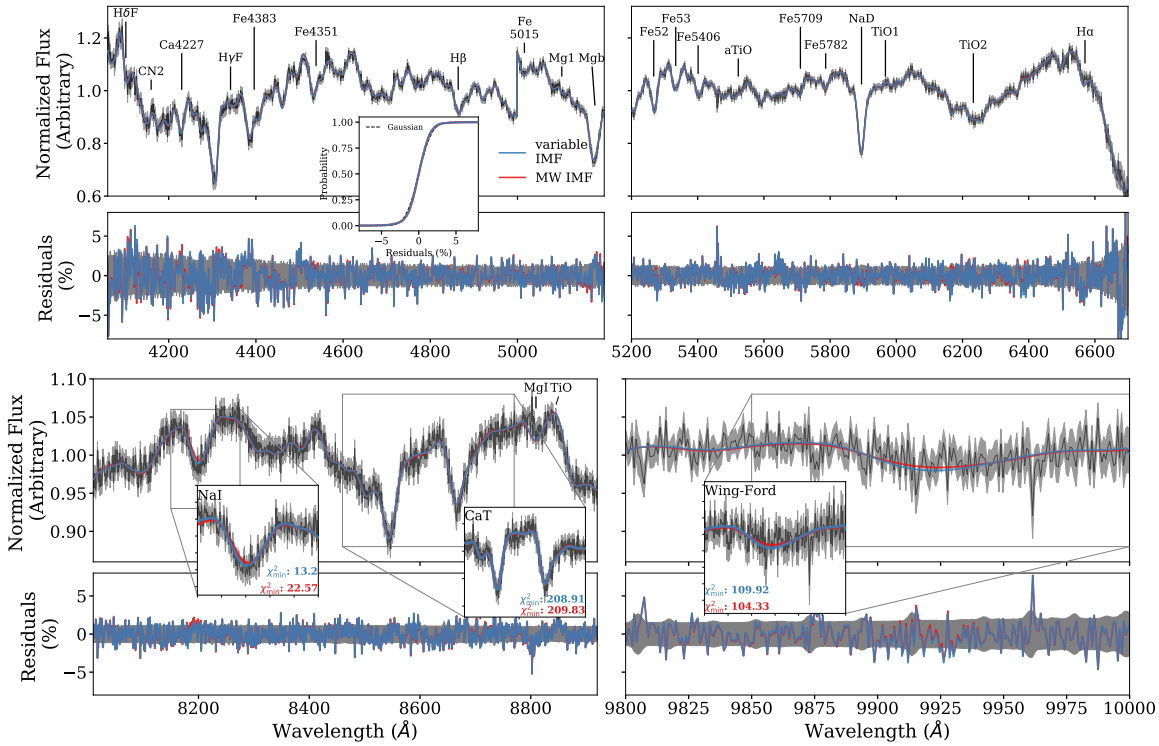

Figure B.2 The same as Figure B.1, but for NGC 4889.

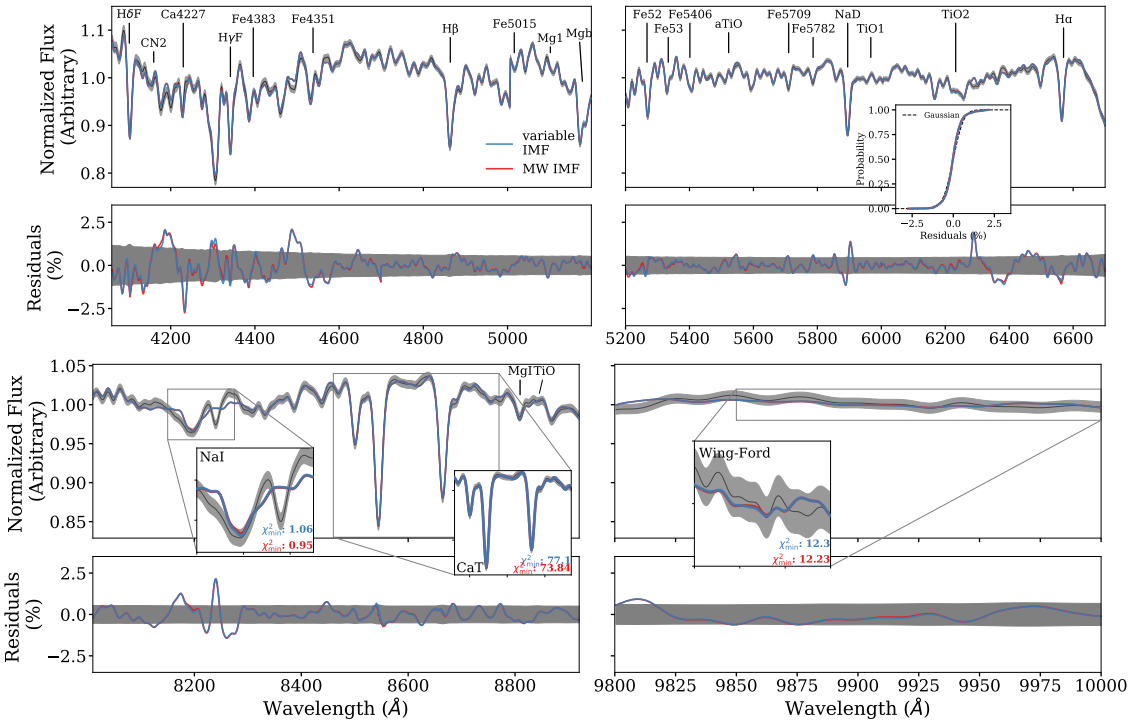

Figure B.3 The same as Figure B.1, but for G001.

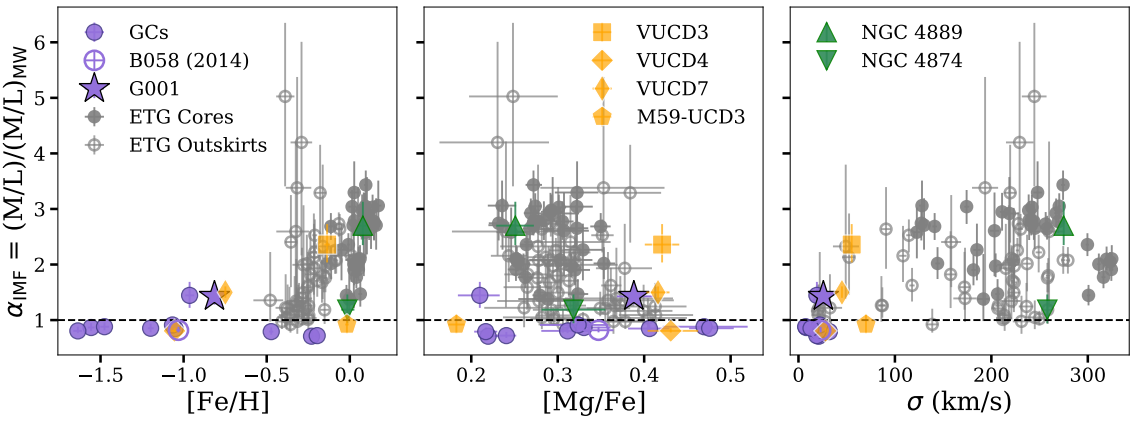

Figure B.4 The same as Figure 4.6, but with the NaD and NaI features included in the fits.

line) and a fit where we fix the IMF to the Kroupa (2001) MW value (red line). We compute the $\chi^2_{\rm min}$ for each fit. In particular, across features like CaT and the Wing-Ford band, there is no significant difference between the variable IMF model and the model where we fix a MW IMF. There is a difference between the models over the NaI feature in all of the objects with supposedly bottom-heavy IMFs, which could potentially indicate that NaI may be driving the bottom-heaviness. However, this seems unlikely since we find that the residuals for NaI are quite large and it is strange that the Wing-Ford band, which is particularly sensitive to M dwarfs (Wing & Ford 1969) does not require a variable IMF for any of these objects. It is unclear why we do not see the expected variation between the different models in Figure B.2. Thus, we are unable to make any robust claims against the IMFs in these objects being consistent with a MW IMF.

B.2 The Effect of Smoothing

We perform several tests to determine the cause of the discrepancies that we are seeing between the IMF mismatch parameters in Figure 4.6 and the fits over the IMF-sensitive features, particularly for G001 in Figure B.3. We use G001 as a test case because it is the object for which our S/N is highest, its formation pathway is debated (see Section 5.3), and it is distinctly bottom-heavy in Figure B.4, compared to the rest of the GCs.

As discussed in Section 3, we must smooth the CSSs prior to fitting, since their intrinsic resolution is higher than that of the ALF models. However, smoothing must be done carefully - it is important to mask out artifacts so that they do not become broadened into adjacent spectral regions, but it can be challenging to differentiate between artifacts and true spectral features. Thus, as a proof of concept, we test fitting the unsmoothed data. We show the fits, with and without the NaD and NaI features in Figures B.5 and B.6, respectively. Here, a variable IMF is strongly preferred by the $\chi^2_{\rm min}$ values when the Na features are retained but the MW fit is preferred when the Na features are masked. We also fit only the red unsmoothed data, with and without the NaD and NaI features, in Figures B.7 and B.8. A variable IMF is preferred in both cases.

Since it is clear that smoothing can have a significant impact on the results, we also test different smoothing routines, in addition to the one that is currently presented in the paper (where we smooth by 200 km/s). First, we test smoothing to 100 km/s, which is the minimum smoothing that can be applied due to the resolution of the ALF models. This can only be done on the red side since the resolution on the blue side is $>$ 100 km/s. Smoothing to a resolution requires one extra step compared to smoothing by a resolution, which we described in Chapter 3. In particular, instead of feeding the PROSPECTOR `smoothspec`

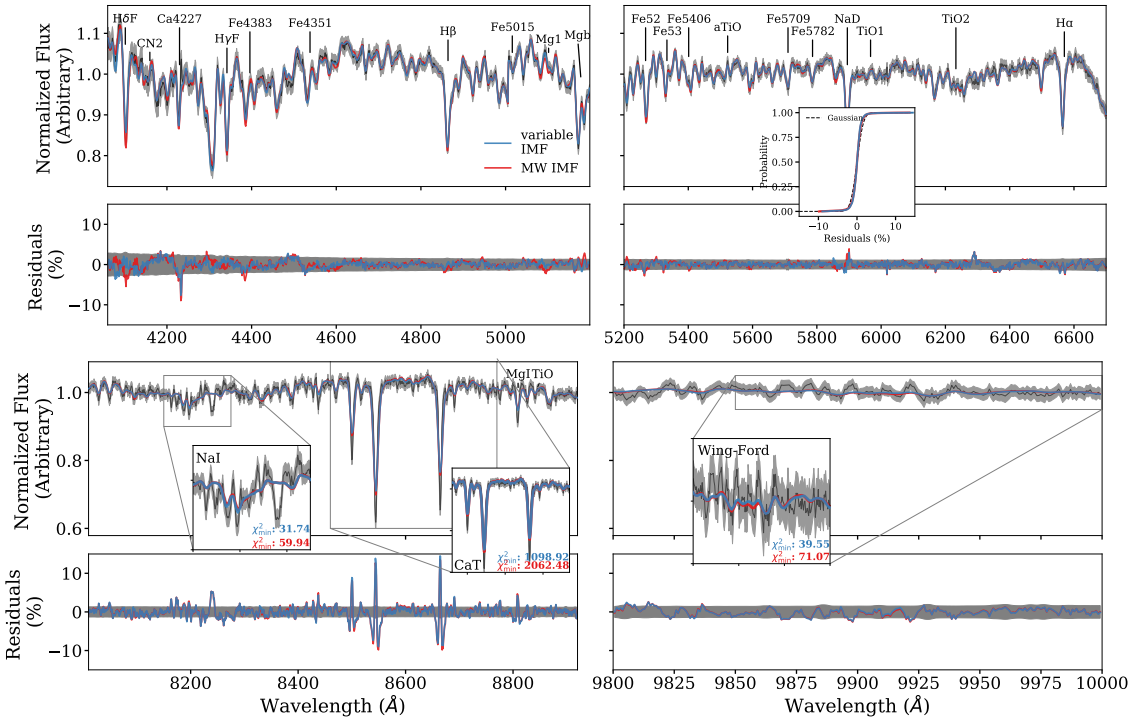

Figure B.5 The same as Figure 4.1 for the unsmoothed G001 data.

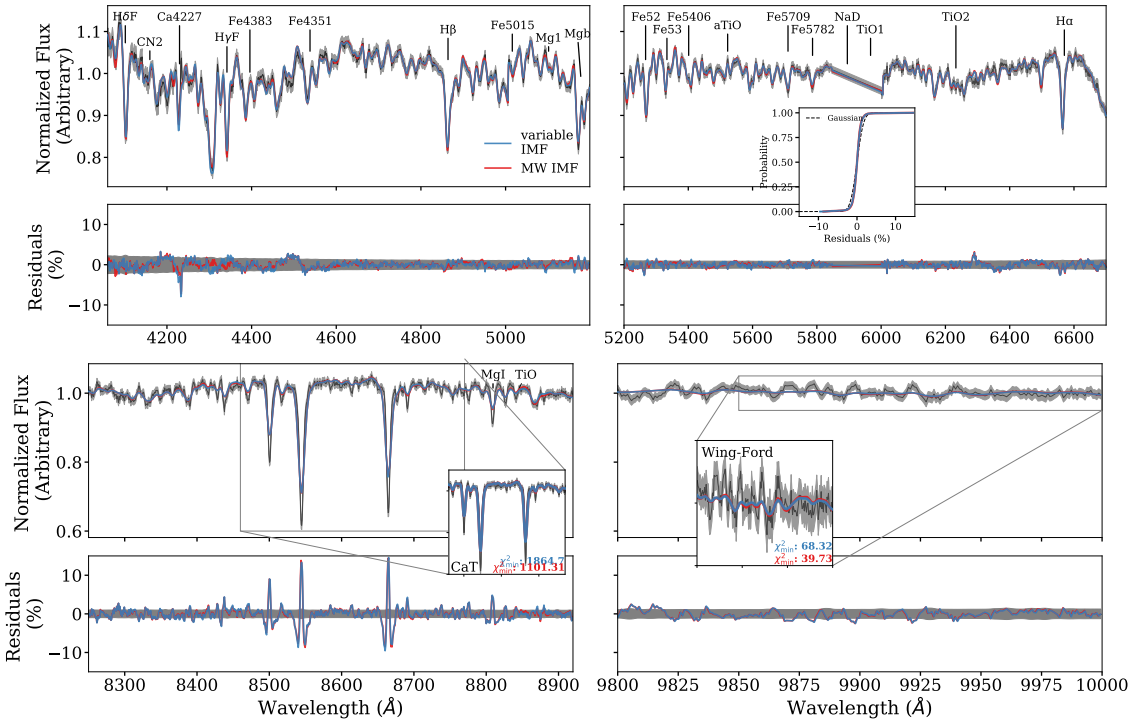

Figure B.6 The same as Figure 4.1 for the unsmoothed G001 data, with the NaD and NaI features removed.

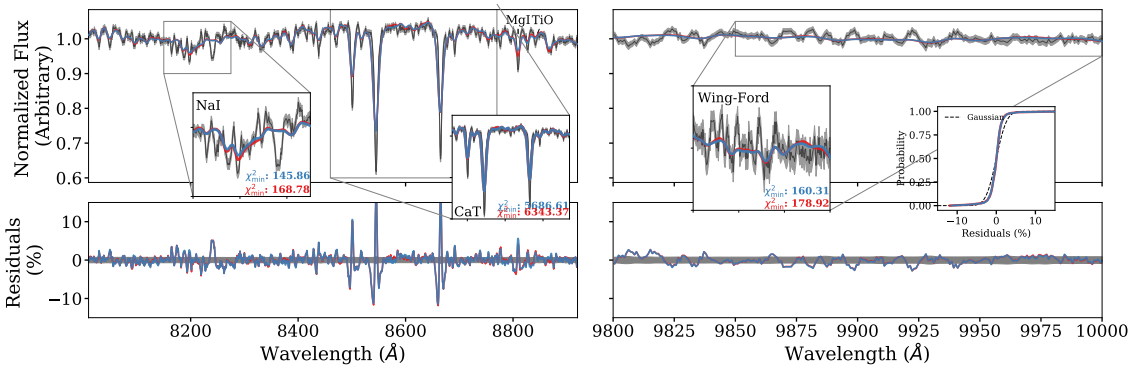

Figure B.7 The same as Figure 4.1 for the red unsmoothed G001 data.

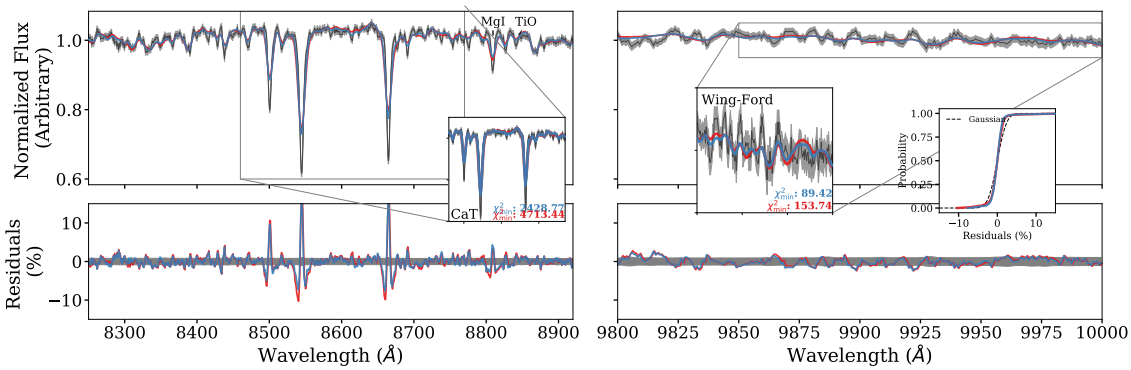

Figure B.8 The same as Figure 4.1 for the red unsmoothed G001 data, with the NaD and NaI features removed.

function simply the resolution, we must use the desired resolution subtracted in quadrature with the effective resolution (which is the quadrature sum of the instrument resolution and the velocity dispersion of the object in question):

$$\sigma_{\text{original}} = \sqrt{\sigma_{\text{instrument}} + \sigma^2_{\text{object}}} \tag{B.1}$$

$$\sigma_{\text{new}} = \sqrt{\sigma^2_{\text{desired}} - \sigma^2_{\text{original}}} \tag{B.2}$$

where σ_{original} is the effective resolution of the object, $\sigma_{\text{instrument}}$ is the wavelength-dependent resolution of the LRIS instrument, σ_{object} is the velocity dispersion of the object (obtained from the literature, see Table 4.5), σ_{new} is the resolution given to `smoothspec`, and σ_{desired} is the desired resolution to smooth to (in this case, 100 km/s). We show these fits in Figures B.9 and B.10, with and without the NaD and NaI features. Here, it seems the data are equally well-fit by a variable and MW IMF, similar to what we see in the main body of the paper.

We also test smoothing the data *to* 200 km/s (i.e. using Equations B.1 and B.1 above, with $\sigma_{\text{desired}} = 200$ km/s). These fits are shown, with and without the Na features, in Figures B.11 and B.12. Once again, a MW IMF cannot be ruled out based on these fits.

If we smooth the data by 200 km/s, as in the main body of the paper (see Chapter 3), but retain the Na features, we find that a MW and variable IMF fit the data equally well (see Figure B.3). This is surprising because, similar to NGC 4889, G001 is very bottom-heavy in Figure B.4.

We test increasing the uncertainties by 50% in Figures B.13 and B.14, with and without the Na features. We do this to test whether the models with regular and increased un-

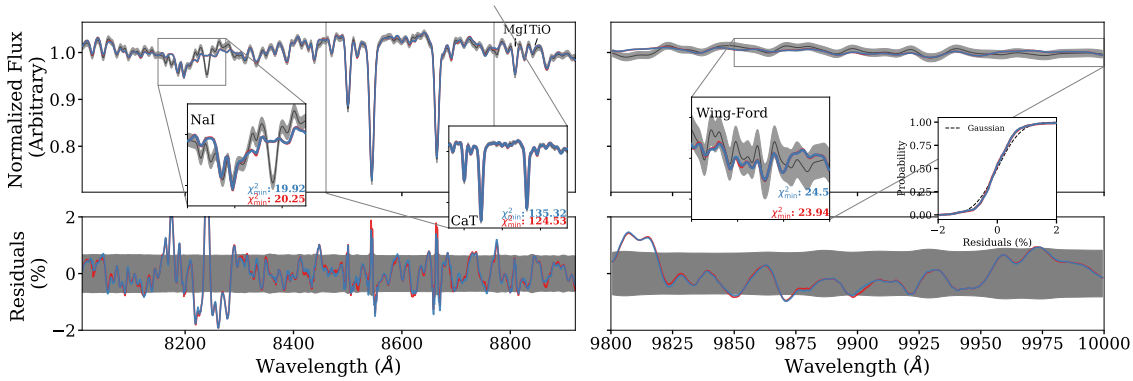

Figure B.9 The same as Figure 4.1 for the red G001 data, smoothed to 100 km/s.

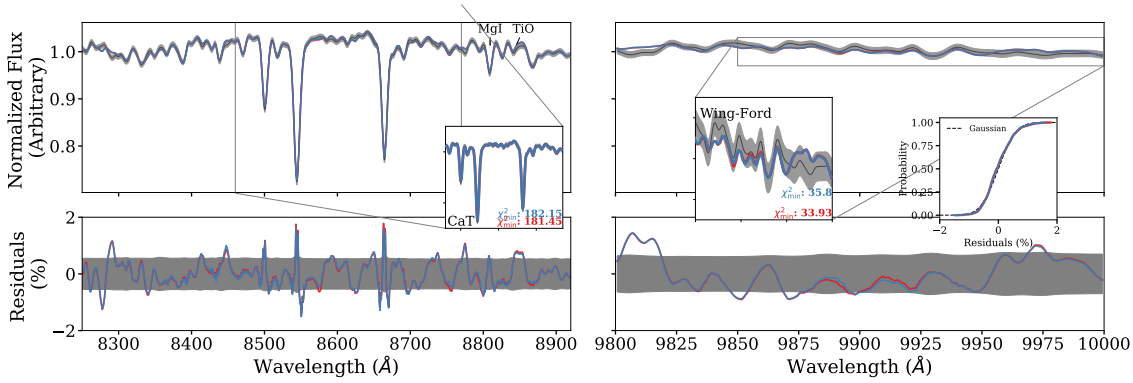

Figure B.10 The same as Figure 4.1 for the red G001 data, smoothed to 100 km/s, with the NaD and NaI features removed.

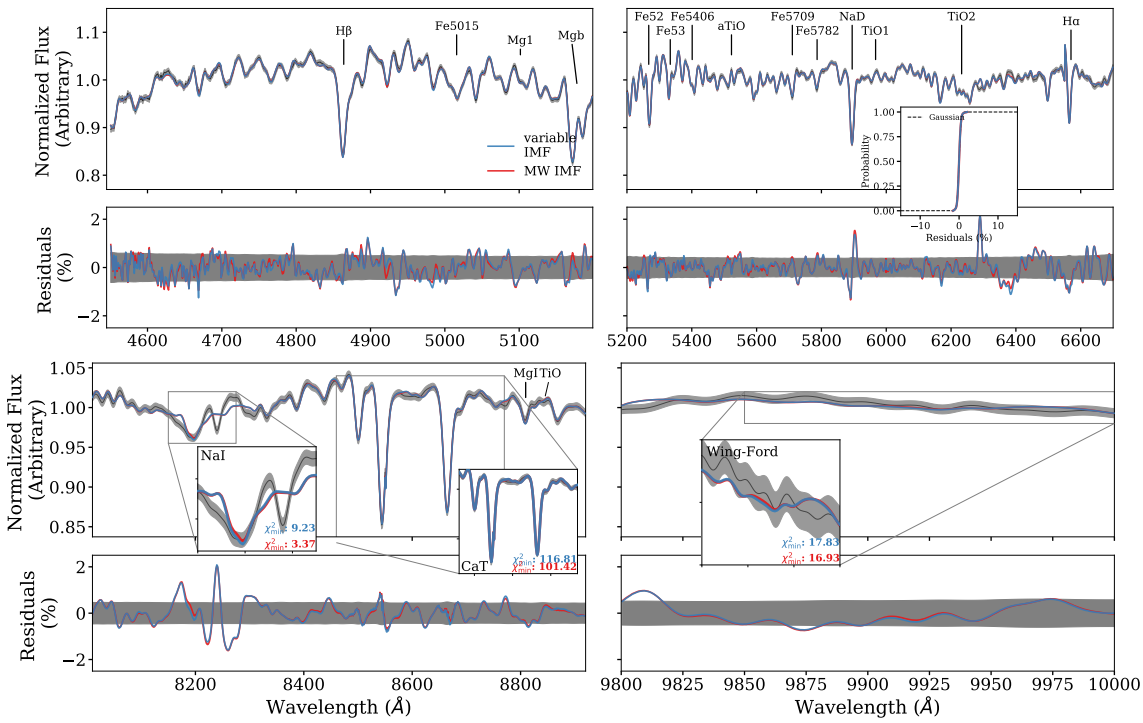

Figure B.11 The same as Figure 4.1 for the G001 data, smoothed to 200 km/s.

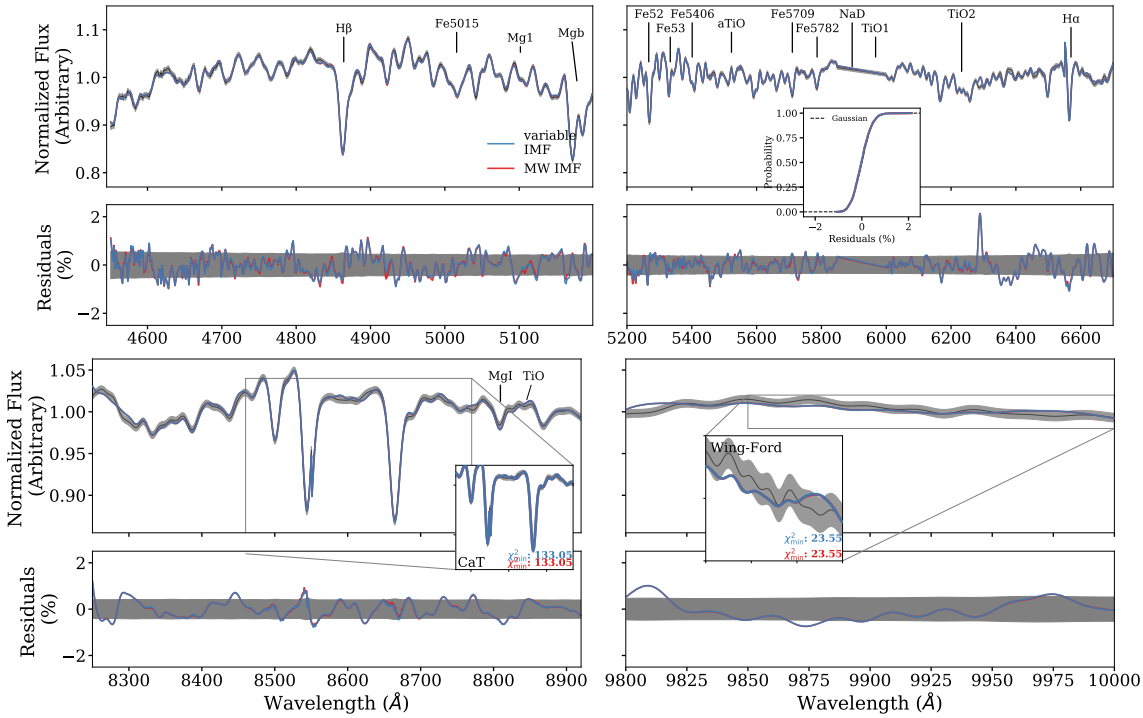

Figure B.12 The same as Figure 4.1 for the G001 data, smoothed to 200 km/s, with the NaD and NaI features removed.

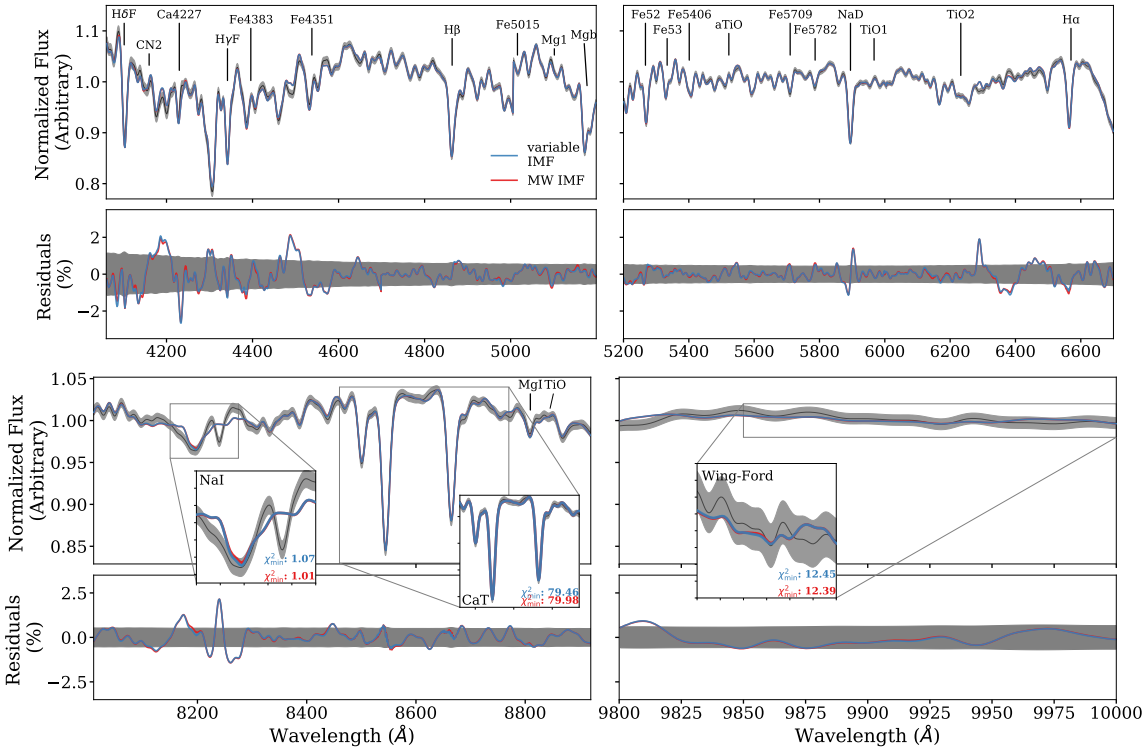

Figure B.13 The same as Figure 4.1 for the G001 data, smoothed by 200 km/s. The uncertainties have been increased by 50%.

certainties are consistent with each other (in which case this would indicate that residuals and artificial spikes in the spectra are driving the IMF) or if they are not (in which case the IMF variation may be real). In both fits, we find that the MW and variable IMFs fit the data equally well.

Finally, we test whether the continuum-normalization implemented in ALF could be affecting the results. ALF continuum-normalizes by multiplying the spectra by a high-order polynomial, where the order of the polynomial is dictated by the width of the wavelength range being fit (Conroy & van Dokkum 2012a). Thus, the continuum-normalization could ostensibly change if the wavelength ranges were wider or narrower. To test this, we define 10 wavelength chunks, encompassing the same overall wavelength regions. We show these fits in Figures B.15 and B.16, with and without Na features. However, there again does not seem to be a significant difference between the variable and MW models.

We summarize some of these tests in Figure B.17. Results from fits with the Na features

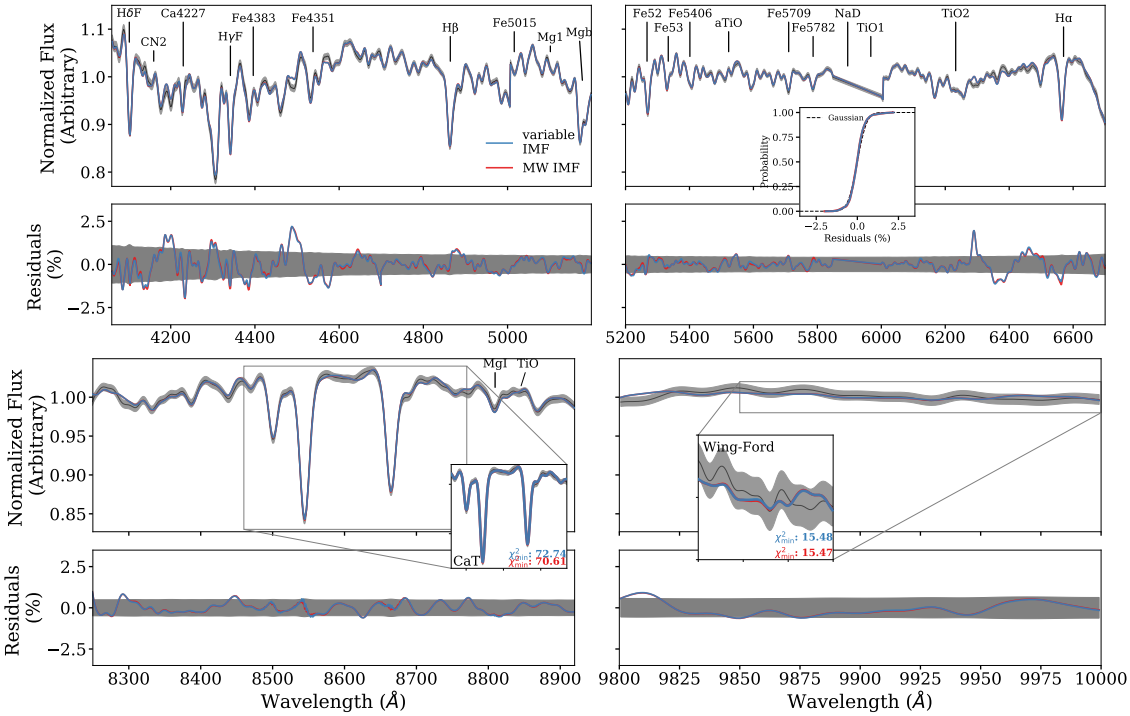

Figure B.14 The same as Figure 4.1 for the G001 data, smoothed by 200 km/s, with the NaD and NaI features removed. The uncertainties have been increased by 50%.

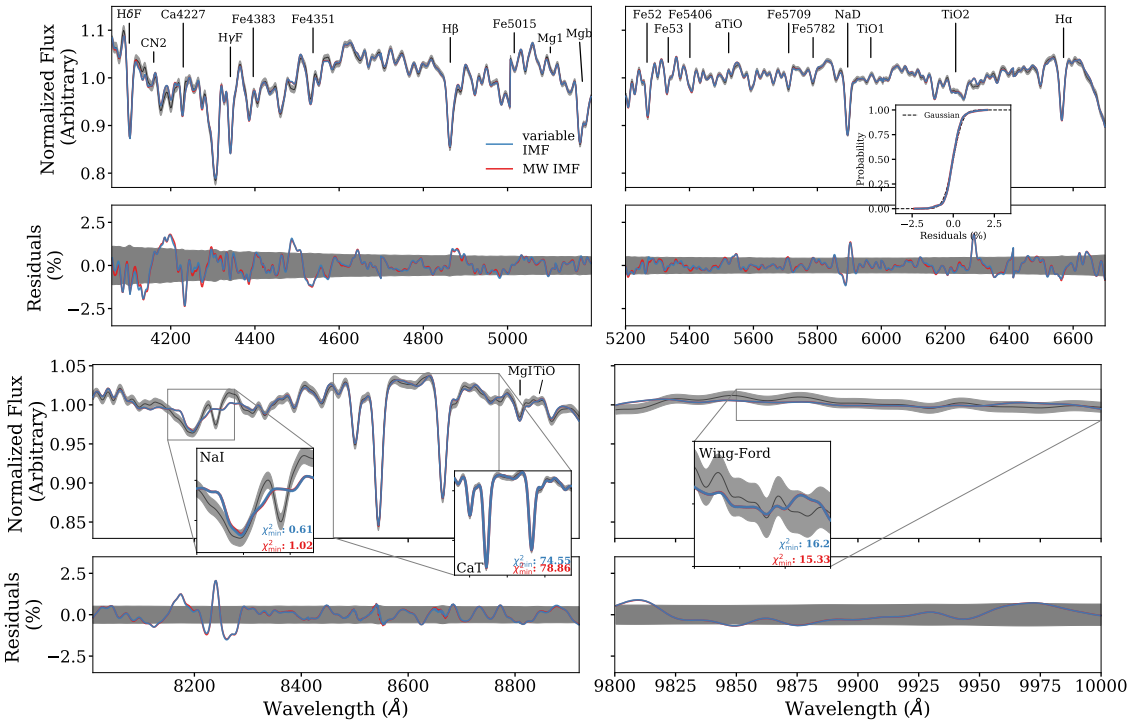

Figure B.15 The same as Figure 4.1 for the G001 data, smoothed by 200 km/s. We fit the spectrum over smaller wavelength ranges (10 in total).

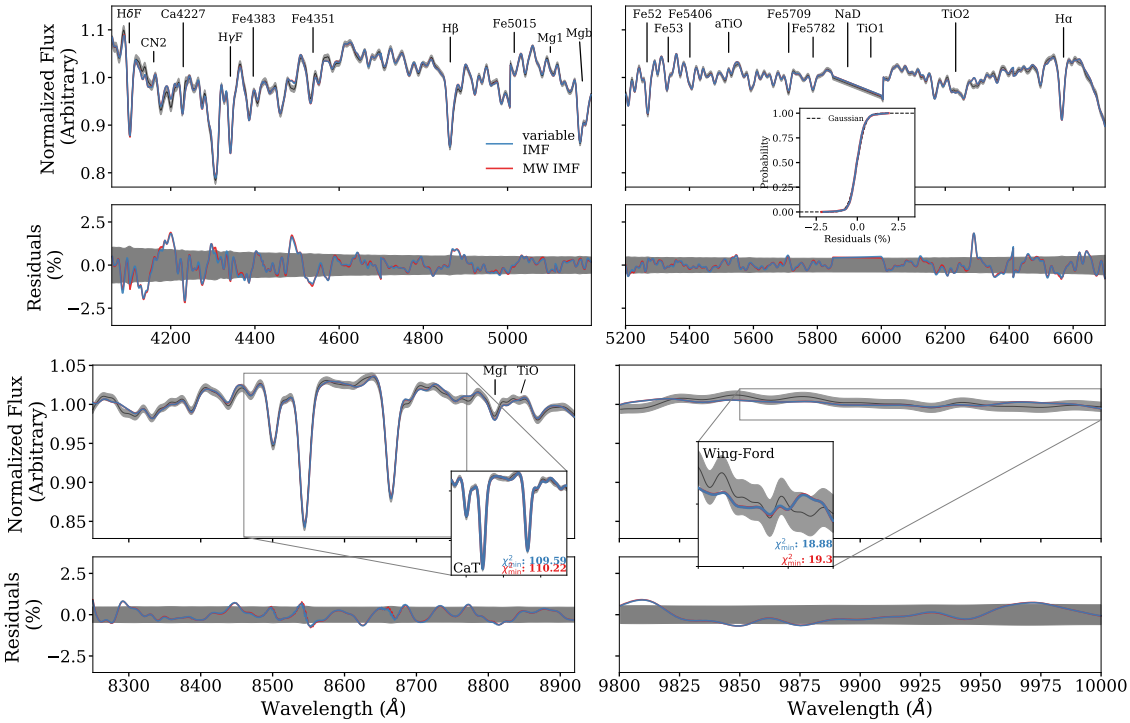

Figure B.16 The same as Figure 4.1 for the G001 data, smoothed by 200 km/s, with the NaD and NaI features removed. We fit the spectrum over smaller wavelength ranges (10 in total).

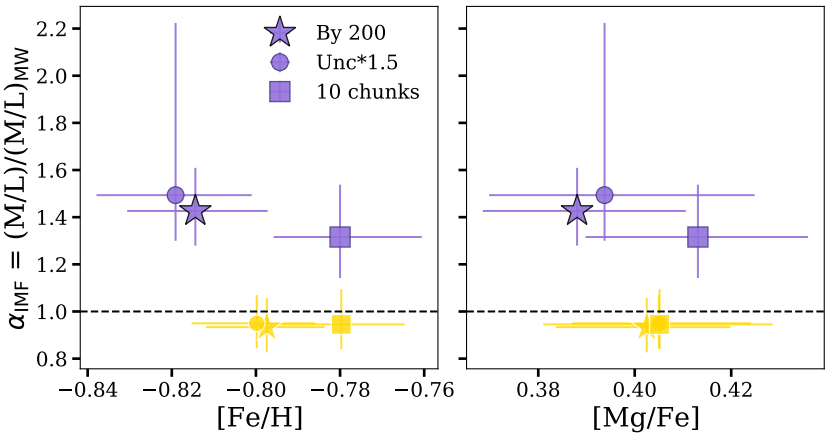

Figure B.17 Similar to the first two panels of Figure 4.6, but with various fitting tests for G001. The full spectrum fits are shown in purple and the fits with the NaD and NaI features removed are shown in yellow. We show the original G001 point from Figure B.4 for reference.

included are shown in purple and fits with NaD and NaI masked are shown in yellow. The G001 point from Figure B.4 (smoothed by 200 km/s) is shown for reference. We exclude from this figure tests that are unrealistic or cannot be directly compared to the others shown here. In particular, the tests where we fit the unsmoothed data can be neglected. We know that we must smooth the data for this object prior to fitting due to the limitation that the ALF models have a lower resolution than that of the CSSs, including G001.

Additionally, the "to 100" and "to 200" tests are not directly comparable to the rest of the points on this plot because they examine different wavelength ranges. The "to 100" test was limited to the red wavelength range only, because the resolution of the blue side is $>$ 100 km/s. Thus, important spectral information for constraining the chemical abundances is missing. The "to 200" test was limited to wavelengths $>$ 4545 Å since, below this, the resolution is $>$ 200 km/s. Thus, the most comparable points on Figure B.17 are the "by 200", "unc*1.5", and "10 chunks", all of which have been smoothed by 200 km/s. Considering only these points limits, we see that the spread in [Fe/H] for different smoothing routines is $\lesssim$ 0.05 dex and the spread in $\alpha_{\rm IMF}$ is 0.15 dex. Thus, different smoothing routines do not have a significant impact on our results.

Appendix C

Other Fits

Here we show the fits to all of the remaining objects in our sample, similar to, for example, Figure 4.3 in Section 4. Specifically, in the upper panels, we show the fully-reduced spectra for each object, along with a fit where we allow for a variable IMF (blue) and a fit where we fix a MW IMF (red). In the lower panels, we show the residuals for each fit. The residual uncertainties for the variable IMF fit are indicated by the grey bands. We highlight key, IMF-sensitive absorption features in the inset panels (CaT and the Wing-Ford band).

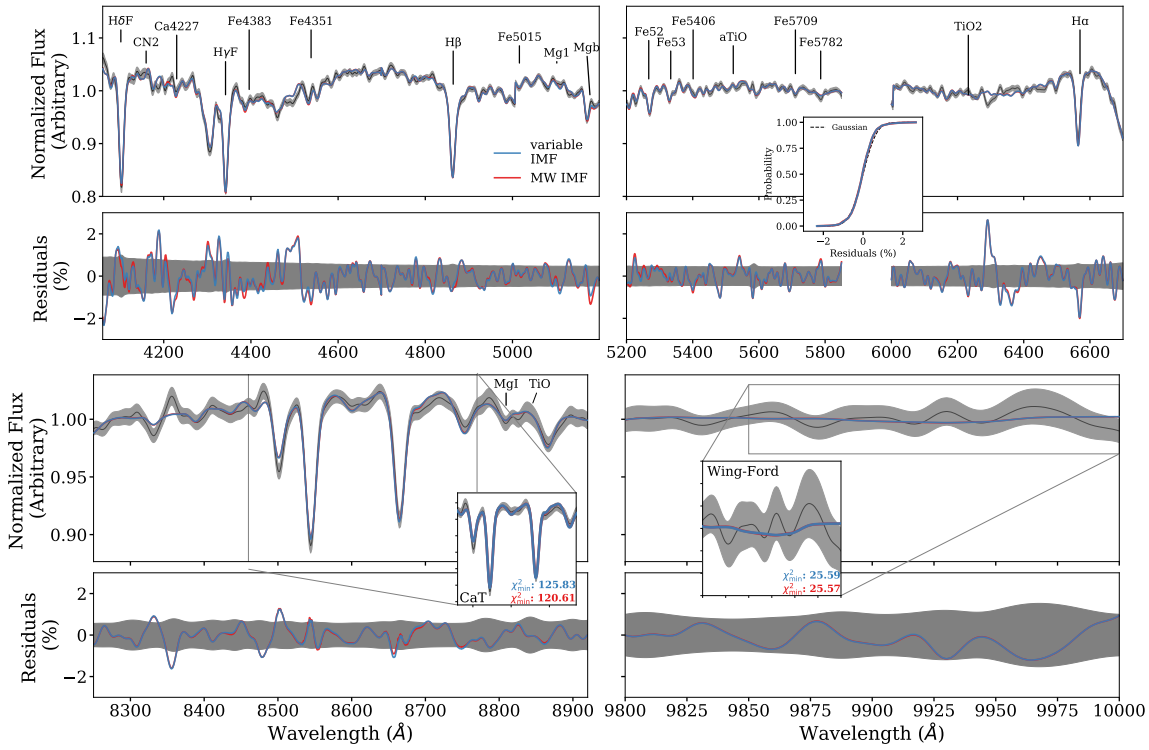

Figure C.1 The same as Figure 4.1, but for B012 (GC).

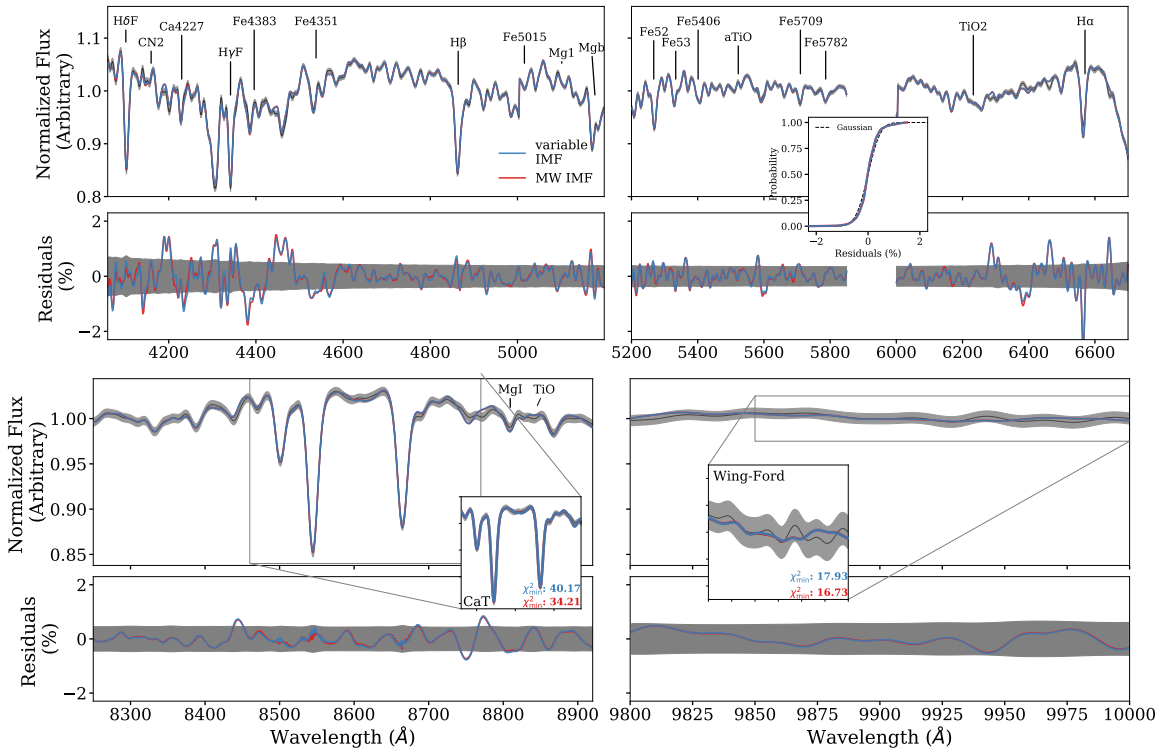

Figure C.2 The same as Figure 4.1, but for the 2014 data for B058 (GC).

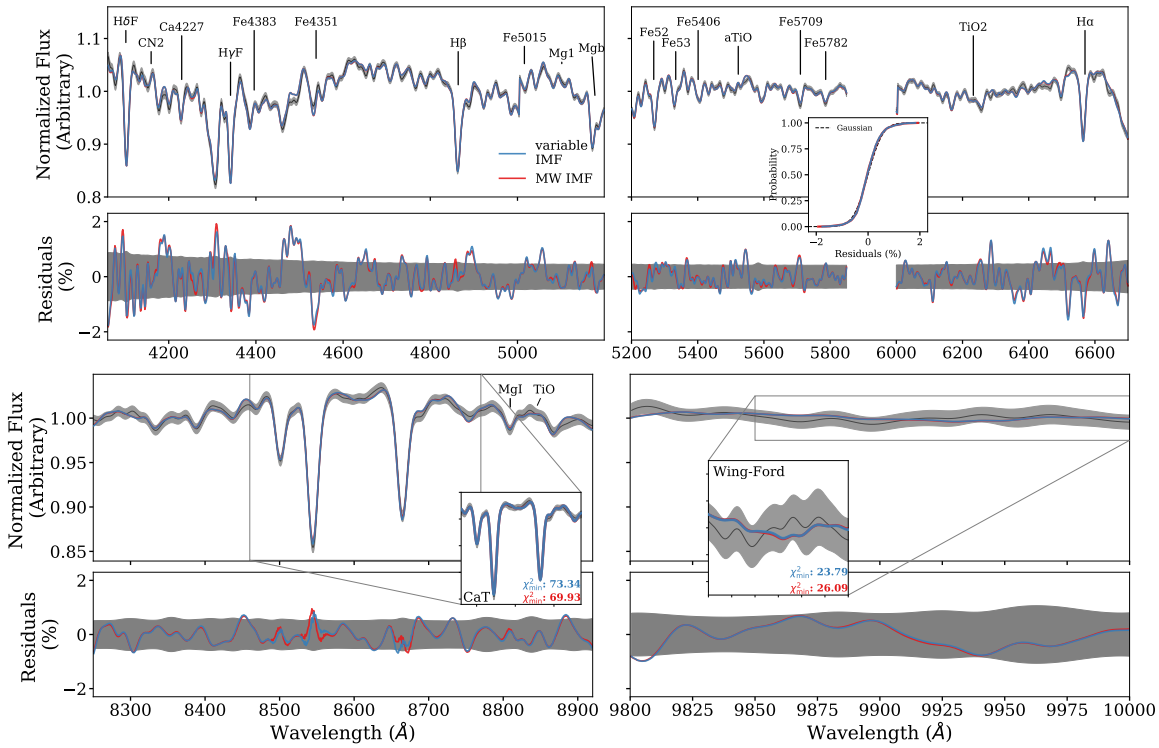

Figure C.3 The same as Figure 4.3, but for the 2016 data for B058 (GC).

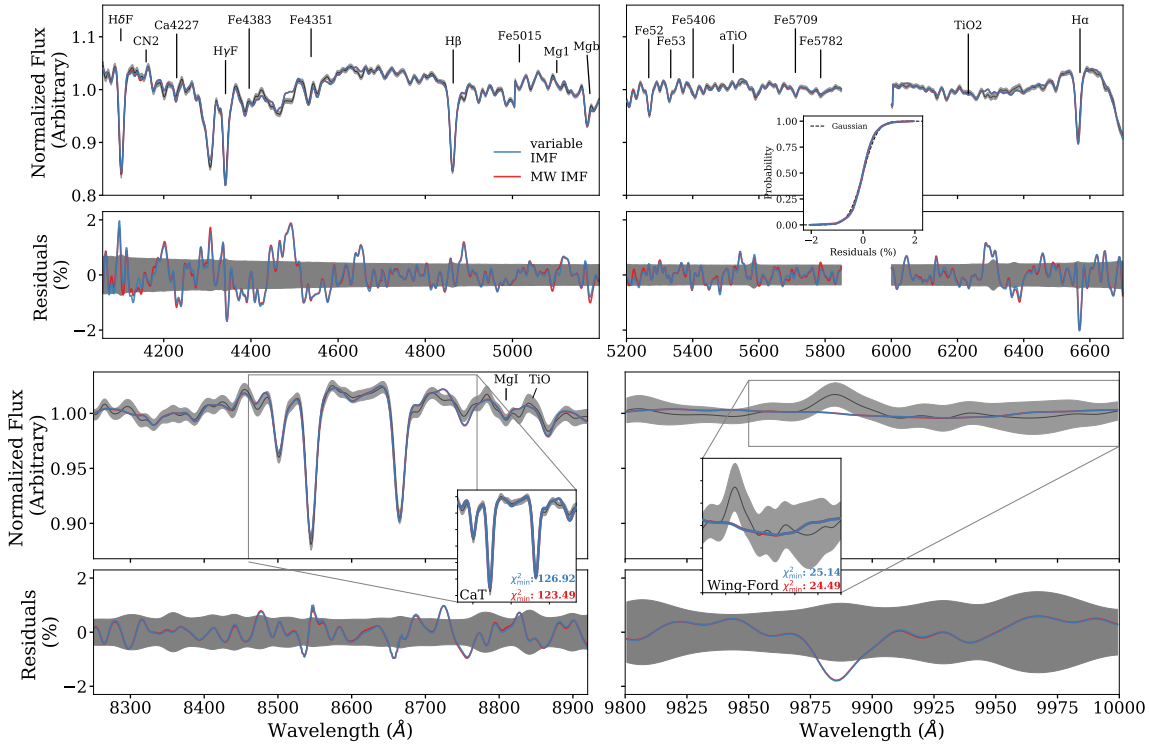

Figure C.4 The same as Figure 4.1, but for B067 (GC).

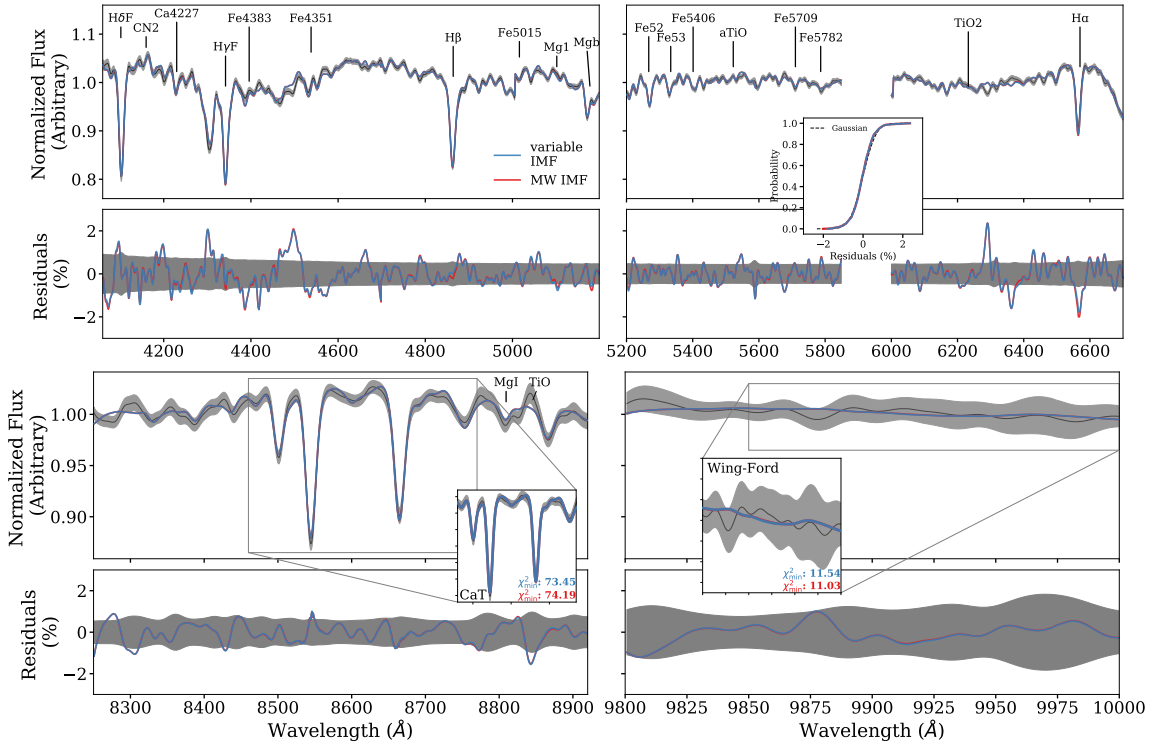

Figure C.5 The same as Figure 4.1, but for B074 (GC).

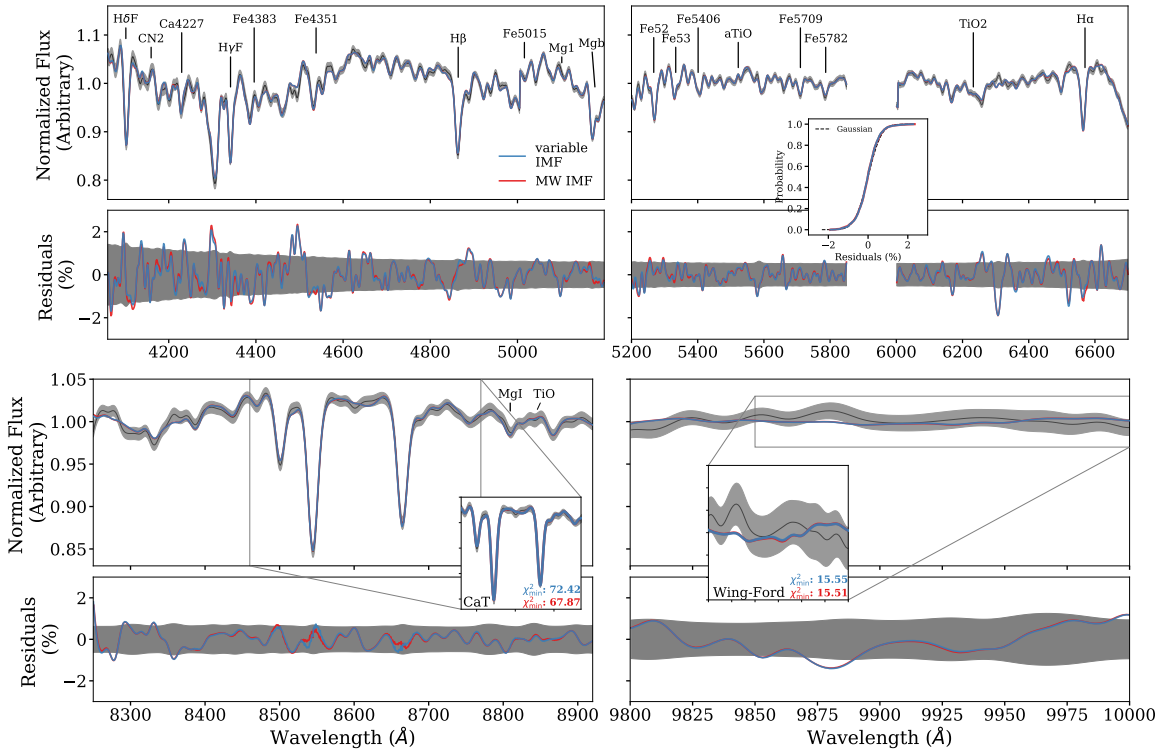

Figure C.6 The same as Figure 4.1, but for B107 (GC).

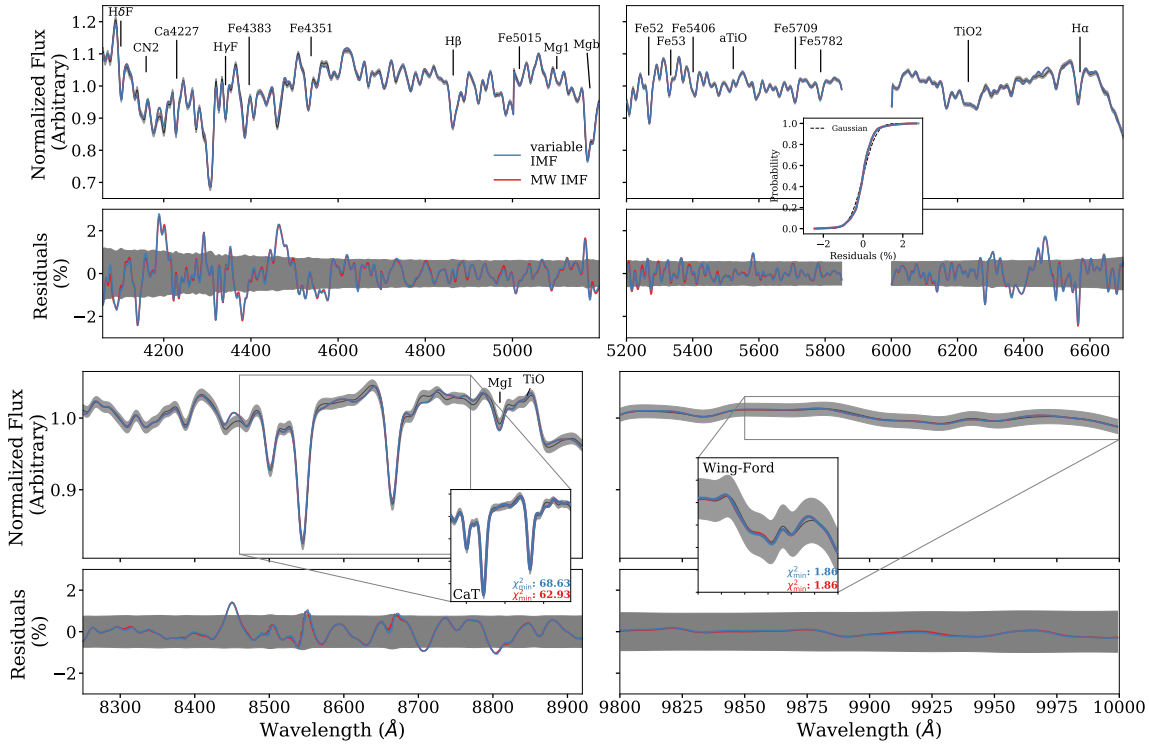

Figure C.7 The same as Figure 4.1, but for B163 (GC).

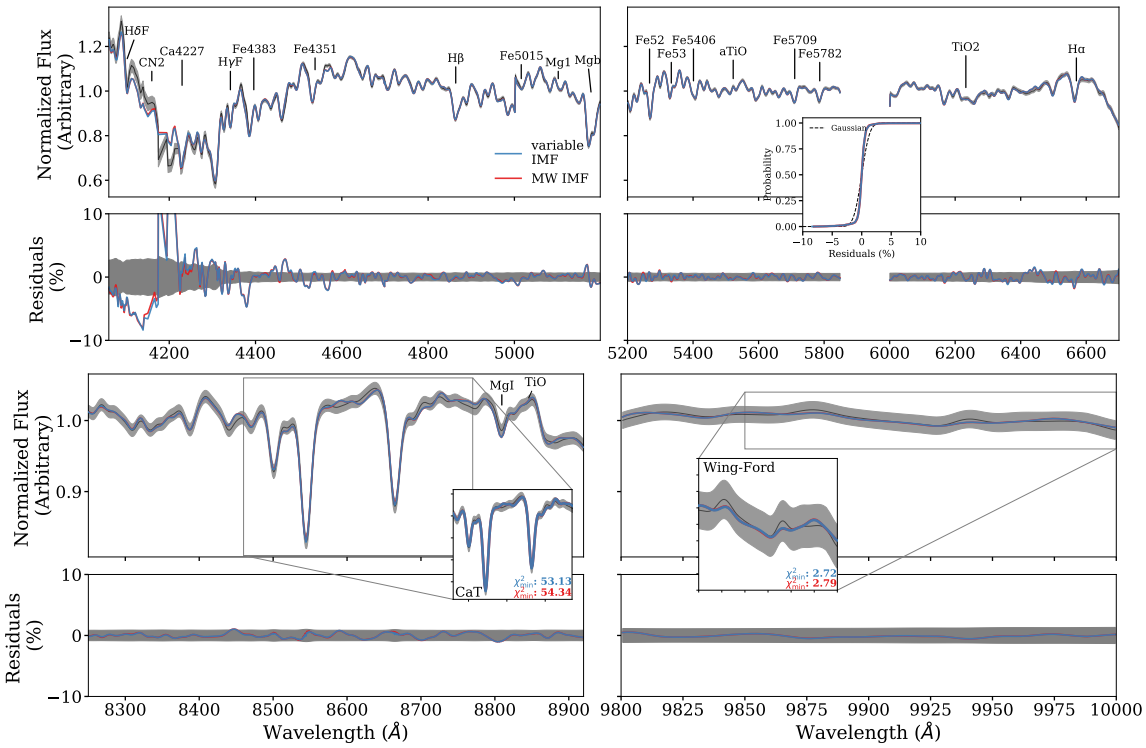

Figure C.8 The same as Figure 4.1, but for B193 (GC).

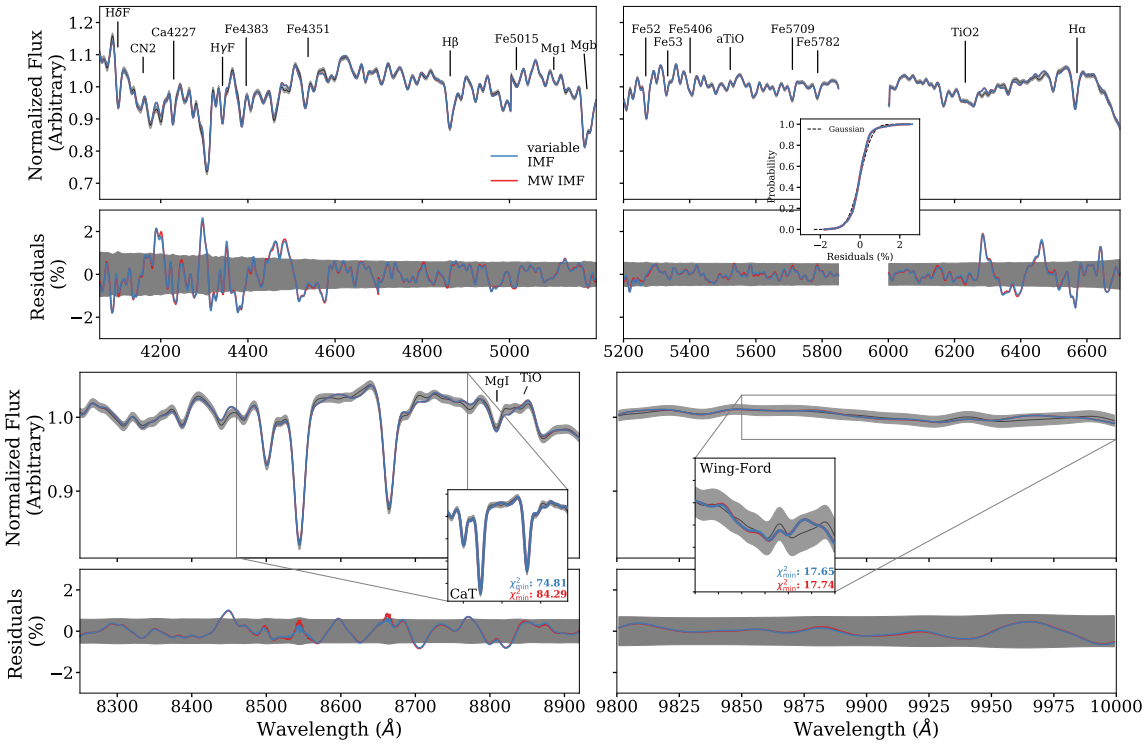

Figure C.9 The same as Figure 4.1, but for B225 (GC).

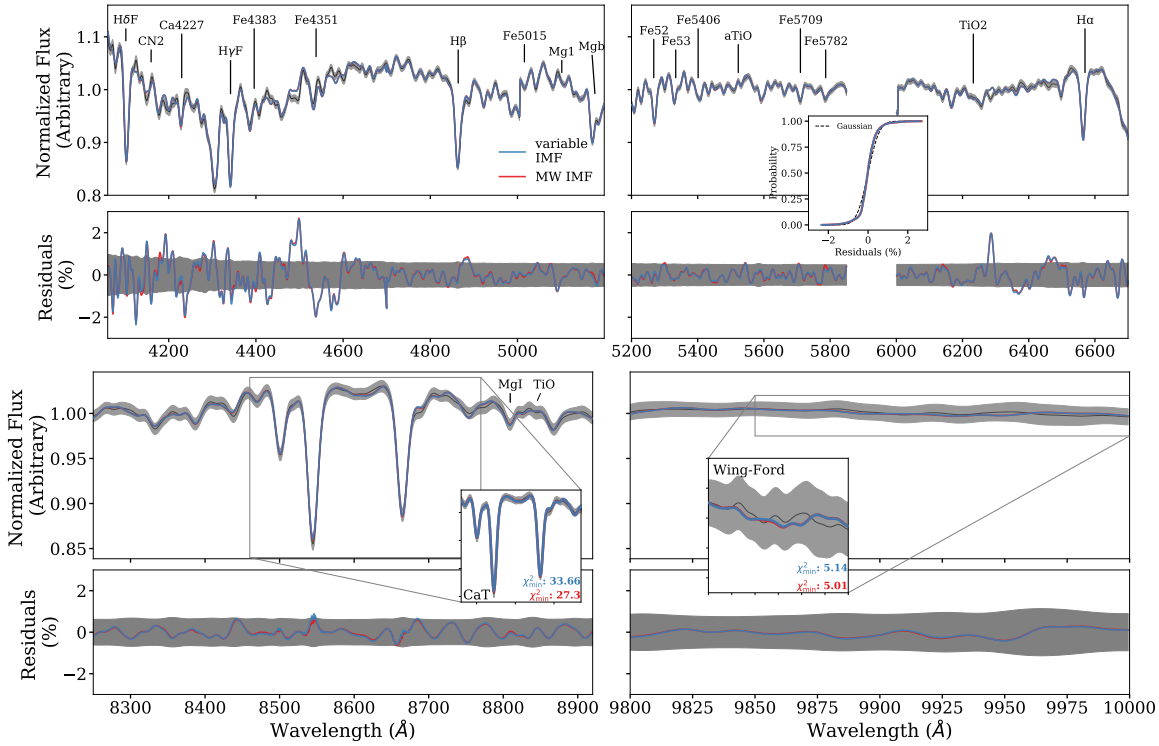

Figure C.10 The same as Figure 4.1, but for B338 (GC).

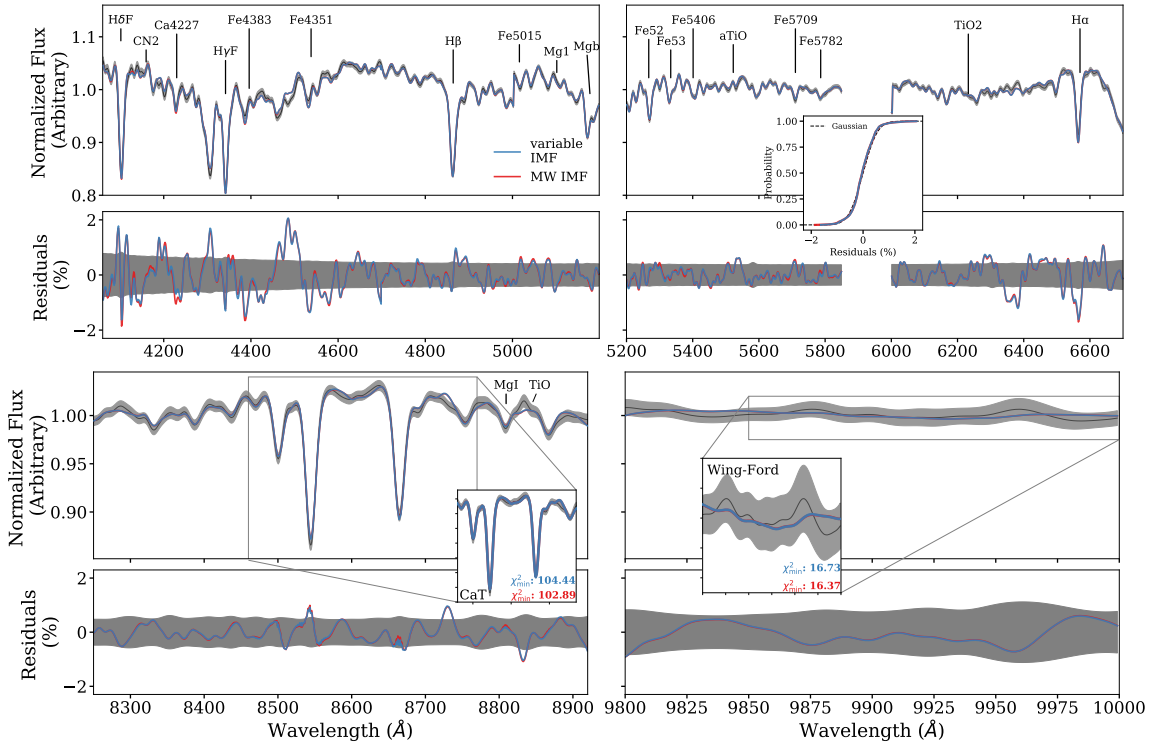

Figure C.11 The same as Figure 4.1, but for B405 (GC).

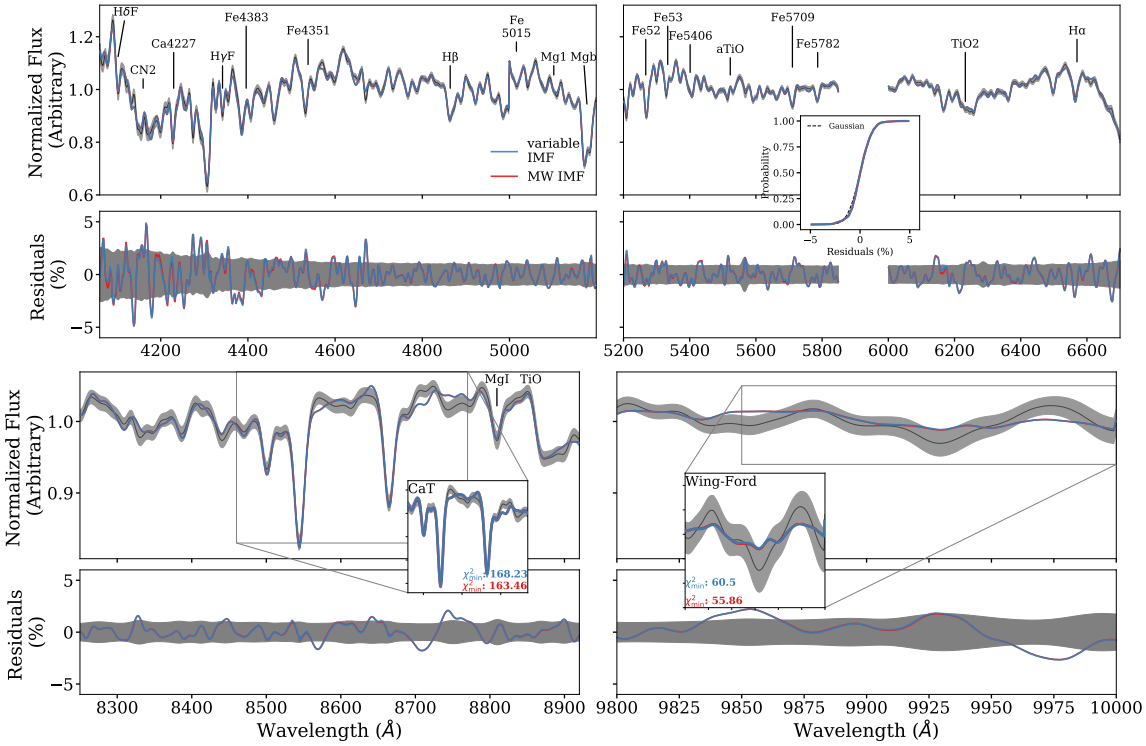

Figure C.12 The same as Figure 4.1, but for VUCD3 (UCD).

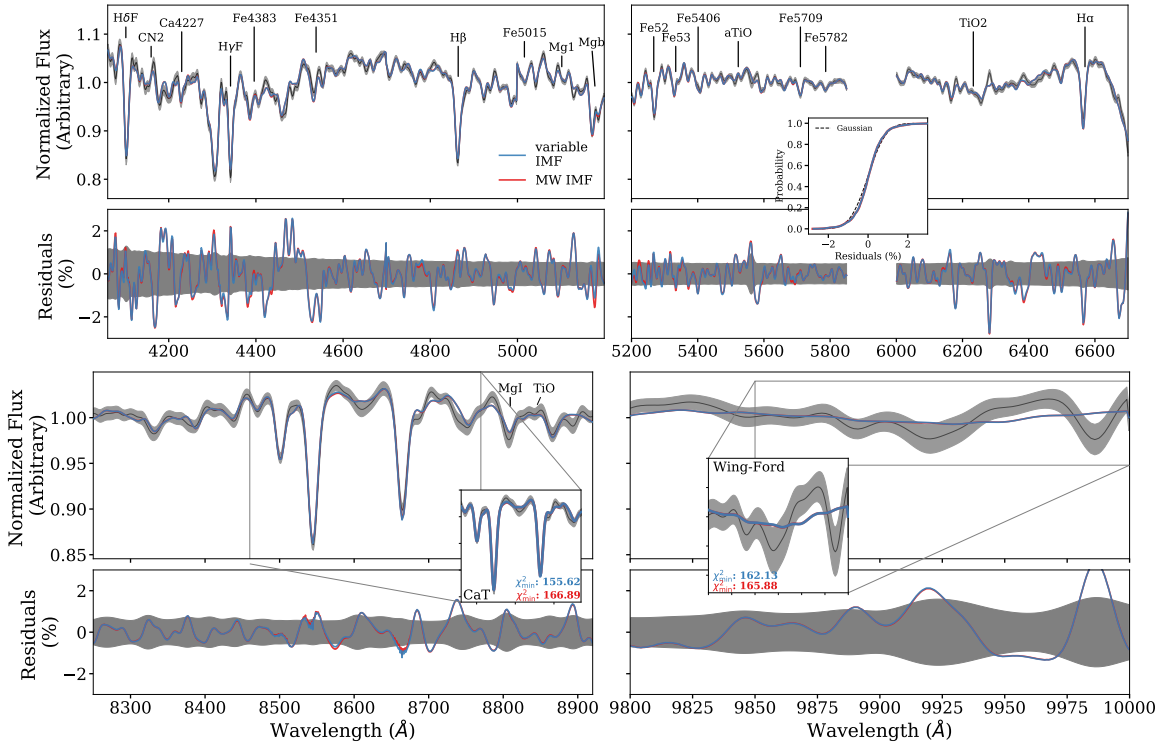

Figure C.13 The same as Figure 4.1, but for VUCD4 (UCD).

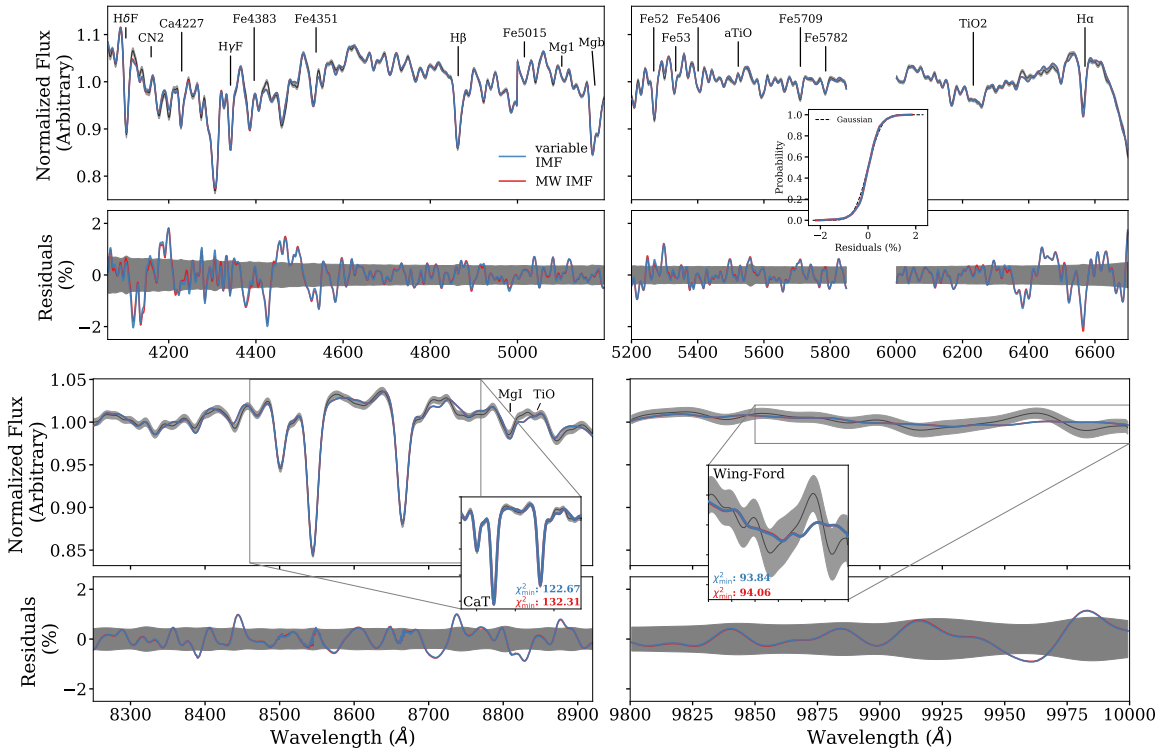

Figure C.14 The same as Figure 4.1, but for VUCD7 (UCD).